UCRL-52251

INVESTIGATIONS IN SILICATE GLASSES: I. Radiation Damage; II. Optical Nonlinearity

Michael James Moran
(Ph.D. Thesis)

November 15, 1976

Prepared for U.S. Energy Research & Development Administration under contract No. W-7405-Eng-48

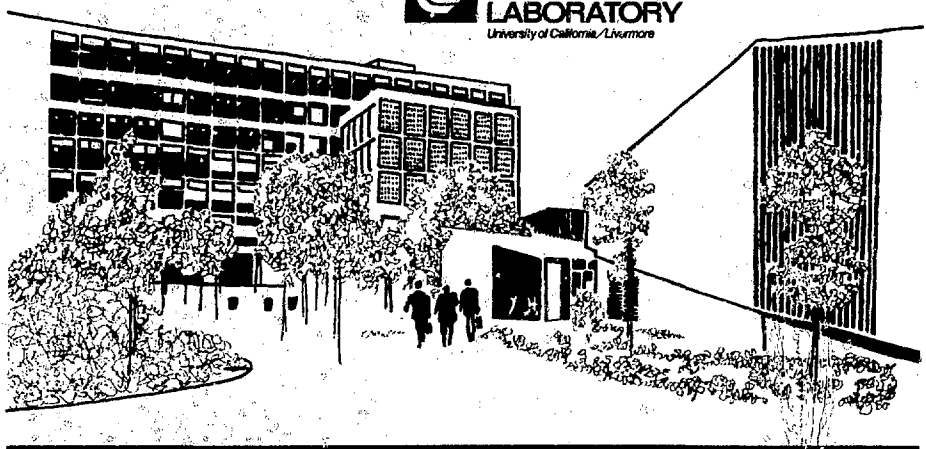

LAWRENCE LIVERMORE LABORATORY
University of California · Livermore, California 94550

UCRL-52251

INVESTIGATIONS IN SILICATE GLASSES: I. Radiation Damage; II. Optical Nonlinearity

Michael James Moran
(Ph.D. Thesis)

MS. date: Nov. 15, 1976

Investigations in Silicate Glasses:

I. Radiation Damage; II. Optical Nonlinearity

ABSTRACT

This thesis describes the investigation of two poorly understood but technologically important physical properties of silicate glasses and related materials. The first portion of the thesis describes the use of Electron Paramagnetic Resonance to investigate the nature of radiation-induced damage in glasses exposed to a variety of high-energy radiation sources. The second part of the thesis describes the measurement of the nonlinear index of refraction coefficient in a variety of optical materials related to the design of high-power laser systems.

The radiation damage investigations described in the first part of the thesis rely heavily on the comparison of experimental results for different experimental situations. The comparison of EPR lineshapes, absolute spin densities and power saturation behavior is used to probe a variety of microscopic and macroscopic aspects of radiation damage in glasses. Comparison of radiation damage associated with exposure to gamma rays and fast neutrons (and combinations thereof) are interpreted in terms of the microscopic damage mechanisms which are expected to be associated with the specific radiations. Comparison of radiation damage behavior in different types of glasses is also interpreted in terms of the behavior expected for the specific materials. The body of data which is generated is found to be internally self-consistent and is also generally consistent with the radiation damage behavior expected for specific situations.

The second part of the thesis describes a new and versatile technique for measuring the nonlinear index of refraction coefficient, n_2, in optical materials. The technique utilizes a 1 nanosecond pulsed neodymium-glass laser system and time-resolved interferometry to determine the ratio of the

coefficient n_2 of sample materials to the n_2 of CS_2. This method avoids some of the complications associated with performing absolute measurements of n_2 and allows the use of a relatively simple experimental technique. The measurements determine the nonlinear index ratios of the samples with an accuracy of about ± 15%. The technique is also demonstrated to be versatile with respect to performing measurements on different types of optical materials and promises to be useful for extending nonlinear index measurements to a variety of different experimental conditions.

Table of Contents

	Page
Abstract	ii
Table of Contents	iv
Part I: EPR Investigations of Radiation Damage in Silicate Glasses	1
I. INTRODUCTION	2
II. THEORY	5
A. Radiation Damage	5
B. Glasses	11
C. Electron Paramagnetic Resonance	19
III. EXPERIMENTAL	52
A. Irradiation Facilities	52
B. Sample Materials	54
C. EPR Spectrometer	55
IV. EXPERIMENTAL RESULTS	69
A. Introduction	69
B. Suprasil I	70
C. Suprasil WI	80
D. Quartz Crystal	87
E. Experimental Problems	87
F. Bk7 Glass	94
V. DISCUSSION	106
A. Introduction	106
B. Spin Densities	109
C. EPR Spectra	121
D. Saturation Behavior	136
E. Microscopic Damage Mechanisms	146
VI. SUMMARY AND CONCLUSIONS	157
REFERENCES	162
Part II. Measurement of the Nonlinear Optical Index Coefficient n_2	167
I. INTRODUCTION	168

II. THEORY OF EXPERIMENT..... 173
A. Introduction..... 173
B. Linear Susceptibility and Polarization..... 174
C. Nonlinear Susceptibility and Polarization.... 176
D. Nonlinear Propagation..... 181
III. EXPERIMENT..... 187
A. Introduction..... 187
B. The Laser System..... 188
C. The Interferometer..... 192
D. Measurement Technique..... 195
IV. EXPERIMENTAL RESULTS AND DISCUSSIONS..... 207
A. Introduction..... 207
B. Nonlinear Propagation Without Self-Focusing... 210
C. Anomalous Temporal Behavior..... 220
D. Nonlinear Index Coefficient Measurements..... 225
E. Nonlinear Index Coefficients-Discussion..... 231
V. CONCLUSIONS..... 239
ACKNOWLEDGEMENTS..... 245
Appendix I..... 246
Appendix II..... 249
Appendix III..... 252
REFERENCES..... 257

PART I: EPR INVESTIGATIONS OF RADIATION DAMAGE IN SILICATE GLASSES

I. INTRODUCTION

The study of the effects of high-energy radiation on solid materials is important for a number of reasons. There are many contemporary technical applications of solids where design criteria depend critically on their response to a high-energy radiation environment.[1,2,3] Studies of radiation damage can be used to characterize the response of materials to radiation, to verify various theoretical predictions of radiation damage behavior, to investigate the nature of specific mechanisms related to radiation-induced changes in physical properties and to probe the fundamental physical nature of solid materials. Each of these applications of radiation damage studies relates directly to current problems in materials science.[4-9]

The technical importance of radiation damage effects on a physical property of a material depends on the particular application of concern. For example, changes in the linear index of refraction and the optical absorption characteristics of glass components in a high power laser system may impose limitations on the performance of currently proposed laser-fusion schemes; while in magnetic confinement fusion experiments, it is the mechanical and electrical stability of first-wall reactor materials which is of primary concern. Depending on the particular application of concern, the effects of radiation on material properties such as the index of refraction, electrical conductivity, changes in elastic coefficients and dimensional stability must be well specified. For these situations, radiation damage studies can be extremely useful in terms of their immediate technical application.

The response of a material exposed to high-energy radiation is generally observed as changes in the physical properties of the material; and when the changes are undesirable, they are called radiation damage. Virtually all of the physical properties of a material can be affected by radiation damage.[10-13]

And, conversely, these physical properties can be used to characterize radiation damage.

In order to develop materials with improved radiation damage characteristics, it is necessary to develop an understanding of the microscopic processes responsible for radiation-induced changes in the bulk physical properties of a material. This is because changes in the macroscopic properties of a material generally occur as a result of the accumulation of high concentrations of microscopic damage sites in the material. While studies of the effects of radiation on bulk physical properties are useful for applied engineering problems, the inherent macroscopic nature of these studies makes it difficult to use them to investigate the microscopic nature of radiation damage. Fortunately, there is a number of diagnostic techniques not directly related to bulk physical properties which can be used to elucidate the microscopic nature of damage sites. Techniques such as electron microscopy,[6,14] x-ray diffraction,[10] small-angle x-ray scattering,[6] Raman spectroscopy,[6] optical spectroscopy[15] and electron paramagnetic resonance[4,5,16] have all been used to investigate the microscopic aspects of radiation damage.

This thesis describes the use of electron paramagnetic resonance (EPR) to characterize and investigate radiation damage in two different ultra-pure fused silicas, crystalline α-quartz and a multicomponent borosilicate glass. The materials were subjected to a variety of intense neutrons and gamma irradiations. The resulting EPR data are used to infer as much information as possible about the radiation damage mechanisms and the nature of the resulting microscopic defects.

In the sections which follow, there will first be a brief description of the current understanding of radiation damage mechanisms and the structural characteristics of silicate glasses and quartz, followed by a summary of some of the relevant aspects of EPR theory. The experimental sections

will describe the different facilities used for sample irradiations, the specific chemical compositions of the samples and the experimental facilities used to measure the EPR spectra. The experimental results will then be presented and will then be discussed in terms of their implications, limitations and possible applications.

II. THEORY

A. Radiation Damage

1. Introduction

Radiation damage in solids is a vast subject dealing with many aspects of the interaction of high energy radiation with matter. Both the microscopic mechanisms resulting in damage and the characteristics of the resulting damage depend on the type of radiation used and the specific material being studied. Our primary present interest is in material damage associated with the interaction of gamma and neutron radiation with silicate glasses and quartz crystal.

The initial step in the production of radiation induced damage is the absorption of energy from the incident radiation field. The absorption of energy occurs through collisions between particles of the incident radiation and the electrons and nuclei of the material. The initial (or "primary") collision of an incident particle generally results in the production of energetic electrons or ions (or primary "knock-ons") in the material. As they propagate through the material, the primary knock-ons experience additional collisions with electrons and nuclei and create additional energetic particles in a cascade-type process. Thus, the absorption of energy from the incident radiation results in the production of energetic particles within the material structure, leading to the creation of a variety of microscopic damage sites, or defects. An accumulation of these defects leads to the changes in physical properties associated with radiation damage.

The remainder of this section will present an elementary discussion of some of the microscopic scattering processes related to radiation damage in solids.[17] The discussion is not intended to be complete or rigorous, but is intended to establish a foundation for discussion of different types of radiation damage behavior. The choice of topics covered will

be determined by their direct relation to the experiments to be described below.

2. Gamma Rays

There are a number of different processes which can occur as the result of primary collision for γ-rays. In the absence of any resonant nuclear absorptions, and for gamma ray energies less than about 3 MeV, the primary collision usually consists of scattering by an atomic electron. The two most important scattering mechanisms for gamma energies up to a few MeV are the Compton effect and the photoelectric effect.

For γ-ray energies of about 1 MeV, the dominant mechanism in low Z materials is the Compton effect. The Compton effect is simply elastic scattering between an electron and a photon. The scattering cross section for this process is proportional to the atomic number Z of the atom and is a complicated function of the incident gamma ray energy. The kinetic energy of electrons resulting from this mechanism is also a complicated function of the incident photon energy; but for 1 MeV gamma rays, the resulting scattered electrons have an average kinetic energy of about 0.5 MeV.

For lower energy gammas, the photoelectric effect is an important scattering mechanism. In the photoelectric effect, an atomic electron absorbs the gamma ray energy and is subsequently emitted with a kinetic energy, T, given by:

$$T = E_\gamma - B \quad , \tag{1.1}$$

where E_γ is the gamma ray energy and B is the electron binding energy. For photon energies above the scattering threshold, the scattering cross section is proportional to Z^5 and decreases monotonically with $E_\gamma^{7/2}$ for increasing E_γ.

3. Fast Neutrons

There is a variety of interactions which can serve as primary collisions for fast neutrons (kinetic energy > 0.1 MeV) propagating in a solid material. Elastic scattering with atomic nuclei can transfer large amounts of energy to the target nuclei, resulting in the production of energetic ions in the material. Inelastic nuclear scattering resulting in the emission of gamma rays ((n,γ) reactions) is also frequently an important process. There is also a variety of nuclear reactions involving the capture of fast neutrons with subsequent emission of energetic particles which must also be considered. However, in SiO_2, the dominant mechanisms are elastic scattering by atomic nuclei and the (n,γ) reaction. In SiO_2, the scattering cross sections for the (n,γ) and elastic collisions with nuclei are roughly the same and are somewhat dependent on the fast neutron energy. For 14.8 MeV neutrons, the (n,γ) reaction with Si^{28} produces mainly 1.78 MeV γ-ray, and with O^{16}, a 6.3 MeV γ-ray. These γ-rays will probably not result in any unusual radiation damage in the material, but the 6.3 MeV gamma ray is interesting because it will have a significant cross-section for pair production.

The majority of the incident fast neutron energy which is absorbed is absorbed through elastic collisions with atomic nuclei. The maximum kinetic energy E_p transferred to the target nucleus in elastic scattering is given approximately by:

$$E_p(\max) \approx \frac{4E_n}{A} \quad , \tag{1.2}$$

where E_n is the incident neutron kinetic energy and A is the target nucleus atomic number. The scattering cross section is roughly independent of the incident neutron energy and the distribution of kinetic energy transferred to the target nucleus is roughly uniform. Thus, for a given incident fast neutron energy, the average transferred energy can be approximately written:

$$\bar{E}_p \simeq \frac{E_p(max)}{2} \quad . \tag{1.3}$$

While these equations are only approximate, they are useful for characterizing the order of magnitude of the energies for a specific situation. For example, using equations (1.2) and (1.3) we see that 15 MeV neutrons incident on SiO_2 will result in primary knock-ons with typical kinetic energies of about 2 MeV.

4. *Thermal Neutrons*

While thermal ($E_n \simeq .025$ eV) or low energy ($E_n << 0.1$ MeV) neutrons are not directly capable of causing material damage, nuclear reactions resulting from neutron capture in an atomic nucleus can be an important source of energetic charged particles within the internal structure. The resulting nuclear transmutations may also lead to significant changes in material composition. Fortunately, the cross sections for these processes for the naturally occurring isotopes of O and Si are small enough that they can generally be neglected.

However, the ${}_5B^{10}$ nuclear reaction:

$$B^{10} + n \rightarrow L_i^{7} + \alpha + 3.3 \text{ MeV} \tag{1.4}$$

is an excellent example where nuclear reactions act as a source of energetic charged particles and can also lead to a change in material composition. This particular reaction is important in the radiation damage behavior of the borosilicate glass to be described below. For low energy neutrons, the reaction has a very large cross section ($\sigma_a \sim 4 \cdot 10^3$ barns);[17] but the cross section decreases rapidly with increases in the incident neutron energy, so that for 100 KeV neutrons, σ_a is less than one barn. Both the lithium ion (kinetic energy ~ 1 MeV) and the alpha particle (kinetic energy ~ 2 MeV) released in this reaction have microscopic ranges on the order of microns and are capable of creating large numbers of energetic charged particles and the associated defects.

5. Energetic Charged Particles

The energetic ions produced by the scattering mechanisms described above are responsible for most of the atomic displacement events in a solid. Because of the ion's relatively large masses, elastic collisions between the ions and the atomic nuclei have a fairly large probability for causing an atomic displacement. These collisions are important because the accumulation of displacement damage is responsible for many of the changes in the mechanical and thermal properties due to radiation damage in solids.

When the primary knock-ons have fairly large kinetic energies (k.e. $\geq$ 0.1 MeV), the energy transferred to subsequent target nuclei can be quite large. These secondary knock-ons (or "secondaries") are capable of causing additional similar atomic displacements. Thus, we see that an energetic primary knock-on can lead to the production of large numbers of atomic displacement collisions in a cascade type process. If E_d is the energy required to displace an atom from its position (typically, $E_d \simeq$ 25 eV), the number of displacements ν which result from a primary knock-on with energy E_p can be estimated by the relation:

$$\nu \simeq \frac{E'}{2E_d} \quad , \tag{1.5}$$

where E' is the energy deposited into atomic displacement collisions. For example, the collision cascade resulting from an incident 1.5 MeV neutron can result in 10^2 to 10^3 atomic displacements in a volume containing 10^5 to 10^6 atoms.

Although atomic displacement collisions may be the most important events for radiation damage by energetic ions, most of the kinetic energy of the ions is dissipated in ionizing collisions with atomic electrons in the material. In fact, for 2 MeV Si or O ions in SiO_2, about 99.97% of their kinetic energy is absorbed in ionizing collisions, while only 0.03%

of their energy is absorbed in atomic displacements. A precise description of ionization processes is a difficult task, but a useful approximate description can be constructed with the use of an ionization energy threshold E_i. In this description, ions with kinetic energy less than E_i are assumed to be incapable of inducing electronic ionizations, while ions with energies greater than E_i are assumed to be capable of ionizing atomic electrons. For most ions and materials, E_i can be approximated by:

$$E_i \approx A \cdot 10^3 \text{ eV} , \tag{1.6}$$

where A is the atomic number of the ion. The Si and O primary knock-ons caused by 11.8 MeV neutrons have typical kinetic energies of about 2 MeV, and it is clear from eq. (1.6) that these ions will be capable of ionizing large numbers of electrons. The electrons ionized by these collisions will typically have relatively low kinetic energies ($\lesssim$ 100 eV), and it isn't clear what their direct effects on radiation damage behavior will be. In general, the effects of the ionized electrons will depend on the nature of the material and the types of states available for occupation by the electrons.

6. Energetic Electrons

The energetic electrons created by the collision processes described above dissipate their energy in a number of different processes. High energy relativistic electrons ($E_e \geq 2$ MeV) lose large portions of their energy to Bremstrahlung in slides. Electrons with energies between 0.5 MeV and 2 MeV can dissipate significant portions of their energy in elastic scattering events with atomic nuclei, resulting in the production of atomic displacements in the material. However, most of the energetic electrons of interest in the present experiments have kinetic energies less than 0.5 MeV, and for these electrons kinetic energy is dissipated in ionizing collisions with other electrons. The relative importance of these

different scattering mechanisms depends on the specific situation of interest. Some of these different processes will be considered in more detail in the discussion of the experimental results in a later section of the thesis.

B. Glasses

1. Introduction

The glassy state of matter arises when a liquid is cooled to a temperature where it solidifies in a time span short enough to prevent crystallization.[18] Most common glasses result from the fusing together of various oxides, with SiO_2 being the base constituent for most commercially produced glasses.

Glasses are not well understood materials. The bulk physical properties of glasses often exhibit anomalies which cannot be explained on the basis of simple models of the nature of glasses. Much of this difficulty is due to a lack of precise understanding of the microscopic amorphous structure of glasses and the effects of amorphous structure on the bulk physical properties.

This section will present a brief introduction to the structure and chemistry of glasses. With this background information, some of the commonly involved radiation damage defects in glasses will then be described.

2. Chemistry

There are several base constituents, or network formers, which are used to form oxide glasses. These compounds include B_2O_3, Al_2O_3, SiO_2 and P_2O_5. Pure amorphous SiO_2 (fused silica) is an extremely hard glass with desirable properties for many applications, but its high fusion temperature limits its practical usefulness.

The physical properties of glasses can be altered by adding various oxides to the base glass composition. The detailed reasons for changes

in the physical properties are not generally well understood; but in some cases these changes can be explained in relatively simple terms. For example, Na_2O is often added to glasses as a softening agent.[18] In the glass, the Na atoms tend to dissociate from the oxygens and occupy interstitial positions in the glass network. The excess oxygens thus produced are then bonded to Si atoms with a single Si-O band. Thus, as Na_2O is added to SiO_2, the double Si-O-Si bonds tend to be broken up into single Si-O bonds, with a weakening or softening of the glass structure as a result.

One of the main goals of contemporary glass research is to develop fabrication techniques based on an understanding of the microscopic nature of glasses and the microstructure's relationship to the resulting bulk physical properties. Recipes for fabricating glasses with specific physical properties have been developed largely through a tradition of trial and error. The Na_2O example cited above is only a very simple case of the application of glass chemistry to control the resultant bulk physical properties of a glass. There is a large number of oxides which are used to control physical properties of a glass such as hardness, melting temperature or index of refraction. While glass compositions are intended to lead to glasses with a specific combination of physical properties, in general, no glass is perfectly suited to its application; but has a combination of desirable and undesirable characteristics.

3. Structure

The microscopic structure of glasses is a subject which is still being actively investigated. The amorphous nature of glasses makes it difficult to investigate and specify the precise nature of their microstructure. In spite of the difficulties, a considerable amount of information has been collected on the structure of these materials.

One of the materials that we are most concerned with here is fused silica, a pure, noncrystalline form of SiO_2. Careful x-ray diffraction studies have yielded four numbers which help to characterize its microscopic structure:[19,20,21] (1) The average Si-O distance is 1.62 Å. (2) The average O-O distance is 2.65 Å. (3) Practically all of the Si atoms are tetrahedrally bonded to four oxygen atoms. (4) Practically all of the oxygen atoms are bonded to two Si atoms, with a large variation in the Si-O-Si bond angles (from 120° to 180°). This structure is often schematically represented by the two-dimensional grid of Fig. 1.1(a).

The above numbers have a strong resemblance to the corresponding numbers for the crystalline forms of SiO_2 and they imply that fused silica is an extended network of SiO_4 tetrahedra which interlock in a random fashion to form the microscopic glass network. The tetrahedra, then, are bound tightly together to form a sort of giant molecule, a fact which correlates with the strength and hardness of silicate glasses.

An interesting and important example of a different glass structure is supplied by amorphous B_2O_3. Diffraction studies have indicated[19] that the microstructure of amorphous B_2O_3 is composed of interlocking BO_3 triangles, with the average B-O distance being about 1.4 Å. This can be schematically represented by the two-dimensional grid of Fig. 1.1(b).

The addition of Na_2O to B_2O_3 results in the phenomena known as the boric oxide anomaly. As Na_2O is added to the glass, the excess oxygens become bound to the boron atoms. The binding occurs in such a manner that the BO_3 triangles are slowly converted to BO_4 tetrahedra (with an average B-O distance of about 1.5 Å) in order to accommodate the extra oxygens.

Glasses composed of a mixture of SiO_2 and B_2O_3 are commonly used for a wide variety of commercial applications. The brief description given

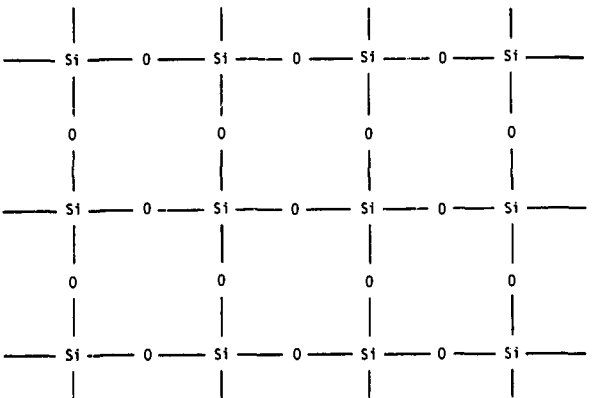

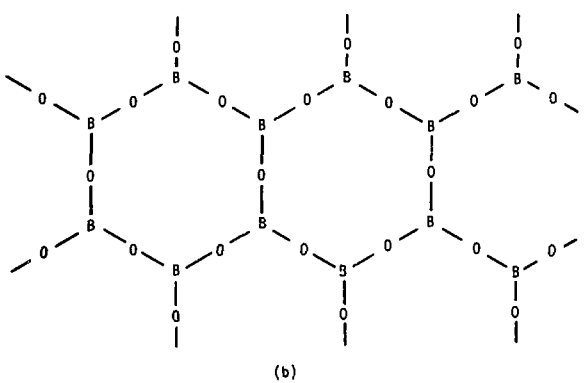

Figure 1.1 Schematic Glass Structures

These figures schematically describe two different types of glass structure. In part (a), the tetrahedral bonding scheme of SiO_2 is illustrated; while in part (b), the triangular bonding arrangement associated with B_2O_3 is shown. In actual glasses, there is no long-range preferred orientation for the atomic bonding in the microstructure.

above of their structures should indicate the problems which will be encountered in any attempt to study or characterize the details of their microscopic characteristics. It is because of these difficulties that the chemistry of glass design depends largely on the recipes developed in the past by trial and error.

4. Defect Structures

Changes in the bulk physical properties of a material associated with radiation damage are due to the collective effects of large numbers of microscopic damage sites, or defects, in the material. There are two basic types of damage which can occur on a microscopic scale in response to high energy radiation. The first, displacement damage, consists of changes in the microscopic structure due to the displacement of an atom over distances varying from the interatomic separation to several microns. The second, ionization processes, are changes in a material resulting from the transition of electrons from their initial ground state in the undamaged material to some other state in the material. There are several other processes, such as nuclear transmutation due to nuclear reactions, which must also be considered for some specific situations.

Defects encountered in solids can usually be classified according to whether they are extrinsic or intrinsic. Extrinsic defects are microscopic defects associated with the presence of an impurity in the material. In glasses, extrinsic defects are often trapped electrons or holes at the site of a multivalent impurity ion. Intrinsic defects are changes in the characteristic microscopic structure of a material. Commonly encountered defects in silicates include[5,22,23] vacancies, interstitials, non-bridging oxygens and broken bonds within the structural network.

Extrinsic defects have been investigated by a number of different techniques; but optical and EPR spectroscopy have been two of the most

useful approaches. The use of spectroscopic methods to investigate the nature of a specific defect is a difficult task, especially in glasses where the microstructure is amorphous and poorly understood, but is often useful for identifying some of the general characteristics of a specific defect. For example, the identification of the extrinsic nature of a particular defect has often been established by noting the correlation between the concentration of a particular atomic species and the intensity of a corresponding spectral line. The use of these techniques in silicate glasses has established that Ce^{3+}, Fe^{2+} and Mn^{2+} are typical hole trapping centers, while Eu^{3+}, Ti^{4+} and Ce^{4+} ions have been identified as electron trapping sites.[24,25,26,27]

The investigation of intrinsic defects is generally more difficult than the investigation of extrinsic defects. For the extrinsic defects mentioned above, prior knowledge of the optical and EPR characteristics of a particular ion have been instrumental in the interpretation of the data. The investigation of intrinsic defects does not have this advantage and interpretation of the data must often proceed from first principles. In this case, analysis of the spectral data must be used to determine the nature of the paramagnetic electron state of interest, in addition to determining the local structural characteristics associated with the defect. This is a very difficult task and has been successful for only a few specific situations, usually involving crystalline materials.

Investigation of intrinsic defects in fused silica has depended strongly on intrinsic defect studies in crystalline α-quartz.[16] In a crystalline material, the well defined microscopic atomic environments makes feasible the detailed analysis of the spectral characteristics of a defect center. And since both the crystalline and glassy forms of silica have the same tetrahedral bonding scheme between the oxygen and silicon atoms, it is expected that both types of materials will have the same types of local

microscopic intrinsic defects. The spectroscopic characteristics of defects in these materials have verified these expectations and have been used to interpret the radiation damage behavior of fused silica.

Optical and EPR investigations of radiation damage in quartz crystal have established the existence of two types of intrinsic defects (the E_1' and E_2' centers).[22] The centers appear to be closely related and studies of the details of the associated EPR spectra have determined that the E' defect consists of the electron occupation of sp^3 hybrid orbital at an incompletely bonded silicon atom.[16] The investigations have not succeeded in determining the complete details of the microscopic structure of these defects and there have been numerous suggestions of likely defect structures. Two of the often cited structures are illustrated in Figs. 1.2.[22] In Fig. 1.2(a), the E_1' center is represented as the electron occupation of an oxygen vacancy in the tetrahedral network; while the E_2' center is represented in Fig. 1.2(b) as the electron occupation of an oxygen vacancy adjacent to a silicon vacancy.

The results of intrinsic defect studies in crystalline quartz have been almost completely consistent with the results of corresponding studies in fused silicas. While much early work was hampered by the confusing effects of the low level impurity contents of glass samples, recent improvements in fabrication techniques have made possible the detailed comparison in fused silica and crystalline quartz. In both types of materials, the ultraviolet absorption spectra associated with the presence of E' centers are very similar.[22] And the E' spectra of damage centers in fused silica have been consistent with the spectra expected on the basis of the spectra observed in crystalline samples. But because of the ambiguities which are inherent in the analysis of optical or EPR spectra in glasses (due to the amorphous nature of the glass microstructure) the data does not definitely establish

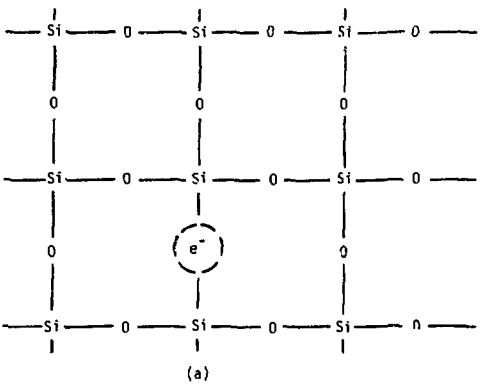

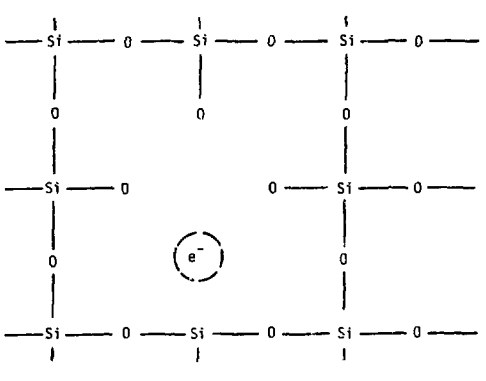

Figure 1.2 Proposed E' Defect Microstructures

This figure illustrates the nature of two of the proposed structures for E' defects.[22] In part (a), the E_1' defect is associated with the electron occupation of an oxygen atom vacancy. In part (b), the E_1' center is associated with the electron occupation of a Si-O vacancy.

that identical intrinsic defects occur in the crystalline and amorphous forms of SiO_2. Recognizing this limitation, it is often convenient to interpret E' spectra in fused silica as being due to unpaired electron spins at incompletely bonded silicon atoms.

Multicomponent silicate glasses are even more difficult systems to understand than fused silica. The microscopic structures of these glasses depend in detail on the specific glass composition, and the structures are rarely well-understood. Interpretation of EPR spectral data of extrinsic or intrinsic radiation induced paramagnetic centers in these glasses must be approached on an individual basis for each system. For complicated glasses, many of the component atomic species (B, K, Na, Ag, etc.) can be associated with paramagnetic centers which have qualitatively similar EPR characteristics. Thus, detailed analysis of EPR spectra in these glasses requires that the contributions from individual atomic species be extracted from the total spectrum before a consideration of the nature of the individual centers can even begin. In addition, multicomponent glasses often contain significant amounts of multivalent impurities which can be associated with radiation induced defects and add to the complicated nature of the EPR spectra.

C. Electron Paramagnetic Resonance

1. Introduction

The experiments to be described in this thesis consist of Electron Paramagnetic Resonance (EPR or ESR) measurements of the characteristics of radiation-induced paramagnetic centers in silicate glasses. EPR is sensitive only to those centers which are paramagnetic (associated with unpaired electron spins); but it is a versatile, sensitive technique for studying those centers which can be detected. For example, much of our data consists of absolute measurements of paramagnetic spin densities in glasses, with a typical effective sensitivity capability better than 10^{12} spins ΔH/c.c. (where ΔH is the spectral linewidth).

EPR is a technique which is used to investigate the resonant behavior of the bulk magnetization $\vec{M}$ due to the electronic magnetic dipoles in a material. The magnetic dipole $\vec{\mu}_i$ of a paramagnetic center is due to the total angular momentum associated with the unpaired electron spin of that center. In the simplest case, the dipole moment is related to the total angular momentum, $\vec{J}$, by the relation:

$$\vec{\mu}_i = - g\beta\vec{J}_i = \gamma\hbar\vec{J}_i \quad , \tag{1.7}$$

where g is the electronic "g" factor, β is the Bohr magnetron, γ is the gyromagnetic ratio and $\hbar$ is Planck's constant. For a free electron, this reduces to:

$$\vec{\mu}_e = - g_e\beta\vec{S} = \gamma_e\vec{S}\hbar \quad , \tag{1.8}$$

where g_e is the free electron g value:

$$g_e = 2.0023 \quad , \tag{1.9}$$

and

$$\gamma_e = - 1.7608 \cdot 10^8 \text{ sec}^{-1} \text{ gauss}^{-1} \tag{1.10}$$

is the gyromagnetic ratio.

When a paramagnetic center is subjected to a constant external magnetic field $\vec{H}_o$, there is a potential energy of interaction E_i given by:

$$E_i = - \vec{\mu}_i \cdot \vec{H}_o \quad . \tag{1.11}$$

For spin = 1/2 paramagnetic centers, this interaction defines a two energy level system with an energy difference ΔE between the two levels given by (see Fig. 1.3):

$$\Delta E = g\beta H_o = \gamma H_o \quad . \tag{1.12}$$

This is the basic equation describing paramagnetic resonance of an electronic dipole. When a spin 1/2 paramagnetic center is subjected to a static magnetic field H_o, there will be two energy levels for the electrons separated by ΔE.

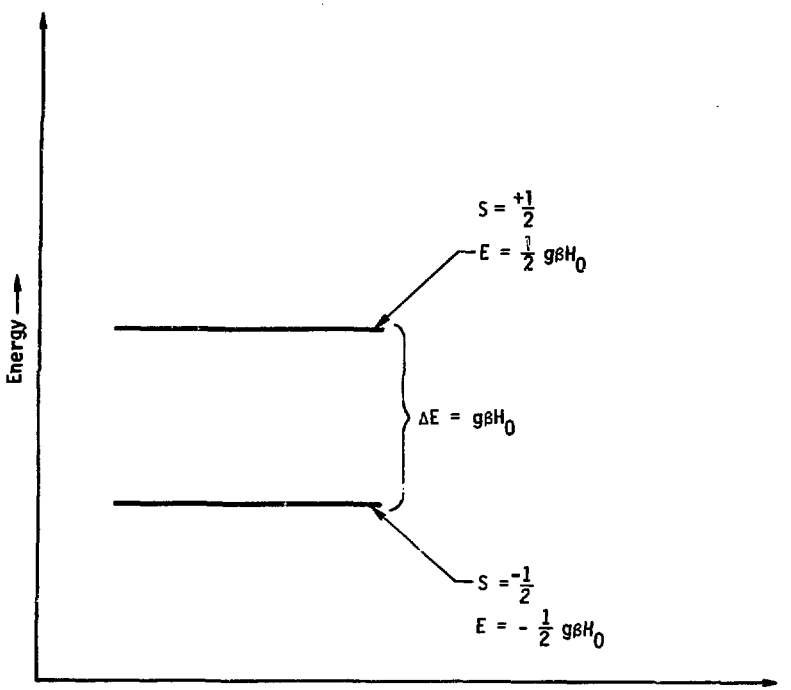

Figure 1.3 Spin 1/2 Energy Levels

This figure schematically describes the two-energy-level system which is associated with a spin 1/2 magnetic dipole in a magnetic field.

If an electromagnetic wave of frequency ω_0 (usually microwave frequency) where,

$$\hbar\omega_0 = \Delta E = g\beta H_0 \tag{1.13}$$

is applied to the center, then the wave will induce transitions between the two energy levels of Fig. 1.3. The resulting absorption (or emission) of energy by the paramagnetic center can then be detected electrically. If the absorption is recorded as the applied frequency ω or magnetic field H_0 is varied, the resulting data, or spectrum, will characterize the particular center in terms of its g-value and resonance lineshape.

When rewritten to emphasize the g-value of a paramagnetic center, Eq. (1.13) takes the form:

$$g = \frac{\hbar\omega_0}{\beta H_0} \quad . \tag{1.14}$$

Equations (1.13) and (1.14) are actually an idealized and somewhat misleading description of paramagnetic resonance. When the EPR spectrum of an ideal isolated spin 1/2 paramagnetic center is recorded, there will be a single, infinitely sharp "line" at the g-value of eq. (1.14), as in Fig. 1.4(a). In reality, the ensemble of paramagnetic centers in a macroscopic sample is perturbed by various interactions (e.g., crystal field, spin-spin, etc.) and the resulting observed EPR spectrum will have a finite width and some characteristic shape. This spectrum is frequently described as a distribution of g-values $g(\omega-\omega_0)$ about the center frequency ω_0 (see Fig. 1.4(b)). The spectral distribution $g(\omega-\omega_0)$ is often referred to as the "lineshape" of the resonance.

The paramagnetic samples studied in the laboratory actually consist of a large collection of paramagnetic centers. The bulk magnetic moment, or magnetization, $\vec{M}$ is due to the sum of the individual magnetic moments $\vec{\mu}_i$ in the sample:

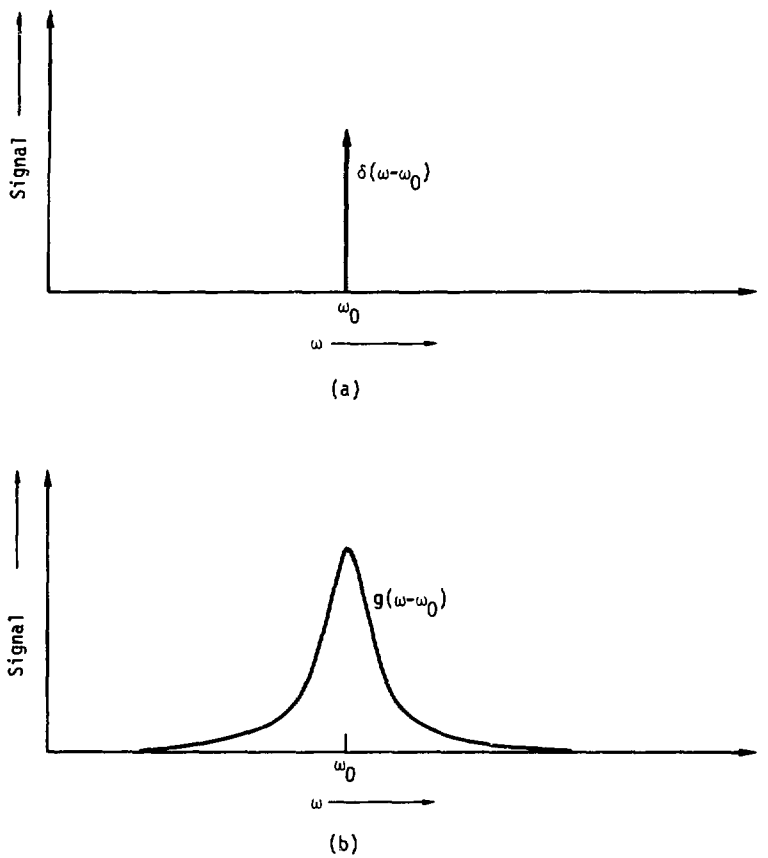

Figure 1.4 Elementary EPR Spectra

These figures illustrate two basic types of EPR spectra. In part (a), the spectrum of an isolated dipole is shown as an infinitely narrow delta-function. In part (b), the broadening of the delta function by external influences results in the resonance distribution function g $(\omega-\omega_0)$.

$$\vec{M} = \sum_{\text{sample}} \vec{\mu}_i \quad . \tag{1.15}$$

With no applied magnetic fields, the individual magnetic dipoles will be randomly oriented and the sample will have zero net bulk magnetization. But a constant applied magnetic field $\vec{H}_o$ (in the z-direction) will tend to align the dipoles in the z-direction. The resultant net bulk magnetic moment is determined by the population difference, N_o, at thermal equilibrium between the two energy levels of the system (see Fig. 1.3), given by:

$$N_o = N_t \left(\frac{1 - e^{-\frac{\Delta E}{kT}}}{1 + e^{-\frac{\Delta E}{kT}}} \right) \simeq N_t \frac{\Delta E}{2kT} \quad , \tag{1.16}$$

where N_t is the total number of centers, k is Boltzmann's constant and T is the system temperature. The resulting magnetization $\vec{M}$ is:

$$\vec{M} = |\vec{\mu}_i| N_o \hat{Z} \quad . \tag{1.17}$$

When $\Delta E << kT$, $\vec{M}$ can be rewritten in the form:

$$\vec{M} = \chi_o \vec{H}_o \quad , \tag{1.18}$$

where

$$\chi_o = g^2 \beta^2 \frac{N_t}{2\Delta kT} \quad , \tag{1.19}$$

and the total potential energy U of the system becomes:

$$U = - \vec{M} \cdot \vec{H}_o \quad . \tag{1.20}$$

When a paramagnetic sample is subjected to a time-dependent magnetic field $\vec{H}_1(t)$, the resulting magnetization can be described by a frequency-dependent susceptibility function $\chi(\omega)$:

$$\chi(\omega) = \chi'(\omega) + i\chi''(\omega) \quad , \tag{1.21}$$

and the resulting magnetization for a particular frequency ω is written:

$$\vec{M}(\omega) = \chi(\omega) \vec{H}_1(\omega) \quad . \tag{1.22}$$

The time dependence of the magnetization can be obtained from the Fourier transform of $\vec{M}(\omega)$:

$$\vec{M}(t) = \frac{1}{\sqrt{2\pi}} \int_{-\infty}^{\infty} \vec{M}(\omega) e^{-i\omega t} d\omega \quad . \tag{1.23}$$

The remainder of this section consists of a discussion of several aspects of the theory of EPR which are relevant to our experiments. Much of the discussion assumes considerable familiarity with EPR on the part of the reader; and there are a number of excellent sources for a more thorough discussion of the specific topics. Pake[28] gives a very clear and readable introduction to many of the topics which will be discussed, while Slichter,[29] and Abragam[30] are traditional sources which can be consulted for a more thorough presentation of the material. In addition, Poole,[31] and Alger[32] give presentations of the theory and related topics from an experimental perspective.

2. The Hamiltonian Operator (time-independent)

The magnetic resonance behavior of a paramagnetic electron depends on the nature of its microscopic environment. Eq. (1.12) is an extremely simplified description of the energy level splitting of an electron exposed to an external magnetic field. A detailed description of the energy level splitting of a paramagnetic electron requires a quantum mechanical description including a Hamiltonian operator and the corresponding electron wave functions. The Hamiltonian description is particularly useful because its form can be easily modified to describe a wide variety of paramagnetic systems.

A typical Hamiltonian for a single paramagnetic ion with a spin $\vec{S}$ in a solid might have the form:

$$H = H_{k.e.} + H_{ion} + H_{s.o.} + H_{cryst.} + H_Z + H_{d.d.} \tag{1.24}$$

Here, the first two terms describe the kinetic and Coulomb potential energy of the paramagnetic electron of an isolated ion, where

$$H_{k.e.} = \frac{-\hbar^2}{2m} \nabla^2 \quad , \tag{1.25}$$

and

$$H_{ion} = \frac{-Ze^2}{r_i} + \sum_{\substack{\text{other} \\ \text{electrons}}} \frac{e^2}{r_{ij}} \quad . \tag{1.26}$$

The third term of the Hamiltonian,

$$H_{s.o.} = \lambda \vec{L} \cdot \vec{S} \quad , \tag{1.27}$$

describes the interaction between the spin and orbital angular momentum of the unpaired electron spin of the ion. These first three terms of the Hamiltonian determine the ground state wave function and energy level of the isolated ion.

When the paramagnetic ion is placed in a solid, the fourth term, $H_{cryst.}$, is added to the Hamiltonian to describe the contribution to the electron energy due to the Coulomb electric potential of the microscopic local crystalline electric fields. In most cases, the ground state of an ionic paramagnetic electron in a solid is determined by a competition between the effects of $H_{s.o.}$ and $H_{cryst.}$. For some ionic species (such as rare earth ions) $H_{s.o.}$ is much more important than $H_{cryst.}$ and the ground state wave functions of the ion in a solid are basically the same as those for the corresponding free ion. For these cases, the paramagnetic behavior can often be predicted with the use of the free ion wave functions. However, there are other types of ions (such as transition metal elements) where the effects of $H_{cryst.}$ are much larger than $H_{s.o.}$ and the corresponding ground state wave functions will be determined by the microscopic environments associated with each specific material.

The two situations just described are two types of systems where the EPR behavior of a paramagnetic electron can be readily predicted on a theoretical basis; and there are many situations where this is not possible. For example, the EPR of ionic species for which $H_{s.o.}$ and $H_{cryst.}$ have comparable effects on the energy of the electron is very difficult to predict. In solids, electron or hole traps associated with intrinsic defects in the material microstructure are another case where the EPR behavior is difficult to predict. The E' centers in crystalline quartz is an excellent example of this situation. Here, the EPR spectra have been shown to be associated with an electron occupying an incompletely bonded silicon orbital,[16] but theoretical descriptions of the details of the EPR spectra remains an unsolved problem. In any case, the first four terms of the Hamiltonian in Eq. (1.24) are used to describe the fundamental characteristics of a paramagnetic center (i.e., they determine $\vec{L}$ and $\vec{S}$).

The splitting of the ground state energy levels due to the application of an externally applied magnetic field is described by the fifth term in the Hamiltonian of eq. (1.24). This term, the Zeeman interaction, can be written in the general form:

$$H_Z = \beta(\vec{L} + g_e\vec{S}) \cdot \vec{H}. \qquad (1.28)$$

Here, the $\vec{L}$ and $\vec{S}$ operators illustrate how the ground state wave functions, determined by the interactions described above, determine the EPR behavior of a particular paramagnetic center.

The final term in the Hamiltonian, H_{dd}, is used to describe the effects of local microscopic magnetic fields due to the presence of other nearby paramagnetic spins in the material. It is included here because it is an important contribution for some of our experiments. Eq. (1.24) includes only a few of the terms which are frequently used to describe paramagnetic systems. In general, the terms included in a specific Hamiltonian are

chosen on the basis of the relative magnitude of their contribution to the overall energy level structure of the system.

The Hamiltonian of eq. (1.24) is useful for describing the important interactions for a specific situation; but is very cumbersome for the interpretation of experimental EPR data. For interpretation of data, the Hamiltonian is frequently rewritten in a condensed form known as the "effective spin" Hamiltonian, H_{eff}:

$$H_{eff} = \beta \vec{H} \cdot \bar{\bar{g}} \cdot \vec{S} + D\left(S_z^2 - \frac{1}{3} S(S+1)\right) + E(S_x^2 - S_y^2) + H_{dd} \quad . \qquad (1.29)$$

Here, the various terms in the original Hamiltonian (Eq. (1.24)) have been absorbed in the constant coefficients of $\bar{\bar{g}}$, D and E. In this representation, the g tensor $\bar{\bar{g}}$ specifies the Zeeman structure of an EPR spectra, while the constants D and E describe the "fine structure" contributions.

For many situations, only the first term of the Hamiltonian of eq. (1.29) is needed to specify the major features of a spectrum:

$$H_{eff} \simeq \beta \vec{H} \cdot \bar{\bar{g}} \cdot \vec{S} \quad . \qquad (1.30)$$

The g tensor, a second-rank tensor with three independent elements, is the three dimensional analog of the g-value in equation (1.7). In crystalline materials, the g-tensor can be specified by its three principal values g_x, g_y and g_z. For systems with any type of axial symmetry, the g tensor can be characterized by the two g-values $g_{||}$ and $g_{\perp}$. Here $g_{||}$ is the g-value associated with the axis of symmetry, and $g_{\perp}$ is the "perpendicular" or orthogonal g-value.

3. Rate Equations

In order to understand the results of an EPR measurement, it is necessary to consider the temporal as well as the static aspects of EPR. The attainment of thermal equilibrium between a paramagnetic spin system and its environment is a time dependent process which imposes well defined limitations on the range of experimental parameters which can be

used to record an EPR spectrum. And conversely, the presence of these limitations is related to characteristics of paramagnetic spin systems which cannot be expressed in terms of the time-independent system Hamiltonian. Hamiltonians are generally cumbersome in the description of temporal aspects of EPR because they require the use of time dependent perturbation theory.

One of the simplest time dependent descriptions of a paramagnetic system is the rate equation approach. Rate equations describe the evolution of energy level populations subject to external driving forces and internal relaxation. In a rate equation description, a collection of spin 1/2 paramagnetic centers is described as a collection of identical two-level systems with energy level separation ΔE (see Fig. 1.3):

$$\Delta E = g\beta H_0 = \hbar\omega_0 \quad . \tag{1.13}$$

Under conditions of thermal equilibrium, the relative populations of the spin energy levels is given by:

$$\frac{N^+}{N^-} = e^{-\frac{\Delta E}{kT}} \quad . \tag{1.31}$$

Here, N^+ and N^- are the populations of the upper and lower energy levels, respectively, and

$$N = N^+ + N^- \tag{1.32}$$

is the total number of spins (or paramagnetic centers) in the system. A high-frequency (microwave) magnetic field with amplitude H_1 and frequency ω applied to the system will induce transitions between the two energy levels. Under these conditions, a competition will exist between thermal equilibration processes which always tend to establish the relative populations of eq. (1.31) and the microwave induced transitions which tend to equalize the energy level populations. This process is described by the "rate equation:"[32,33]

$$\left(\frac{dn}{dt}\right) = \left(\frac{dn}{dt}\right)_{mw} + \left(\frac{dn}{dt}\right)_{sl} \quad , \tag{1.33}$$

where

$$n = N^{+} - N^{-} \tag{1.34}$$

is the population difference between the two levels, $(dn/dt)_{mw}$ is the rate of microwave-induced transitions:

$$\left(\frac{dn}{dt}\right)_{mw} = -\pi\gamma^2 H_1^2 g(\omega - \omega_0)\, n \quad , \tag{1.35}$$

and $(dn/dt)_{sl}$ is the rate of thermally induced transitions:

$$\left(\frac{dn}{dt}\right)_{sl} = \left(\frac{n_0 - n}{T_1}\right) \quad . \tag{1.36}$$

Here, T_1, the longitudinal or "spin-lattice" relaxation time, is the time constant characterizing the approach of the spin system to thermal equilibrium with its environment. Also, $g(\omega - \omega_0)$ is the g-value distribution function of the resonance and is normalized such that:

$$\int_{-\infty}^{\infty} g(\omega - \omega_0)\, d\omega = 1 \tag{1.37}$$

When variations in the applied microwave power are small during time intervals on the order of T_1, steady state solutions of eq. (1.33) may be used to determine the equilibrium energy level populations during magnetic resonance. Thus, when

$$\left(\frac{dn}{dt}\right) = 0 \quad , \tag{1.38}$$

we obtain:

$$n(\omega) = \frac{n_0}{1 + \pi\gamma^2 H_1^2 T_1 g(\omega - \omega_0)} \tag{1.39}$$

This result can be directly used to determine the imaginary portion of the magnetic susceptibility, $\chi''(\omega)$. For a rotating field with amplitude H_1,

the microwave power absorbed can be written:

$$P_{mw} = \frac{1}{2}\omega\chi''(\omega)(2H_1)^2 \quad , \tag{1.40}$$

where $2H_1$ is the linear magnetic field required to create a rotating component with amplitude H_1. But the microwave power absorbed can also be written:

$$P_{mw} = \frac{1}{2}\hbar\omega\left(\frac{dn}{dt}\right)_{mw} \quad , \tag{1.41}$$

where the 1/2 is necessary because each induced transition changes n by two, but absorbs only one photon. Using eqs. (1.35), (1.39-1.41) we obtain:

$$\chi''(\omega) = \frac{1}{2}\chi_0\omega_0 \frac{\pi g(\omega - \omega_0)}{1 + \pi\gamma^2 H_1^2 g(\omega - \omega_0)T_1} \quad . \tag{1.42}$$

This result is often rewritten in the form:

$$\chi''(\omega) = \frac{1}{2}\chi_0\omega_0 \frac{\pi g(\omega - \omega_0)}{1 + S'} \quad , \tag{1.43}$$

where S', the "saturation parameter," is:

$$S' \equiv \pi\gamma^2 H_1^2 T_1 g(\omega - \omega_0) \quad . \tag{1.44}$$

The result of eq. (1.43) can be used to illustrate some simple aspects of the power saturation of an EPR resonance. For very low microwave powers ($S' << 1$), we see that the amplitude of the observed $\chi''(\omega)$ is independent of the applied power and has a "lineshape" which is the same as that of $g(\omega - \omega_0)$. But for large applied microwave powers ($S' >> 1$), the amplitude of $\chi''(\omega)$ "saturates," or decreases as $1/S'$ with increases in applied power and will have a much different lineshape (becoming independent of microwave frequency) than $g(\omega - \omega_0)$.

4. The Bloch equations

Rate equations serve as an extremely useful format for description of resonant absorption and thermal relaxation processes associated with the z-component of the magnetization. However, there is a variety of phenomena involving the dynamic behavior of the transverse

components of the magnetization (M_x and M_y) which cannot be described by rate equations. For a time dependent description of all three components of the megnetization, the Bloch equations are frequently used.

The Bloch equations are a set of three linear coupled differential equations which describe the time dependence of the magnetization $\vec{M}(t)$ due to a collection of independent identical spins subjected to a magnetic field $\vec{M}(t)$:

$$\frac{dM_x(t)}{dt} = \gamma\left(\vec{H}(t)\times\vec{M}(t)\right)_x - \frac{M_x(t)}{T_2}$$

$$\frac{dM_y(t)}{dt} = \gamma\left(\vec{H}(t)\times\vec{M}(t)\right)_y - \frac{M_y(t)}{T_2}$$

$$\frac{dM_z(t)}{dt} = \gamma\left(\vec{H}(t)\times\vec{M}(t)\right)_z - \frac{M_z - M_0}{T_1} \quad , \tag{1.45}$$

where M_x, M_y and M_z are the vector components of the magnetization, T_1 is the spin-lattice or "longitudinal" relaxation time which characterizes thermal processes involving energy transfer between the spin system and its host lattice (the same as the T_1 in the rate equation of eq. (1.33)), and T_2 is the spin-spin or "transverse" relaxation time, also known as the "phase coherence" time of the spin system.

Solutions of the Bloch equations can be used for a wide variety of experimental situations. Since we are mainly interested here in continuous-wave measurement of paramagnetic susceptibilities, we present in eqs. (1.46) steady state solutions of the Bloch equations in the form known as "slow passage" solutions:[28]

$$\chi'(\omega) = \frac{1}{2}\chi_0\omega_0 T_2 \frac{T_2(\omega_0 - \omega)}{1 + T_2^2(\omega - \omega_0)^2 + \gamma^2 H_1^2 T_1 T_2}$$

$$\chi''(\omega) = \frac{1}{2}\chi_0\omega_0 T_2 \frac{1}{1 + T_2^2(\omega - \omega_0)^2 + \gamma^2 H_1^2 T_1 T_2} \quad . \tag{1.46}$$

These solutions have assumed the presence of a large, static magnetic field $\vec{H}_0$ in the z-direction, and a small transverse microwave magnetic field with amplitude H_1 and frequency ω. The "slow passage" label derives from the assumed restrictions (necessary to derive eqs. (1.46)) on the time derivatives of the large "static" magnetic field H_0 or the frequency ω. The most demanding of these restrictions can be stated in the form:

$$\frac{1}{|H_1|}\frac{d|H_0|}{dt} \ll \gamma|H_1| \tag{1.47}$$

This condition is known as "adiabatic passage" and is generally fairly easy to satisfy in the laboratory.

The solution for $\chi''(\omega)$ in eqs. (1.46) can be rewritten in the form:

$$\chi''(\omega) = \left[\frac{1}{2}\frac{\chi_0\omega_0}{1+S}\right] \frac{1}{1+\frac{T_2^2}{1+S}(\omega-\omega_0)^2}, \tag{1.48}$$

where

$$S = \gamma^2 H_1^2 T_1 T_2 \tag{1.49}$$

is similar to the saturation parameter S' defined in eq. (1.44). When written in this form it is seen that $\chi''(\omega)$ has a Lorentzian functional form (due to the assumed exponential decays in eqs. (1.45)). As with the rate equation solution, the amplitude of $\chi''(\omega)$ "saturates" with increases in the applied microwave power by the factor $1/(1+S)$. In addition, because of the specific Lorentzian form, we see that the full width at half maximum of the resonance at $\omega = \omega_0$ exhibits "saturation broadening" and is given by:

$$\Delta\omega_{fwhm} = \frac{2\sqrt{1+S}}{T_2} \tag{1.50}$$

For one particular choice of $g(\omega - \omega_0)$ the solution for $\chi''(\omega)$ of eqs. (1.46) can be seen to be identical to the rate equation solution of eq. (1.42). Substitution of

$$g(\omega - \omega_0) = \frac{T_2}{\pi} \frac{1}{1 + T_2^2(\omega - \omega_0)^2} \tag{1.51}$$

into eq. (1.42) will verify that the two solutions are identical. We see here that there are certain situations where rate equations and the Bloch equations are completely consistent with each other. Each of these approaches to a mathematical descriptions has its advantage. The usefulness of rate equations derives from their mathematical simplicity together with the inherent generality contained in the lineshape function $g(\omega - \omega_0)$. On the other hand, the advantage of the Bloch equations comes from the more detailed description which is possible with the three dimensional magnetization vector $\vec{M}(t)$ and the two relaxation times T_1 and T_2.

5. Homogeneous Spin Systems

The lineshape function $g(\omega - \omega_0)$ of an EPR spectrum is determined by the nature of the specific paramagnetic system. Homogeneous spin systems are a common and important type of spin system which consist of a collection of identical paramagnetic spins. The form of the lineshape function $g(\omega - \omega_0)$ for a homogeneous system depends on the nature of the dominant homogeneous "broadening" mechanism of the system. Typical homogeneous broadening mechanisms include the spin-lattice interaction, dipole-dipole broadening between like spins and saturation broadening. Paramagnetic homogeneous spin systems are a basic, simple and important type of spin system in EPR. Homogeneous systems are particularly useful because they are well understood and can be used to explain the behavior of more complicated systems. The EPR characteristics of homogeneous systems also serve as a common reference point for comparison of the EPR of different types of systems.

Because homogeneous systems consist of a collection of identical spins, the behavior of the entire ensemble of spins in the system can be

expressed in terms of the behavior of a single spin center. For example, during EPR, each of the spins in the system will have equal probability of absorbing power from the incident microwave field; and the absorption of the entire system is the same as the absorption probability for one spin multiplied by the total number of spins in the system. As a result, the individual spins of a homogeneous system always remain in internal thermal equilibrium with each other during EPR and all of the spins behave identically.

The Bloch equations describe the EPR behavior of homogeneous spin systems, because all of the spin centers are characterized by the same g-value and relaxation times, T_1 and T_2. The paramagnetic susceptibility of a homogeneous system can be obtained directly from the Bloch equations solutions of eqs. (1.46). The unsaturated ($S << 1$) behavior of these solutions can be obtained by taking the limit as $H_1 \to 0$. We find for the susceptibility $\chi''(\omega)$:

$$\chi''(\omega) = \frac{1}{2} \chi_0 \omega_0 T_2 \frac{1}{1 + T_2^2(\omega - \omega_0)^2} \quad . \tag{1.52}$$

We see that the Lorentzian form, or "lineshape," of $\chi(\omega)$ is centered at ω_0 and has a full-width at half-maximum of:

$$\Delta\omega_{fwhm} = \frac{2}{T_2} \tag{1.53}$$

This lineshape and its derivative are illustrated in Fig. 1.5.

6. Inhomogeneous Spin Systems

Inhomogeneous systems consist of collections of different kinds of spin centers. The differences between centers may be due to variations in the local spin environment or may be due to intrinsic differences in the nature of the center. Inhomogeneous systems are often extremely complicated and difficult to investigate. EPR is one technique which is frequently used to study inhomogeneous systems and forms a major

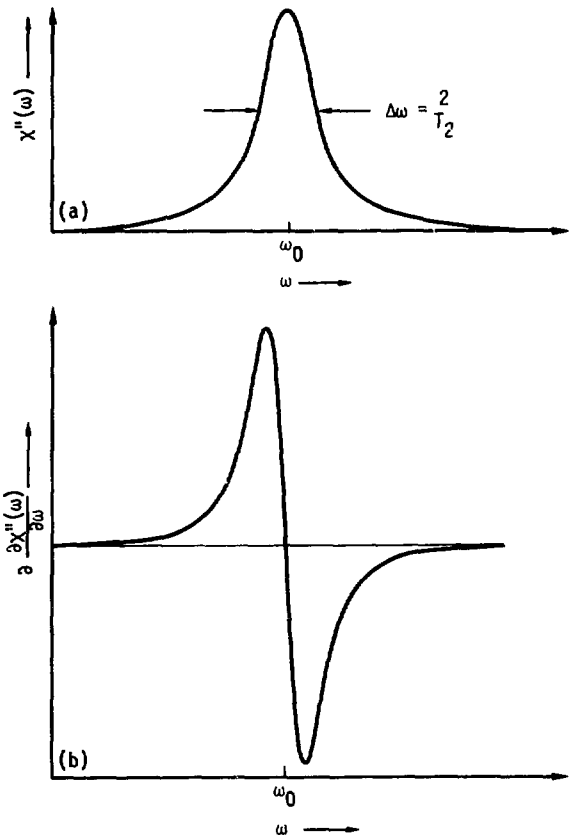

Figure 1.5 Homogeneous Lorentzian Lineshapes

These figures demonstrate two different ways to display an EPR spectrum. In part (a), the resonant absorption due to $\chi''(\omega)$ with a Lorentzian lineshape is shown as a function of ω. In part (b), the derivative (with respect to ω) of the absorption lineshape is plotted as a function of ω.

topic of this thesis. In order to interpret some of the data to be presented, there are a number of aspects of EPR in inhomogeneous systems which must be explored.

In many cases, the behavior of inhomogeneous spin systems can be understood in terms of the behavior of homogeneous systems; but there are many differences in the behavior of the two types of systems. For example, because inhomogeneous systems are composed of a collection of different centers, energy absorbed during EPR is generally not uniformly distributed to the entire spin system. As a result, the spins of an inhomogeneous system are not necessarily in thermal equilibrium with each other.

One type of inhomogeneous system that is particularly important in this thesis consists of a collection of similar spin centers which are subjected to different microscopic or macroscopic environments. This type of inhomogeneous system can be thought of as being composed of a collection of distinct homogeneous subsystems or "spin packets." The EPR of each of the spin packets can be characterized by the same values of the relaxation times, T_1 and T_2, but will be distinguished by different g-values. Inhomogeneous spin systems consisting of a distribution of homogeneous spin packets occur in many paramagnetic substances; and typical inhomogeneous "broadening" mechanisms for such systems include variations in the local crystalline electric fields, variations in the resonance g-value due to g-tensor anisotropy and variations from center to center in externally applied fields.

Because they can accommodate only one set of relaxation times and g-value at a time, the Bloch equations are incapable of directly describing the magnetic resonance behavior of inhomogeneous systems. But if the inhomogeneous system consists of a distribution of homogeneous spin packets which can each be individually described by the Bloch equations, then the behavior of the entire inhomogeneous line can be expressed as a sum of the contributions from the spin packets. Using this approach, it is possible

to construct expressions describing the paramagnetic susceptibility of inhomogeneous systems.

In order to describe an inhomogeneous system, it is necessary to specify two different frequency or "lineshape" distributions. The first, $g(\omega - \omega_0)$ is the lineshape function of an individual spin packets. For most of the following discussion, $g(\omega - \omega_0)$ is assumed to be a normalized Lorentzian with a full-width at half-maximum of $2/T_2$ (see eq. 1.51). Within a given inhomogeneous distribution, all of the spin packets will be assumed to be described by the same T_1 and T_2, but there will be a variation in the resonant frequency ω_0 (or g-value) from packet to packet. The second lineshape function $h(\omega - \omega_0)$ describes the distribution of spin packet center frequencies ω_0 across the inhomogeneous distribution and has a width in frequency space designated by $\frac{1}{T_2^*}$ (see Fig. 1.6). The form of $h(\omega - \omega_0)$ depends on the nature of the particular system of interest. In the discussion which follows, both $g(\omega - \omega_0)$ and $h(\omega - \omega_0)$ are assumed to be normalized functions:

$$\int_0^\infty g(\omega - \omega_0)\, d\omega = \int_0^\infty h(\omega - \omega_0)\, d\omega = 1 \qquad (1.54)$$

In order to construct an expression for the unsaturated susceptibility of an inhomogeneous system, it is necessary to begin with the contribution to the susceptibility from an individual spin packet. From the rate equation solution of eq. (1.42), we obtain for the unsaturated susceptibility $\chi_{sp}''(\omega)$ of a single spin packet centered at ω':

$$\chi_{sp}''(\omega) = \frac{\pi}{2} \chi_0 \omega' g(\omega - \omega') \qquad (1.55)$$

The unsaturated susceptibility $\chi''(\omega)$ of the entire inhomogeneous system can be obtained by integrating the contributions of individual spin packets across the entire inhomogeneous distribution:

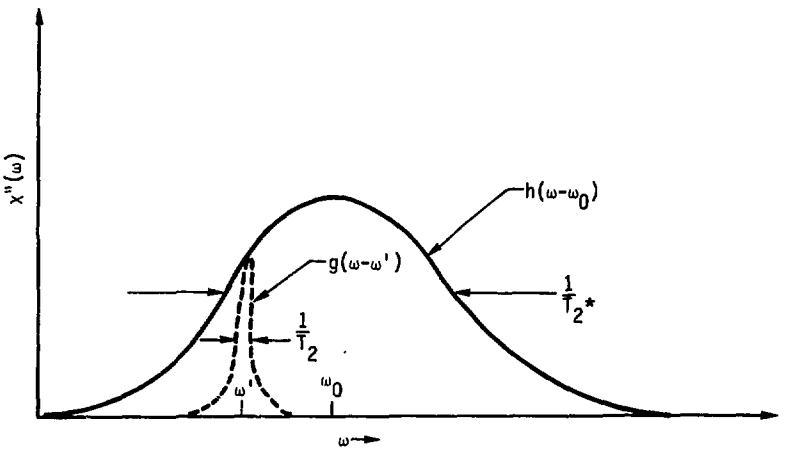

Figure 1.6 Inhomogeneous Distribution Functions

This figure illustrates the different distribution functions and relaxation times which are used to specify the nature of an inhomogeneous system. $g(\omega-\omega')$ describes the nature of individual "spin packets" in the system, while $h(\omega-\omega_0)$ describes the spectral distribution of the packets.

$$\chi''(\omega) = \frac{\pi}{2}\chi_0 \int_0^\infty \omega' g(\omega - \omega') h(\omega' - \omega_0)\, d\omega' \qquad (1.56)$$

In the case when the overall inhomogeneous broadening is much greater than the homogeneous spin packet width, the only important contributions to this integral occur when $\omega' \approx \omega$ and the integral becomes unnecessary, yielding:[33,34]

$$\chi''(\omega) = \frac{\pi}{2}\chi_0 \omega h(\omega - \omega_0) \qquad (1.57)$$

Thus the $\chi''(\omega)$ of an extremely inhomogeneous system (i.e., $T_2^* \ll T_2$) has a lineshape which is the same as the inhomogeneous distribution. These results are too vague to be useful for most experimental situations, and were derived in order to illustrate the procedure. The corresponding results for inhomogeneous systems with Lorentzian spin packets, retaining the effects of power saturation are much more useful and are presented below.

7. EPR Power Saturation

The power saturation of continuous wave EPR signals is determined by the relaxation times T_1 and T_2 and the homogeneous and inhomogeneous broadening mechanisms of the particular spin system. Power saturation of EPR spectra is a consequence of the fact that there is a finite limit on the amount of power which the spin-lattice relaxation mechanisms of a paramagnetic spin system can transfer to lattice vibration excitations. Roughly speaking, if the spin lattice relaxation time of a paramagnetic system is T_1, and ΔE is the resonant energy level difference (see eq. 1.13), then the maximum power P_m which can be continuously absorbed by the system is:

$$P_m \approx N \frac{\Delta E}{T_1} \quad , \qquad (1.58)$$

where N is the number of spins in the system. This limitation on the power absorption capability of a spin system leads to the saturation of EPR signals. On the other hand, eq. (1.58) shows that the presence of these limitations can be used to investigate the T_1 associated with the system. In fact, detailed observations of saturation behavior can be used to determine T_1 and T_2 and their relationship with other experimental variables. Some of the theory associated with these techniques will be discussed below.

The discussion below will describe the power saturation behavior of homogeneous and inhomogeneous systems. The purpose of the discussion is to illustrate the ways in which EPR power saturation measurements can be used to determine the relaxation times T_1 and T_2 of a system. The saturation behavior of homogeneous systems will be considered first and will be discussed in terms of solutions to the Bloch equations. The saturation behavior of inhomogeneous systems will then be considered, and, following the analysis of Portis,[33] will be discussed in terms of the saturation behavior of homogeneous systems.

The power saturation behavior of homogeneous sytems can be completely determined from the solutions to the Bloch equations of eqs. (1.48-50). In eq. (1.48) we see that the amplitude of $\chi''(\omega)$ is proportional to the factor $(1+S)^{-1}$. Since the power absorbed in EPR is proportional to $H_1^2 \chi''(\omega)$, for very low incident microwave power ($S << 1$) the absorbed power is proportional to H_1^2 because the amplitude of $\chi''(\omega)$ becomes independent of the incident power:

$$P_a \propto H_1^2 \chi''(\omega) \propto H_1^2 \quad . \tag{1.59}$$

This corresponds to a situation where the incident microwave power is much less than the maximum power P_m which the system can absorb, and any small increases in the incident microwave power will be absorbed in accordance

with eq. (1.59). However, when the incident microwave power is very large ($S >> 1$), the spin system will be absorbing the maximum possible power P_m. Under these conditions, increases in the microwave power will not lead to increases in absorbed power, and the absorbed power becomes a constant, independent of the incident power, and we have:

$$P_a \propto H_1^2 \chi''(\omega) = \text{const.} \tag{1.60}$$

As a result, for saturated conditions ($S >> 1$), we see that $\chi''(\omega)$ is proportional to H_1^{-2}.

Relations (1.59) and (1.60) can be used to determine the product T_1T_2 of a system. For very low incident microwave power, an EPR signal can be used to determine a quantity Q_u which is proportional to the unsaturated susceptibility $\chi''(\omega)$ at line center ($\omega = \omega_o$):

$$Q_u(\omega_o) \propto \chi''(\omega) = \frac{1}{2} \chi_o \omega_o \chi_u(\omega_o) \quad , \tag{1.61}$$

where $\chi''(\omega)$ is the unsaturated susceptibility.

If the same measurement is performed for saturating levels of incident microwave power ($S >> 1$), then the resulting quantity, Q_s, can be written:

$$Q_s(\omega_o) \propto \chi''(\omega_o) = \frac{\frac{1}{2} \chi_o \omega_o \chi_u(\omega_o)}{1 + S} \tag{1.62}$$

The quantities shown in equations (1.61) and (1.62) can be used to determine T_1T_2, because taking the ratio Q_s/Q_u yields:

$$\frac{Q_s}{Q_u} = 1 + S = 1 + \gamma^2 H_1^2 T_1 T_2 \tag{1.63}$$

Thus, since S and H_1 are experimentally determined quantities, eq. (1.63) determines T_1T_2 for the system. This illustrates the theory behind the techniques by which measurements of the power saturation of the amplitude of $\chi''(\omega)$ can be used to determine T_1T_2 for homogeneous systems.

If a determination of either T_1 or T_2 can be made for a system, then the result for T_1T_2 can be used to determine both T_1 and T_2. For homogeneous spin systems, T_2 can be determined from a measurement of the unsaturated spectral linewidth of an EPR spectrum (using eq. 1.53):

$$T_2 = \frac{2}{\Delta\omega_{fwhm}} \tag{1.64}$$

Using eqs. (1.63) and (1.64) together can be used to determine T_1 and T_2 for a homogeneous system. These results are useful because they illustrate that continuous wave EPR measurements can be used to determine the relaxation times T_1 and T_2 of homogeneous spin systems.

Measurements of the power saturation of the susceptibility $\chi''(\omega)$ can also be used to determine the relaxation times associated with some inhomogeneous systems. Because of this greater complexity, it is more difficult to use saturation measurements to determine T_1 and T_2 for an inhomogeneous system than for an homogeneous system. In order to discuss inhomogeneous saturation, it is necessary to develop appropriate expressions for the saturated inhomogeneous susceptibility $\chi''(\omega)$. As with the unsaturated $\chi''(\omega)$ for inhomogeneous systems, it is convenient to begin with the expression for the paramagnetic susceptibility of a single spin packet (from eq. 1.39):

$$\chi_{sp}''(\omega) = \frac{\pi}{2}\chi_o\omega_o \frac{g(\omega - \omega_o)}{1 + \pi\gamma^2H_1^2T_1g(\omega - \omega_o)} \tag{1.65}$$

The susceptibility of the entire inhomogeneous system is obtained by integrating the individual spin packet contributions across the entire inhomogeneous distribution:

$$\chi''(\omega) = \frac{\pi\chi_o}{2}\int_0^\infty \frac{\omega' g(\omega - \omega')h(\omega' - \omega_o)}{1 + \pi\gamma^2H_1^2T_1g(\omega - \omega')}\, d\omega' \quad . \tag{1.66}$$

Portis[33] has shown that when the homogeneous spin packet width is negligible when compared to the width of the inhomogeneous distribution, i.e.,

$$\frac{1}{T_2} << \frac{1}{T_2^*} \quad , \tag{1.67}$$

then eq. (1.66) for the inhomogeneous susceptibility $\chi''(\omega)$ can be written as:

$$\chi''(\omega) = \frac{\pi}{2} \chi_0 \omega h(\omega - \omega_0) \int_0^\infty \frac{g(\omega - \omega')\, d\omega'}{1 + \pi\gamma^2 H_1^2 T_1 g(\omega - \omega')} \tag{1.68}$$

This equation illustrates two interesting features of EPR in inhomogeneous systems. First, the lineshape of $\chi''(\omega)$ is essentially the same as the form of the inhomogeneous distribution $h(\omega - \omega_0)$. Secondly, eq. (1.68) shows that the saturation of the amplitude of $\chi''(\omega)$ for an inhomogeneous system for which $T_2 >> T_2^*$ is determined completely by the nature of the homogeneous spin packet distribution $g(\omega - \omega')$.

The precise form of $\chi''(\omega)$ obtained from eq. (1.68) depends on the specific form of the function $g(\omega - \omega')$; but for Lorentzian spin packets (see eq. (1.51)), the integral can be completed and yields:

$$\chi''(\omega) = \frac{\pi}{2} \chi_0 \omega \frac{h(\omega - \omega_0)}{\sqrt{1 + S}} \tag{1.69}$$

Here, we see that the lineshape of $\chi''(\omega)$ is determined by the inhomogeneous distribution $h(\omega - \omega_0)$ and that the amplitude of $\chi''(\omega)$ saturates as $(1 + S)^{-1/2}$. This result is valid as long as there are no unusual energy absorption phenomena due to unusual features in the distribution $h(\omega - \omega_0)$ and as long as the spectral width of the system spin packets is much less than the overall width of the inhomogeneous distribution. However, there is a limit on the amount of microwave power which can be accommodated by eqs. (1.68) and (1.69). For high levels of microwave power ($S >> 1$), saturation broadening can broaden individual spin packets to the extent that they are as wide as, or wider than, the inhomogeneous width ($2/T_2^*$). From eq. (1.50) we see

that the effective width of a saturation broadened spin packet can be written:

$$\Delta\omega_{sp} = \frac{2\sqrt{1+S}}{T_2} \tag{1.70}$$

If sufficient microwave power is applied to the system so that:

$$\frac{\sqrt{1+S}}{T_2} \geq \frac{1}{T_2^*} \tag{1.71}$$

then the spin packet width is no longer less than the inhomogeneous width and eqs. (1.68) and (1.69) will no longer be valid. Thus, eqs. (1.68) and (1.69) are valid only as long as:

$$\frac{\sqrt{1+S}}{T_2} < \frac{1}{T_2^*} \tag{1.72}$$

Equation (1.69) is a result of the specific Lorentzian form chosen for $g(\omega - \omega')$ in eq. (1.68), but some aspects of this result apply to a broad class of inhomogeneous systems. For large incident microwave fields (i.e., $S \gg 1$), $\chi''(\omega)$ in eq. (1.69) behaves as:

$$\chi''(\omega) \propto \frac{1}{\sqrt{S}} \propto \frac{1}{H_1} \tag{1.73}$$

This type of characteristic behavior for the saturation of the amplitude of $\chi''(\omega)$ can be shown by some fairly simple arguments to apply to inhomogeneous systems which are composed of homogeneous spin packets which can absorb only a limited amount of power, as in eq. (1.58).

For saturating levels of an incident microwave field with frequency ω_i in an inhomogeneous system, the width of the homogeneous spin packet $\Delta\omega_{sp}$ centered at ω_i is given by eq. (1.70). And when $S \gg 1$, the power absorbed by the spin packet centered at ω_i approaches the maximum power possible, defined in eq. (1.58). Under conditions of saturated EPR in an inhomogeneous system, all spin packets within γH_1 of the frequency ω_i will be absorbing nearly the maximum possible power. Spin packets outside the

interval γH_1 from ω_1 will be absorbing power more weakly through the "wings" of their individual homogeneous distributions. Here, we see that the number of saturated spin packets in the system is proportional to γH_1. Under these conditions, increases in the applied microwave power lead to increases in the absorbed power because the number of spin packets contained in the interval γH_1 increases with H_1. Thus, increases in the absorbed power are not due to increases in the power absorbed by saturated spin packets, but is due rather to increases in the number of spin packets which can be "reached" by the microwave field. Thus, the total power absorbed becomes proportional to H_1:

$$P_a \propto H_1 \tag{1.74}$$

From eq. (1.59), we see that this implies:

$$\chi''(\omega) \propto \frac{1}{H_1} \propto \frac{1}{\sqrt{S}} \quad , \tag{1.73}$$

which is the same behavior which we obtained for the power saturation of $\chi''(\omega)$ with Lorentzian spin packets in eq. (1.69).

These results are similar to the results obtained for homogeneous systems and can be used to determine the relaxation time product T_1T_2. For homogeneous systems we have shown that $\chi''(\omega)$ saturates as S^{-1}, and that measurements of the saturation of the amplitude of $\chi''(\omega)$ as a function of S determines T_1T_2. For inhomogeneous systems we have found that $\chi''(\omega)$ saturates as $S^{-1/2}$; and here also, measurements of the saturation of the amplitude of $\chi''(\omega)$ as a function of S can be used to determine the product T_1T_2. For inhomogeneous systems, these results require only that there be no unusual energy absorption mechanisms associated with unusual features in the inhomogeneous distribution $h(\omega - \omega_0)$ and that the amount of power which can be absorbed by a single spin packet have an upper limit (as in eq. (1.58)). In addition, the applied microwave power must conform with the

limitation defined in (eq. (1.72)), so that the saturation broadened spin packet spectral width is less than the inhomogeneous width of the system.

For some situations, it is possible to apply sufficient microwave power to an inhomogeneous system so that individual spin packets are saturation broadened to the point where the spin packet spectral width is comparable to the total spectral width of the inhomogeneous distribution. Under these conditions, we would have:

$$\frac{1}{T_2^*} \approx \frac{\sqrt{1 + S}}{T_2} \tag{1.75}$$

and the system would no longer be strongly inhomogeneous. When the condition of eq. (1.75) is established in a spin system, equations (1.68) and (1.69) will not correctly describe the saturation behavior of a system, because the derivation of these results effectively assumed

$$\frac{1}{T_2^*} >> \frac{\sqrt{1 + S}}{T_2} \tag{1.76}$$

(or, that the system was strongly inhomogeneous). For situations where the saturation broadened spin packet width is comparable to the inhomogeneous width of the system, the saturation of the amplitude will have a behavior somewhere between the behavior expected for homogeneous and inhomogeneous systems: For homogeneous systems, $\chi''(\omega)$ saturates as $(1 + S)^{-1}$; while for inhomogeneous systems, $\chi''(\omega)$ saturates as $(1 + S)^{-1/2}$. This transition in behavior due to the increase in homogeneous broadening in a system (i.e., saturation broadening) in an inhomogeneous system is interesting because it suggests that for spin systems which are only mildly inhomogeneous:

$$\frac{1}{T_2} \approx \frac{1}{T_2^*} \quad , \tag{1.77}$$

the saturation of $\chi''(\omega)$ will occur no more "rapidly" (with increases in microwave power) than $(1 + S)^{-1}$, and no more "slowly" than $(1 + S)^{-1/2}$. Thus, it is possible to approximately characterize the saturation of the

amplitude of $\chi''(\omega)$ of an inhomogeneous system, even when the precise nature of the spectral distributions of the system are not well-specified.

The results of this discussion can be used to determine the relaxation time product T_1T_2 for different spin systems. Roughly speaking, for high levels of saturation ($S >> 1$) it has been shown that (from eqs. (1.69) and (1.73)):

$$T_1T_2 \propto \frac{1}{\gamma^2 H_1^2 [\chi''(\omega)]^{\alpha}} \quad , \tag{1.78}$$

where, for homogeneous systems α is 1, for strongly inhomogeneous systems α is 2, and for systems which are mildly inhomogeneous α is somewhere between 1 and 2. If a measurement of T_1 or T_2 can be made on the system, then both T_1 and T_2 will be determined. For homogeneous systems, it has been pointed out that a measurement of the unsaturated spectral width of a resonance can be used to determine T_2. For inhomogeneous systems, the unsaturated spectral width cannot be directly measured because it is obscured by the inhomogeneous distribution of the system. However, in some cases, it is possible to use measurements of saturation broadening to determine the T_2 of an inhomogeneous system. For example, if the experimental conditions allow sufficient power to be applied to the system so that the saturation broadened spin packet spectral width is greater than the inhomogeneous width of the system, then, from eq. (1.70),

$$T_2 = \frac{\Delta\omega_{sp}}{2\sqrt{1+S}} \quad . \tag{1.79}$$

Here, both $\Delta\omega_{sp}$ and S are experimentally measurable quantities, and T_2 can be determined. Thus, for this type of inhomogeneous system, both T_1 and T_2 can be determined from continuous wave saturation measurements.

8. Powder Lineshapes

The final topic which will be discussed in this section is EPR powder lineshapes. Powder lineshapes are EPR spectra which result

from an angular average of the orientation dependent g-values associated with the three-dimensional g-tensor (see eq. (1.30)). These lineshapes are encountered in systems which have no characteristic angular orientation throughout a sample, such as liquids, powders and glasses. They are important here because most of the data to be presented in this thesis consists of powder lineshapes in glasses.

A discussion of the origin of powder lineshapes begins with the simplified Hamiltonian of eq. (1.30). Using eq. (1.30) for an isolated center with a specific orientation with respect to the static magnetic field $\vec{H}_0$ (in the z-direction) the EPR resonance condition can be written in the form:

$$\hbar\omega = \beta \vec{H}_0 \cdot \bar{\bar{g}} \cdot \Delta\vec{S} \tag{1.80}$$

where $\bar{\bar{g}}$ is the g-tensor associated with the microscopic nature of the center and ω is the frequency of a small microwave field applied to the center. Continuous wave EPR measurements in the laboratory are usually performed under conditions of constant microwave frequency ω, with a slowly varying field H_0 used to vary the instantaneous resonance condition. For this technique, EPR occurs at the magnetic field value given by (for $\Delta S = 1$):

$$H_0 = \frac{\hbar\omega}{g_{eff}\beta} \quad , \tag{1.81}$$

where g_{eff} is the effective g-value resulting for a particular orientation of the tensor relationship of eq. (1.80). For systems with axial symmetry ($g_x = g_y = g_\perp$, $g_z = g_{||}$), g_{eff} can be written in the form:

$$g_{eff} = \frac{1}{2}\left(g_{||}^2 \cos^2\theta + g_\perp^2 \sin^2\theta\right)^{1/2} \tag{1.82}$$

where θ is the angle between $\vec{H}_0$ and the axis of symmetry.

When a sample containing a large number of centers which have random orientations with respect to the magnetic field (as in glass samples),

the resonance condition of eq. (1.81) will contain contributions from all possible orientations, and the resulting EPR lineshape will result from a combination of all possible values of g_{eff}. In order to find an expression for the EPR lineshape as a function of magnetic field, we note that the number of centers whose axis of symmetry is at an angle θ from $\vec{H}_o$ is:[31,35]

$$dN = \frac{N}{2} \sin\theta d\theta \tag{1.83}$$

But, from eqs. (1.81) and (1.82) we have:

$$dH_o = \frac{2H_o^2}{N_o A^2} (g_{\parallel}^2 - g_{\perp}^2) \cos\theta dN \tag{1.84}$$

And substituting this into eq. 1.83 yields:

$$dN = \frac{N_o}{2} \frac{A^2}{H_o^3} \frac{dH_o}{(g_{\parallel}^2 - g_{\perp}^2)} \cos\theta \quad , \tag{1.85}$$

or, after simplifying:

$$dN = \frac{N_o}{2} \frac{A^2}{H_o^3} \left[\left(g_{\parallel}^2 \cdot g_{\perp}^2 \right) \left(\frac{H_o^2}{A^2} - g_{\perp}^2 \right) \right]^{-1/2} dH_o \quad , \tag{1.86}$$

where

$$A = \frac{\hbar\omega}{\beta} \quad . \tag{1.87}$$

A plot of dN/dH from eq. (1.86) will display the EPR lineshape as a function of the magnetic field H_o. Figures (1.7) show a typical resulting lineshape for specific values of $g_{\perp}$ and $g_{\parallel}$. The infinite peaks in the figures are a consequence of the implicit assumption in this discussion of infinitely narrow spin packets for each specific value of g_{eff}.

When finite linewidths are assumed for these contributions, the divergences disappear and the resulting lineshapes can be used to model specific situations. This is also illustrated in Figs. 1.7.

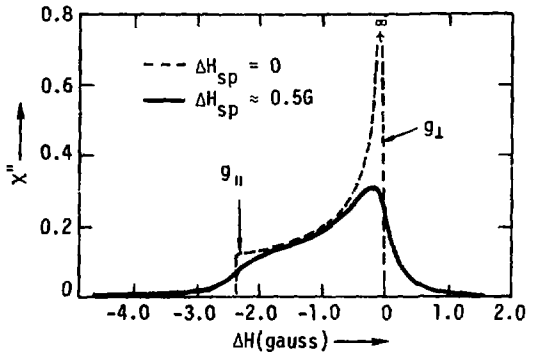

(a)

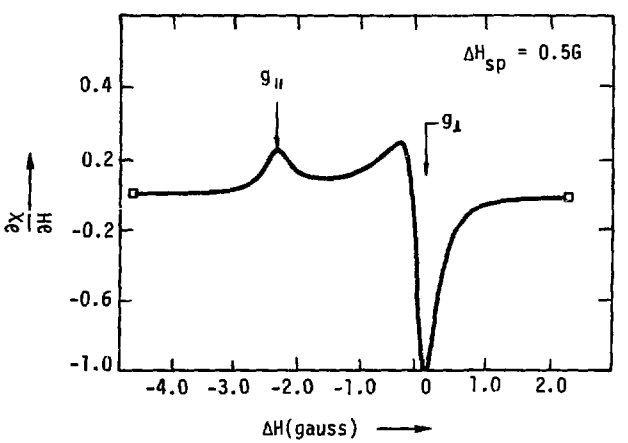

(b)

Figure 1.7 Powder Lineshapes

This figure illustrates some of the powder lineshapes that are associated with systems having axial symmetry and which can be characterized by two g-values, $g_{\parallel}$ and $g_{\perp}$. In part (a), absorption lineshapes which result from the assumption of zero and finite spin packets widths are shown. In part (b), a derivative lineshape for finite spin packet width is shown.

III. EXPERIMENTAL

A. Irradiation Facilities

1. Introduction

Three different LLL radiation sources were used for irradiation of the samples. A pool-type Co^{60} source was used for gamma-ray irradiation, the LLL Rotating Target Neutron Source (RTNS)[36] was used for 14.8 MeV neutron irradiations, and the Livermore Pool-Type Reactor (LPTR)[37] was used for irradiation by a broad spectrum of fast neutrons and gamma rays. The LPTR facility was also used for thermal neutron irradiations. For irradiations in these facilities, no special provisions were made to control the temperature of the various samples. The ambient temperatures of these sources vary from room temperature to about 60°C. The general characteristics of each of these sources are described below.

2. Cobalt-60 Source

The Livermore Co^{60} irradiation facility maintains a source with a maximum intensity of about $3 \cdot 10^3$ rad/sec. The source consists of 72 nine-inch pencils formed into a cylinder with a seven-inch diameter and is submerged under twenty feet of water.

A pneumatically activated system was used to deliver aluminum capsules which contain the samples to the center of the cobalt source. There were no facilities for controlling or monitoring the sample temperature, but the ambient temperature of the water pool was ~25°C. Exposure times for the samples ranged from twenty seconds to one month yielding a range of doses of from 10^5 to 10^{10} rads.

3. The 14 MeV Neutron Source

The LLL Rotating Target Neutron Source (RTNS)[36] was used for 14 MeV neutron irradiation of samples. The RTNS is an intense (typically $4 \cdot 10^{12}$ neutrons/sec) source which produces neutrons with an average energy of 14.8 ± 10% MeV.

The neutrons are produced by the deuterium-tritium fusion reaction. In the RTNS, a 400 MeV, 15 mA deuteron beam impinges a tritium target. The target consists of a 230 mm diameter sphere of a tritium implanted copper-zirconium alloy. During operation the target is rotated at 1100 rpm and is water-cooled on its outside surface. Samples irradiated by the RTNS received total neutron fluences ranging from 10^{10} to ~$5 \cdot 10^{16}$ n/cm^2.

4. The Livermore Pool Type Reactor (LPTR)

The LPTR is a research reactor moderated and cooled by light water in a tank-type pool and fueled with fully enriched ^{235}U fuel elements of the materials-test-reactor type. The reactor operates at a steady state power of 3 megawatts and provides a peak thermal neutron flux of $7 \cdot 10^{13}$ n/cm^{2}sec. The reactor has a number of different facilities for neutron irradiation of sample specimens.

We used two different reactor facilities for irradiation of the samples: one in-core (E-1) facility for fast neutron irradiation, and the West-thermal-column-stringer for thermal neutron irradiation. Because of the complex neutron and gamma spectrum associated with the reactor, it is difficult to precisely specify the radiation field for these irradiations.

The in-core facility can be characterized by a cadmium ratio[37] of 2.5, a thermal neutron flux of $1 \cdot 9 \cdot 10^{13}$ n/cm^{2}sec and a fast (E > 0.1 MeV) neutron flux of $1 \cdot 2 \cdot 10^{13}$ n/cm^{2}sec. The thermal column facility is characterized by a range of thermal neutron fluxes and associated cadmium ratios of from 10^{11} n/cm^{2}sec and 10^3 to a thermal neutron flux of 10^{12} n/cm^2 and a cadmium ratio of 2.0.

In addition, there exist very intense gamma ray fluxes throughout the reactor facility. The gamma ray spectrum is very broad with a peak at about 0.7 MeV. During operation, the in-core (E - 1) irradiation facility has a gamma flux of about $1.7 \cdot 10^6$ rad/hr, while the thermal column has a gamma flux of about $3 \cdot 10^5$ rad/hr.

Samples irradiated in the reactor core received integrated fast neutron (E_n > 0.1 MeV) fluences ranging from $2.2 \cdot 10^{15}$ n/cm^2 to $1.4 \cdot 10^{18}$ n/cm^2. The gamma ray doses received for these exposures ranged approximately from $5 \cdot 10^6$ rads to $5 \cdot 10^{10}$ rads. No special provisions were made for temperature control of the samples, but the capsules containing the samples were in contact with the reactor pool water which has an ambient temperature of about 40°C.

Samples irradiated in the West-thermal-column-stringer received total thermal neutron fluences ranging from $2 \cdot 10^{11}$ n/cm^2 to $1 \cdot 10^{17}$ n/cm^2, with an accompanying range of cadmium ratios of from 10^3 to 20, respectively. The gamma ray doses associated with these exposures ranged from about $2 \cdot 10^5$ rads to 10^8 rads. There were no special provisions made for temperature control of the samples, but the ambient temperature of the facility ranges from 25°C to 70°C during reactor operation.

B. Sample Materials

Four different materials were used for the radiation damage studies. The materials included two ultra-pure fused silicas, quartz crystal and BK7[38] optical glass.

The first ultra-pure fused silica is known as Suprasil 1.[39] Suprasil 1 is synthetic silica which is produced by the hydrolyzation of $SiCl_4$ in an oxygen-hydrogen flame. This material is practically free (< 1 ppm) of metallic impurities; but has a relatively high OH content (~ 1000 ppm) and also contains about 100 ppm Cl impurity.

The second fused silica is known as Suprasil W1.[39] Suprasil W1 is a synthetic silica produced from $SiCl_4$ in a water vapor-free plasma flame. This silica is similar to Suprasil 1; but contains only 0.4 ppm OH and about 200 ppm Cl impurities.

The crystalline sample was a piece of α-quartz crystal. The sample was cut from an optical polarization rotator. An emission spectroscopy

analysis indicated the presence of metallic impurities in the levels 100 ppm (Mg), 10 ppm (Al, Fe), 1 ppm (Cu) and ~ 1 ppm (Ag, Ca).

The fourth sample material was BK7 optical glass. Since the composition of BK7 is proprietary information, it was necessary to perform an emission spectral analysis in order to determine the composition of our sample. The base composition was found to be (in weight percent): SiO_2 (75%), Na_2O (10%), K_2O (5%), B_2O_3 (5%) and BaO (0.5%). A large number of metallic oxides were also detected in the glass with concentrations ranging from 0.3% to 0.0003%.

C. EPR Spectrometer

1. Introduction

The EPR spectrometer used for our experiments was a conventional superheterodyne type system operating with a microwave frequency of about 9.5 Ghz and an intermediate detection frequency of 30 Mhz. Phase-locked signal detection was used to provide data output in the form of lineshape derivatives. The microwave frequency was always "locked" to the instantaneous microwave resonant frequency of the sample cavity so that all measurements were performed in the pure absorption mode. The configuration of the spectrometer was largely determined by the nature of the samples which were investigated. In particular, the relatively long relaxation times associated with the E' defect center in fused silica necessitated the use of low frequency signal detection and low microwave power operation of the spectrometer.

The three sample characteristics measured by the spectrometer were EPR lineshapes, absolute spin measurements, and power saturation behavior. The EPR lineshapes were recorded in a conventional manner with very conservative experimental parameters. The absolute spin measurements and power saturation behavior were performed with the use of ratio measurement techniques in order to avoid errors associated with absolute calibration of the spectrometer.

The remainder of this section consists of a brief discussion of the spectrometer construction and operation. There is also included a detailed analysis of the first derivative signal detection technique used for these experiments. This discussion assumes considerable familiarity with EPR systems; for a more detailed presentation of these considerations, Poole[31] and Alger[32] are excellent references.

2. Spectrometer Construction

A schematic diagram of the spectrometer system is presented in Fig. 1.8. The basic design is that of a conventional superheterodyne system used to detect $\chi''(\omega)$, the imaginary portion of the magnetic susceptibility. The system was constructed in a superheterodyne configuration because the noise characteristics of superheterodyne receivers are independent of the signal detection frequency. This characteristic is particularly valuable for detection of low frequency (less than 100 hz) signals. Receivers based on crystal rectification of microwave carrier waves are undesirable for low frequency signal detection because the noise figure of these systems increases with the inverse of the signal frequency. Superheterodyne receivers are also very convenient for low power (less than 1 μW) signal detection because of the ease with which the detector gain may be varied.

The main microwave source was a Varian #153C low noise X-band klystron which delivers a peak power of about 250 mW. The klystron was powered by a Hewlett-Packard model 716B klystron power supply. The klystron frequency was controlled by a homemade automatic frequency control (AFC) which employed a 61 kHz frequency modulation of the klystron output to "lock" the klystron to the instantaneous EPR cavity resonant frequency. The local oscillator microwave source was a Laboratory for Electronics Ultra-Stable microwave source (stable to about 1 khz).

The spectrometer magnet was a 12" Varian EPR magnet (model #4012). The EPR cavity was a Varian V232 dual sample cavity with a TE_{104} mode, a

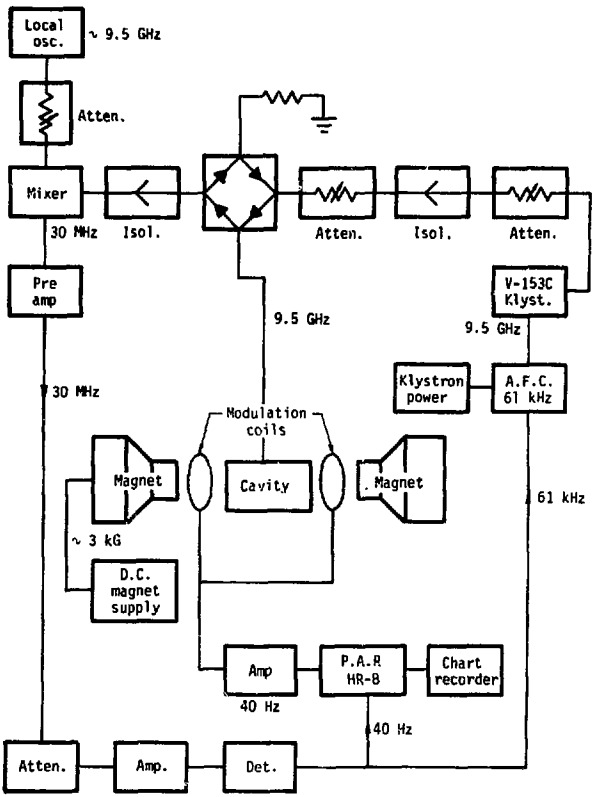

Figure 1.8 Superheterodyne Spectrometer Schematic

This figure schematically describes the arrangement of the various components of the superheterodyne spectrometer used for the present experiments.

Q factor of about 7500 and a resonant frequency of about 9.5 GHz. A Microline model 730 variable attenuator and a Hewlett-Packard precision attenuator model 382A-X were used to attenuate the input microwave power to the cavity by as much as 80 decibels (dB). The microwave detector was a Microwave Associates model MA-54071 hybrid magic tee with matched IN23 diodes and a preamplifier with 30 dB gain (model #MA-7210-10).

A schematic diagram of the 30 MHz detector is shown in Fig. 1.9. The detector consists of a series LC resonant network with Q ≈ 10. The output of the LC circuit is rectified by a single diode and is then filtered by a standard RC low-pass filter. The output of this detector is used both for the EPR signals and the 61 kHz klystron frequency control signal. The phase-locked amplifier used for the EPR signal detection was a Princeton Applied Research model HR-8 lock-in amplifier.

The Klystron output power was measured with a Hewlett-Packard model 432A power meter, while the microwave frequency was measured with a Hewlett-Packard model 5245L counter. The D.C. magnetic field was periodically monitored with a Systron-Donner Digital NMR Gaussmeter model #3193.

3. Spectrometer Performance

The spectrometer performance capabilities were generally equal to or better than those required by the experiments. The spectral resolution (better than 15mG) was much better than required, because the narrowest lines which were of experimental interest had linewidths of about 0.5 gauss. For power saturation measurements, the capability to operate the spectrometer with as little as 2 nanowatts ($2 \cdot 10^{-9}$W) incident on the cavity allowed data to be recorded over an extremely wide power range without altering the spectrometer configuration. During the experiments, the nature of our EPR samples prevented the use of the spectrometer in its optimum sensitivity configuration, so that the resulting useable sensitivity was about $5 \cdot 10^{13}$ spins/gauss. The spin sensitivity was the only spectrometer

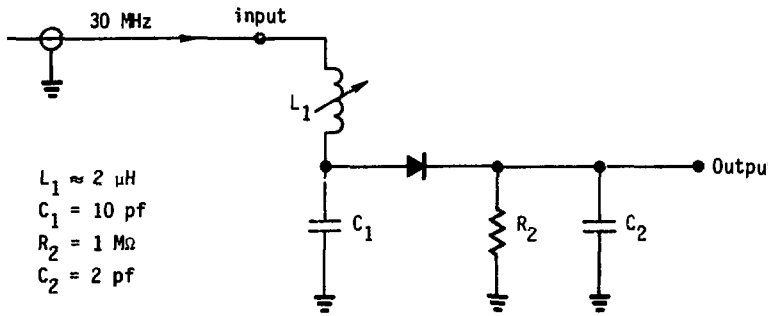

Figure 1.9 30 Mhz Detector

This figure is a schematic diagram of the detector used for the 30 Mhz mixer signal.

characteristic which limited the experimental capabilities for our particular measurements.

There were a variety of noise sources which imposed occasional limitations on the spectrometer performance. Microphonics in the system were always the ultimate limiting noise source. During operation at very low klystron power the frequency stability (usually stable to better than 1 kHz) sometimes degraded to the point that a noticeable increase in the system noise figure was observed. There was also an intermittent problem with the magnetic field stability because A.C. power line voltage fluctuations were sometimes capable of causing magnetic field shifts as large as 0.5G. These problems did not impose fundamental limitations on the spectrometer performance, but were merely situations which had to be dealt with occasionally.

4. Spectrometer Operation

The spectrometer (schematically diagrammed in Fig. 1.8) operated in a fairly conventional manner. The AFC "locked" the EPR Klystron to the cavity resonance. Microwave power reflected from the sample cavity was then mixed with a local oscillator to produce an intermediate frequency of 30 MHz. Finally, the 30 MHz signal was rectified to yield both the EPR signal and the 61 kHz frequency control signal. EPR signals were recorded at low frequency (≈40 hz) in a first-derivative form using phase-locked detection.

In all cases, during measurement of the EPR spectral lineshapes, the magnetic field modulation amplitude was at least ten times smaller than the width of the spectra being observed. In addition, the modulation frequency and magnetic field sweep rate were reduced to values where they could have no measurable effect on the measured lineshapes.

Varian standard pitch samples were used to calibrate some spectrometer signals. A "weak pitch" sample was used to establish the overall system

sensitivity. For absolute spin measurements, a Varian "strong pitch" sample (accurate to ± 10%) was used to calibrate signal amplitudes.

Absolute spin measurements were performed in a slightly unconventional manner. In order to avoid errors due to changes in the spectrometer gain, all signal amplitudes were compared to the signal of a "dummy" sample in the second cavity of the dual sample cavity. The "dummy" sample was a small piece of DPPH. Since the signal of the unknown sample and the "dummy" sample occurred at roughly the same magnetic field values and were recorded at the same modulation frequency, it was necessary to employ a small pair of D.C. magnetic field offset coils on the "dummy" cavity to separate the two signals (see Fig. 1.10).

The procedure for performing the absolute spin measurements was as follows. First, a spectra was recorded which compared the Varian strong pitch signal and the "dummy" DPPH signal. Then, without changing the relative amplitude of modulation fields for the two cavities, the signal from an unknown sample was compared to the "dummy" signal. The resulting four first-derivative spectra were then numerically doubly integrated to yield effective "spin" measurements. The ratio of the number of spins in the strong pitch to the "dummy" sample was called R_1. The ratio of spins in the unknown sample to the "dummy" was called R_2. The number of spins in the unknown sample N_u could then be shown to be related to the number of spins in the strong pitch N_{sp} sample by:

$$N_u = N_{sp} \left(\frac{R_2}{R_1} \right) \quad . \tag{1.88}$$

There were a number of correction factors not shown in eq. (1.88) which were included to account for the effects of parameters such as sample sizes. The result of eq. (1.88) is useful because it is independent both of any absolute spectrometer calibration and the size of the "dummy" sample. Thus the results depended only on the number of spins in the unknown sample

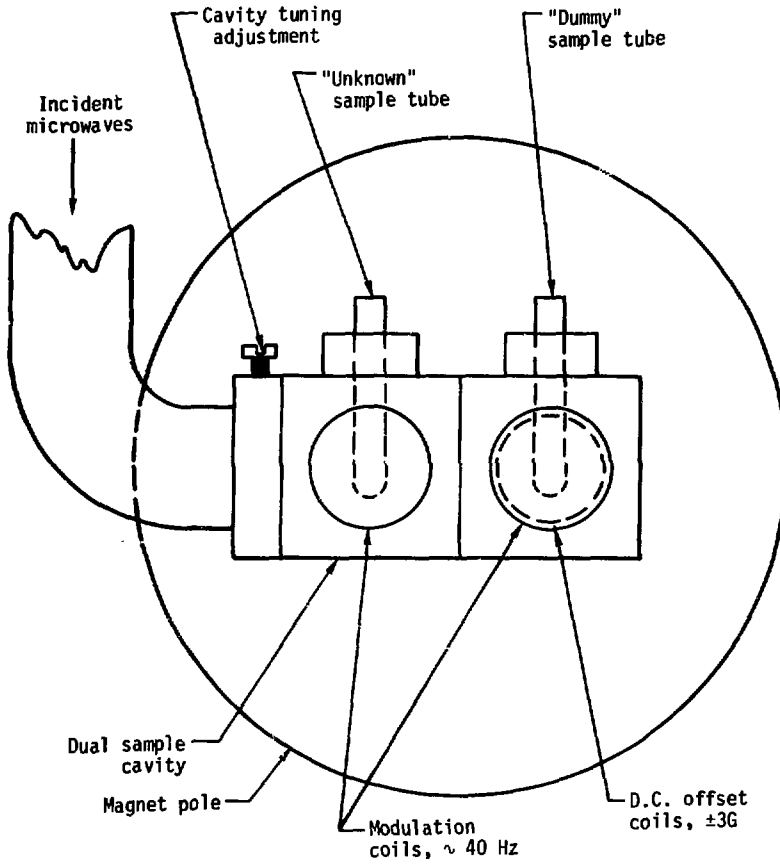

Figure 1.10 Sample Cavity Arrangement

This figure illustrates the physical arrangement of the dual EPR sample cavity. The sample tube centered in the D. C. offset coils is used to supply a calibrated signal for absolute measurements. The other sample tube is used for the specimen which is being investigated.

and the calibration of the strong pitch sample, assuming that the samples caused no significant changes in the microwave mode pattern.

In a manner similar to the spin measurements, the "dummy" sample was used to calibrate power saturation measurements. Since the DPPH paramagnetic spins have relaxation times short enough that we were unable to saturate the DPPH signal with the available klystron power (~ 250 mW), a plot of the DPPH signal versus applied power results in an ideal unsaturated signal versus power curve. Comparison of the saturation of unknown sample signal amplitudes (which could be saturated) to the "dummy" signals yielded excellent power saturation data for the unknown samples.

5. Theory of Spectrometer Operation

EPR measurements on systems such as the E' center which are characterized by long relaxation times require a precise understanding of the operation of the spectrometer. Our first attempts to record E' spectra were characterized by nonreproducible results, unexpected signals and unexplainable behavior. These problems were due to a combination of characteristics of the spectrometer and of the E' center, and a failure to account for them during the experiment. The following analysis of signal detection in a superheterodyne spectrometer is useful because it clearly identifies the origin of the different signals which are available.

The detected signals are due to microwave power reflected from the EPR cavity. The microwave field $H_1(t)$ incident on the cavity can be written

$$H_1(t) = H_1[\sin\omega t - i \cos \omega t] \tag{1.89}$$

and has a vector direction perpendicular to the static magnetic field $\vec{H}_0$. The microwave field reflected from the cavity depends on the resonant properties of the cavity and the EPR sample. The behavior of the cavity and sample can be represented by a complex function $\chi_c(\omega, H_0)$:

$$\chi_c(\omega,H_0) = \chi_c'(\omega,H_0) + i\chi_c''(\omega,H_0) \tag{1.90}$$

The microwave field reflected by the cavity, $H_R(t)$, will be proportional to $\chi_c(\omega,H_0)$, and its real part will have the form:

$$H_R(t) \propto H_1[\chi_c'(\omega,H_0)\sin \omega t + \chi_c''(\omega,H_0) \cos \omega t] \tag{1.91}$$

The reflected wave $H_R(t)$ acts as a carrier wave for the different spectrometer signals.

There are a number of techniques which can be used to detect the signals carried by $H_R(t)$. Rectification of the microwaves can be accomplished by direct crystal rectification or by homodyne detection. But these methods have a disadvantage because the detected signals will have a 1/f noise characteristic, making low frequency signal detection difficult.

The more complicated superheterodyne detection technique is often used because it avoids the 1/f noise characteristic. In this method, the microwave $H_R(t)$ is mixed with a local oscillator signal $H_\ell(t)$ at a nearby frequency ω_ℓ:

$$H_\ell(t) = L \sin \omega_\ell t \tag{1.92}$$

When the signal $H_R(t)$ is "mixed" with $H_\ell(t)$, the mixer produces a voltage $V_R(t)$ at the intermediate frequency ω_2:

$$V_R(t) \propto H_1 L[\chi'(\omega,H_0) \sin \omega_2 t + \chi''(\omega,H_0) \cos \omega_2 t] + \text{smaller terms}, \tag{1.93}$$

where:

$$\omega_2 = |\omega - \omega_\ell| \quad . \tag{1.94}$$

ω_2 (usually about 30-100MHz) can be adjusted by varying the local oscillator frequency. The intermediate radio frequencies used for superheterodyne detection are convenient because they can be directly detected by crystal rectification without acquiring the 1/f noise spectrum which would have been acquired if the microwave frequencies had been directly detected by crystal rectification. Thus, the superheterodyne system allows the maximum

possible signal to noise ratio possible for low frequency signal detection. When the signal voltage $V_R(t)$ is demodulated, the final signal V_s will have the form:

$$V_s \propto H_1 L[\chi_c'(\omega,H_0) + \chi_c''(\omega,H_0)] + \text{smaller terms} \qquad (1.95)$$

The χ' term represents the in-phase portion of the reflected microwaves and describes frequency dependent or dispersive behavior. The χ'' term represents the out-of-phase portion of the reflected microwaves and describes power absorption (or emission) in the sample cavity.

For pure absorption measurements of EPR spectra, the microwave frequency ω is adjusted to equal the cavity resonant frequency. When this is the case, $\chi_c'(\omega,H_0)$ is zero and all detected signals are proportional to $\chi_c''(\omega,H_0)$. However, if the microwave frequency is not adjusted to equal the cavity frequency, the detected signals will be of the form of eq. (1.95) and will be difficult to interpret due to the admixture of $\chi_c'(\omega)$ and $\chi_c''(\omega)$.

Experimentally, both the microwave frequency and the static magnetic field are modulated to provide detectable signals which ride on the microwave carrier. Frequency modulation of the klystron yields a signal which can be used to control the microwave frequency. Modulation of the static magnetic field produces an EPR signal at the modulation frequency. Since we are concerned with pure absorption measurements, we will look at the behavior of $\chi_c''(\omega,H_0)$ in response to these modulations.

$\chi_c''(\omega,H_0)$ can be expanded about ω_0 (cavity resonant frequency) and H_0 (static component of magnetic field) in a Taylor series:

$$\chi_c''(\omega,H) = \chi_c''(\omega_0,H_0) + \frac{\partial\chi_c''}{\partial H}(H - H_0) + \frac{1}{2}\frac{\partial^2\chi_c''}{\partial H^2}(H - H_0)^2 + \ldots$$
$$+ \frac{\partial^2\chi_c''}{\partial\omega\partial H}(H - H_0)(\omega - \omega_0) + \frac{\partial\chi_c''}{\partial\omega}(\omega - \omega_0)$$
$$+ \frac{1}{2}\frac{\partial^2\chi_c''}{\partial H^2}(H - H_0)^2 + \ldots \qquad (1.96)$$

When the magnetic field modulation is included with the magnetic field:

$$H(t) = H_o + H_m \cos \omega_m t \quad , \tag{1.97}$$

and the microwave frequency is similarly written:

$$\omega(t) = \omega_o + A_c \cos \omega_c t \quad , \tag{1.98}$$

substitution into the Taylor series above yields:

$$\chi_c''(\omega,H,t) = \chi_c''(\omega_o,H_o) + \frac{H_m^2}{2}\frac{\partial^2\chi_c''}{\partial H^2} + \frac{A_c^2}{2}\frac{\partial^2\chi_c''}{\partial\omega^2} \qquad \text{(a)}$$

$$+ \frac{\partial\chi_c''}{\partial H} H_m \cos\omega_m t + \text{smaller terms} \qquad \text{(b)}$$

$$+ \frac{\partial\chi_c''}{\partial\omega} A_c \cos\omega_c t + \ldots \qquad \text{(c)}$$

$$+ \frac{1}{2}\frac{\partial^2\chi_c}{\partial H^2} H_m^2 \cos(2\omega t) + \ldots \qquad \text{(d)}$$

$$+ \frac{1}{2}\frac{\partial^2\chi_c}{\partial\omega^2} A_c^2 \cos(2\omega_c t) + \ldots \qquad \text{(e)}$$

$$+ \text{higher order terms.} \tag{1.99}$$

Since the detected signal $V_s(t)$ is proportional to $\chi_c(\omega,H,t)$, the various terms in this expansion represent the different signals which can be detected. Terms (a), (b) and (c) represent the three most important signals for phase-locked detection of first-derivative EPR spectra in the "pure-absorption" mode.

Term (a) represents the level of continuous microwave power absorption in the EPR cavity and sample. Term (a) leads to a carrier wave amplitude level at the intermediate frequency (here, the "i.f." = 30 Mhz) and a constant D.C. bias voltage at the 30 Mhz detector output.

Term (b) represents the first derivative of χ_c'' with respect to magnetic field. Since the EPR cavity properties have effectively no dependence on the magnetic field, term (b) is related directly to the EPR characteristics

of the sample contained by the cavity. When

$$H_m < 0.1\ \Delta H_{1/2} \tag{1.100}$$

where $\Delta H_{1/2}$ is the EPR resonance linewidth, term (b) is effectively the derivative of the EPR magnetic field lineshape of the sample. There are several restrictions on the choice of H_m and ω_m for measuring the EPR spectrum of a particular sample. In order to satisfy the adiabaticity assumptions associated with the slow passage solutions of the Bloch equations (see eq. (1.47)), it is necessary that

$$\omega_m H_m < \gamma H_1^2 \tag{1.101}$$

This is not normally a severe restriction, but it can be a significant limitation for low microwave power detection. In addition, if the modulation magnetic field $\vec{H}_m$ changes quickly with respect to the relaxation times of the relevant EPR system, the resulting EPR spectra will be altered by "passage effects." In order to avoid these problems, it is necessary to satisfy:

$$\omega_m < \frac{1}{T_2} \tag{1.102}$$

For our experiments this required that ω_m be less than 1 khz.[40]

Term (c) is determined by the frequency dependence of the cavity-sample combination and results in the signal used to control the EPR klystron frequency. When the klystron frequency is adjusted so that term (c) is zero, χ_c' is zero and the associated EPR measurements will be in the pure "absorption-mode." In addition, since ω_c was about 61 khz, the amplitude A_c must be restricted to prevent the possibility of "passage effects" between spin packets in certain EPR systems. For our samples, this required that

$$A_c < 1 \text{ khz} \quad , \tag{1.103}$$

and was satisfied by our experimental parameters.

The additional terms in eq. (1.99) represent higher orders of the Taylor's series expansion. Term (d) is often used for second-derivative

recording of EPR spectra. For our experiments, it was not necessary to use any of these higher order terms.

IV. EXPERIMENTAL RESULTS

A. Introduction

The experimental data consists of the EPR spectra observed in the silicate glasses and quartz crystal as a result of exposure to Co^{60} γ-rays, 14 MeV neutrons, and the reactor core and thermal column neutron plus gamma ray ($n + \gamma$) fluxes. We are concerned mainly with three different aspects of the EPR spectra: the EPR lineshapes, absolute spin measurements determined from the lines, and the power saturation behavior of the lines. These three aspects were chosen because they are relatively simple to execute and because the resulting information can be used in a number of ways.

The EPR spectra were recorded in a first derivative form in the laboratory. For lineshape considerations and power saturation measurements, the derivative lineshapes were used directly. For the absolute spin measurements, the derivative lineshapes were double-integrated in order to count numbers of spins.

The spectral resolution of the system was such that lineshape features as small as 40 mG would be easily resolved for some crystalline samples. However, significant fluctuations of the main power line voltages sometimes caused fluctuations in the magnetic field as large as 500 mG, so that the spectral resolution depended on the instantaneous power line stability.

The absolute spin standard for the spin measurements was a Varian strong pitch-sample (accurate to ±10%). As mentioned above, for absolute spin measurements the derivative lines were double-integrated. Because of the difficulty of determining the zero signal level, there is considerable error in the double integration of the lineshapes. Because of the errors accompaying integration of the spectra, our absolute spin density results are only accurate to within a factor of two. However, for a given material and type of radiation, the relative spin density measurements should be accurate

to within ±15% as long as the lineshape does not depend on the amount of irradiation. This is because relative spin densities can be determined simply from a comparison of derivative EPR signal heights for systems with the same lineshape, and no lineshape integration is necessary.

Power saturation curves were generally recorded over a range of 20-70 decibels attenuation of the incident microwave power. This wide range of applied power required corresponding changes in the gain of the EPR system. As a result, the relative accuracy of the signal amplitudes for saturation measurements is only good to about ±10%.

The absolute microwave magnetic fields in the EPR cavity were determined from calculations of the relevant microwave mode patterns. The calculations ignored the effects of slightly detuning the cavity and the effects of inserting our samples. For these reasons, the absolute H_1's cited in our results are accurate to only ±20%; but the relative values for the saturation measurements should still be accurate to within ±5%.

Prior to irradiation, no EPR spectra were detected in the glasses used in our experiments. The Suprasil glasses are low in impurity content and no signals were expected. Bk7 glass contains significant levels of paramagnetic impurities; but for the spectrometer configuration used, no signals were detected prior to irradiation.

After irradiation, all of the samples exhibited EPR signals. The characteristics of the spectra depended on the specific glass and the type and amount of radiation used. The data is presented below individually for each material that was studied.

B. Suprasil I

1. EPR Spectra

The EPR spectrum of damage centers induced in Suprasil I by Co^{60} γ-rays is shown in Fig. 1.11. For the gamma fluxes employed (10^6 - 10^{10} rads), this lineshape is independent of exposure. The spectrum

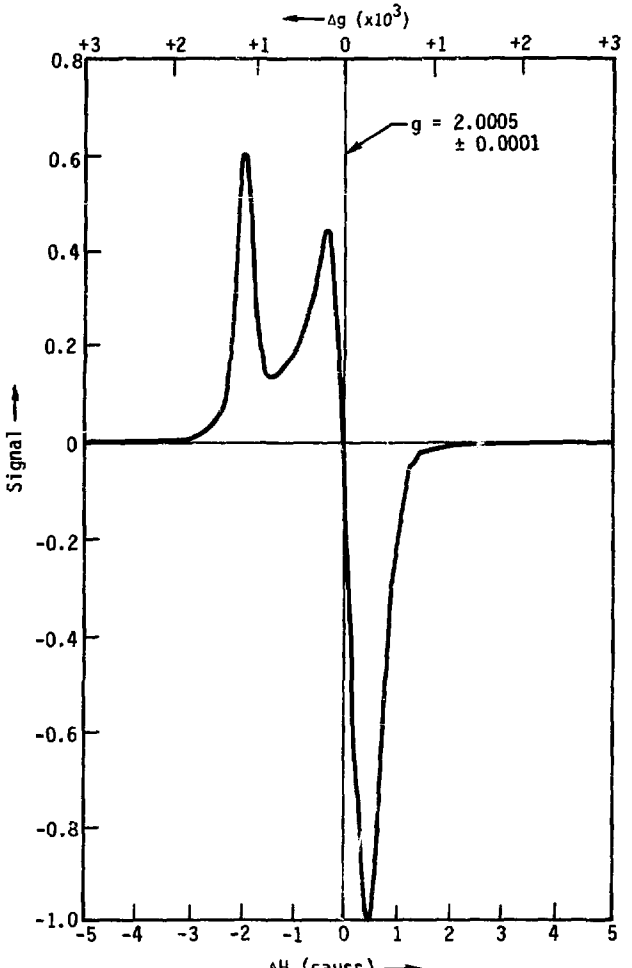

Figure 1.11 E' Spectrum of Co^{60} γ-ray Irradiated Suprasil I

This figure shows the EPR spectrum observed in γ-ray irradiated Suprasil 1 samples. This spectrum, and most of the others to follow, is a computer reproduction of a digitized version of the data. Some of the noise and minor fluctuations in the spectra are due to the method used to reproduce the data.

has a total width of about 2.5 gauss. The zero crossing g-value is $g = 2.0005 \pm 0.0001$, and the changes in g-value at the high and low magnetic field peaks of the spectrum are $\Delta g^{+} = -0.0002$, $\Delta g^{-} = +0.0012$, respectively. A similar lineshape has been previously observed in a number of different glasses and has been called the E' lineshape.

Figure 1.12 shows the Suprasil I EPR line resulting from exposure to 14 MeV neutrons. The line is basically the same as the previous E' lineshape except for a slight additional bump at $g = 2.0020$ on the low field portion of the line. Once again, the lineshape was found to be independent of the total neutron flux.

Exposure of Suprasil I to low ($<10^{17}$) neutron fluences in the reactor core resulted in spectra similar to those shown above. Exposure to the thermal column ($n + \gamma$) flux resulted in relatively low spin densities and the expected E' lineshape of Fig. 1.11. However, samples heavily irradiated in the reactor core displayed a different spectrum. A sample exposed to $1.4 \cdot 10^{18}$ neutrons/cm^2 displayed the spectrum in Fig. 1.13. The g-values of the features of this spectrum are the ones expected for E' centers, but the lineshape is considerably broadened.

2. Spin Density Measurements

Absolute measurements of damage induced spin densities were performed as a function of the amount of exposure to each type of radiation. Because of the convenience of the sources, the data for Co^{60} and 14 MeV neutron irradiations are much more detailed than the data from the reactor and thermal column irradiations.

Figure 1.14 shows the results of spin density measurements for Suprasil I exposed to Co^{60} γ-rays. Up to an exposure of 10^8 rads, the spin density increases roughly linearly with the applied radiation. But at exposures above 10^8 rads, the density begins to fall off, peaking at 10^9 rads and actually decreasing for higher exposures.

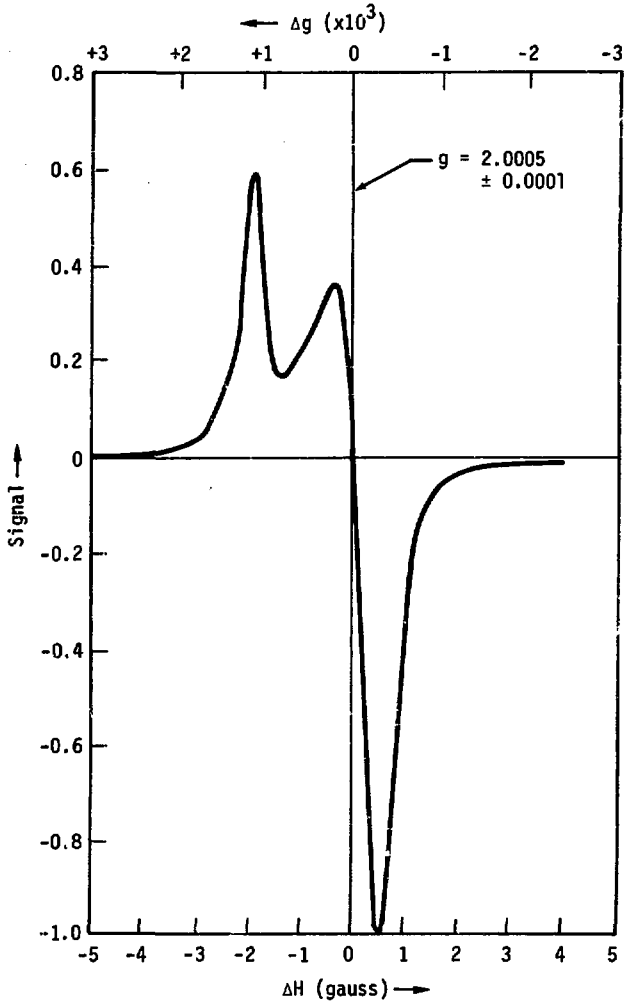

Figure 1.12 E' Spectrum of 14.8 MeV Neutron Irradiated Suprasil 1

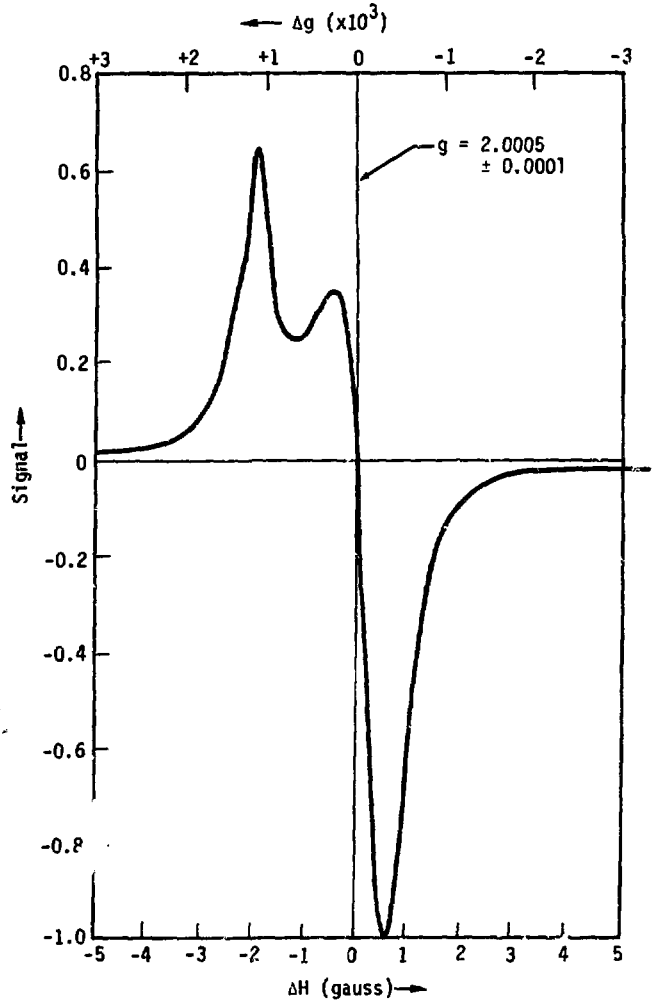

Figure 1.13 E' Spectrum of Reactor Core Irradiated Suprasil 1

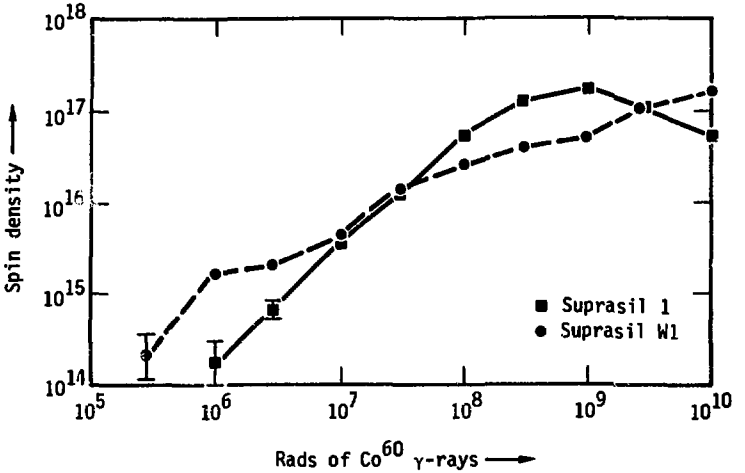

Figure 1.14 Spin Density in Co^{60} γ-ray Irradiated Suprasil Samples

This figure shows the dose-dependent spin densities measured in Suprasil 1 and Suprasil W1 samples exposed to Co^{60} γ-rays. The absolute accuracy of the measurements are probably only good to a factor of two, but the relative accuracy for comparing different samples is generally about ±10%. Error bars will be shown on these plots only when the relative error is expected to be greater than ±10%.

Figure 1.15 shows the measured spin densities resulting from exposure of Suprasil I to 14 MeV neutrons. The spin density is not a simple function of the neutron fluence; and in particular, there appears to be a "jump" of an order of magnitude in the spin density at an exposure of about $1.5 \cdot 10^{15}$ neutrons/cm^2. This behavior was verified for four or five different sets of samples. For fluences above and below $1.5 \cdot 10^{15}$ n/cm^2, the spin density appears to vary smoothly with exposure.

The spin densities measured for Suprasil I exposure to the reactor core (n + γ) fluxes is shown in Fig. 1.16. The figure also shows the results for exposure to the thermal column (n + γ) flux. In both cases the spin density appears to be linearly related to the exposure. Under exposure to the reactor core, relatively high spin densities ($\sim 3.6 \cdot 10^{18}$/cm^3) were measured with no evidence of "saturation" of the spin density as a function of radiation dose.

3. EPR Saturation Behavior

With one major exception, the power saturation behavior of the E' center in Suprasil I was very similar for most of the irradiations included in the experiments. The extremely low microwave powers which are capable of saturating the E' center resonance have been well established.[40] Figure 1.17 shows a typical saturation curve for the E' center. Here, the relative amplitude of $\chi''(\omega)$ is plotted as a function of H_1. For most samples, these measurements demonstrated that a microwave power of about 2.5 μW (or $H_1 \approx$ 3mG) was sufficient to saturate the amplitude which would be expected for an unsaturated $\chi''(\omega)$.

For most situations, the E' lineshape was independent of the microwave power used to measure the spectra. However, under conditions of extreme saturation ($S > 10^3$) it was possible to saturation broaden individual spin packets of the system until they were as broad as the entire inhomogeneous lineshape. This situation corresponds to the conditions defined in eq. (1.71),

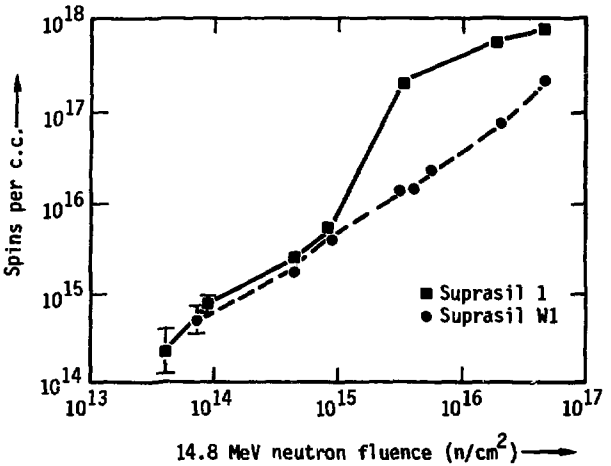

Figure 1.15 Spin Densities in 14.8 MeV Neutron Irradiated Suprasil Samples

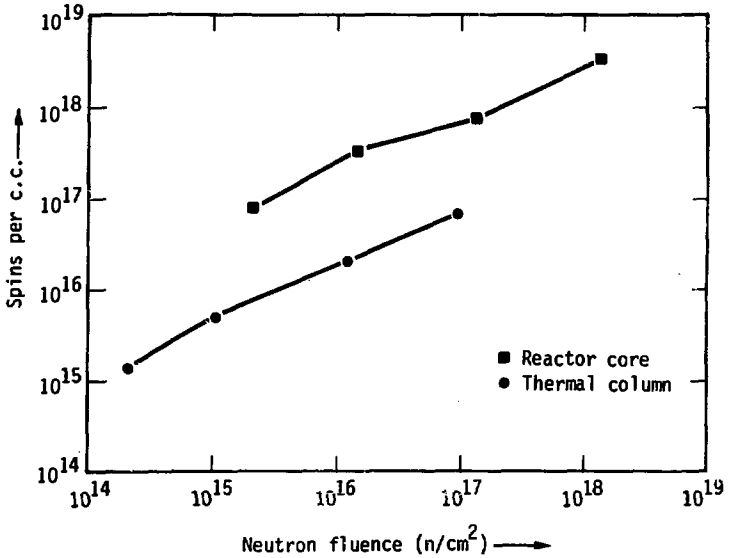

Figure 1.16 Spin Densities in Reactor Irradiated Suprasil 1

Here, for reactor core irradiations, the neutron fluence is the integrated fluence of only those neutrons with energies greater than 0.1 MeV. For thermal column irradiations, the neutron fluence is the total neutron fluence experienced by the samples.

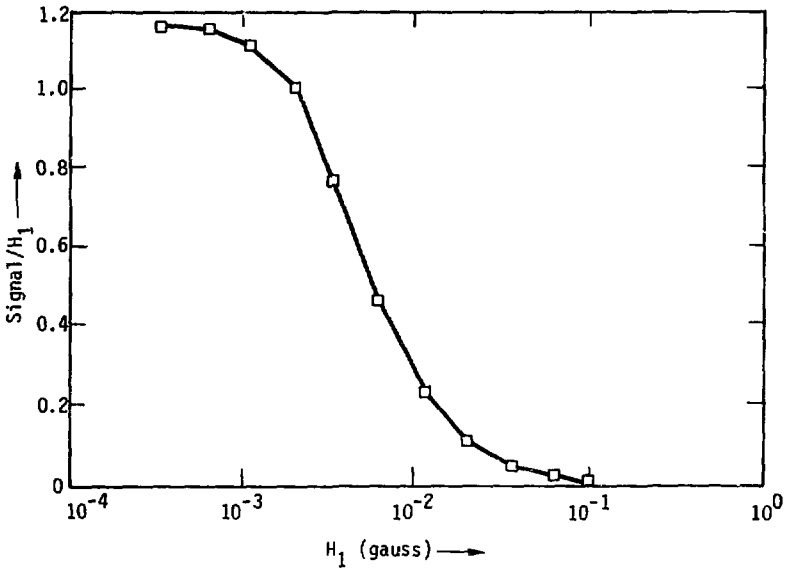

Figure 1.17 Power Saturation of $\chi''(\omega)$ for the E' Center

Here, the relative amplitude of $\chi''(\omega)$ is plotted as a function of the applied microwave field amplitude H_1.

where

$$\frac{\sqrt{1+S}}{T_2} \geq \frac{1}{T_2^*} \quad . \tag{1.71}$$

Experimentally, this situation was observed as a qualitative broadening of the E' lineshape spectral features. Fig. 1.18 shows the saturation broadened spectra obtained for the same sample used to obtain the data for Fig. 1.17.

Using different types of irradiations usually had little effect on the saturation behavior. For Co^{60} irradiations, only very slight changes in the saturation behavior could be detected. The same was true for thermal column exposures. For 14 MeV neutron irradiations, some of the more intensely irradiated samples required slightly higher (factors of 1.5-2) powers to saturate the signal.

The major exception noted above is the saturation behavior of Suprasil I exposed to high neutron fluences in the reactor core. The sample which was exposed to $1.4 \cdot 10^{18}$ n/cm^2 in the reactor core required about two orders of magnitude more power to saturate the signal than for the sample in Fig. 1.17.

C. Suprasil W1

1. EPR Spectra

There were a number of surprising differences in the E' spectra in Suprasil W1 sample, compared to the Suprasil I samples. The spectrum of Suprasil W1 irradiated by Co^{60} γ-rays is shown in Fig. 1.19. This spectrum is similar to the E' spectrum in Fig. 1.11, except for the presence of a slight peak of $g = 2.0020$. For Co^{60} irradiations, the lineshapes were independent of dose for the range of doses used (10^6 - 10^{10} rads).

When exposed to 14 MeV neutrons, Suprasil W1 exhibited the EPR lineshape shown in Fig 1.20. This lineshape has two peaks of nearly equal intensity at g values of 2.0017 and 2.0020. The remainder of the spectrum

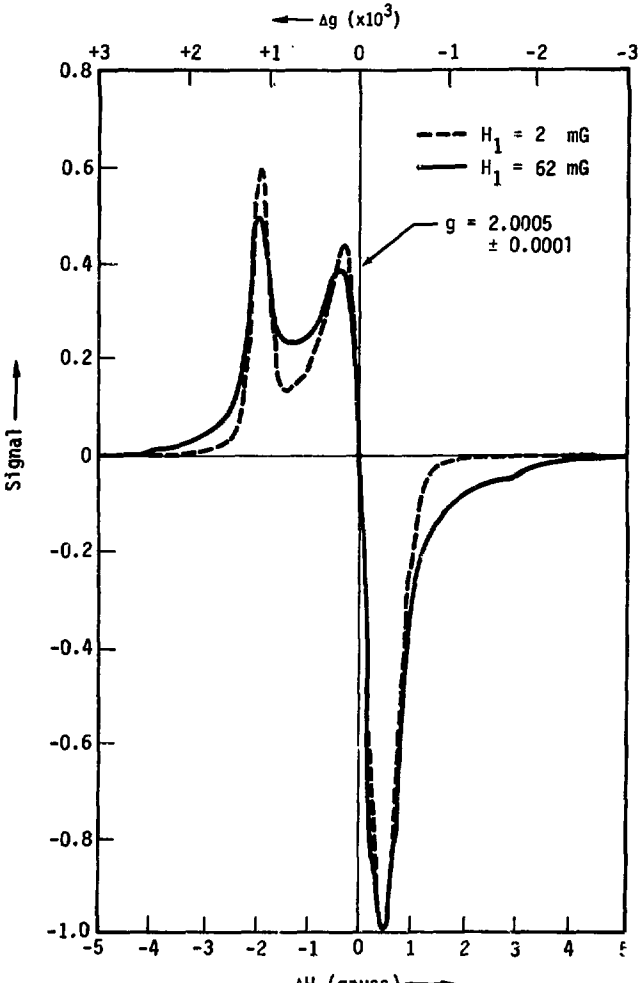

Figure 1.18 Saturation Broadened E' Spectra

This figure shows the changes which occur in the E' lineshape as saturation broadening occurs. The dotted line shows the normal unsaturated lineshape. The solid line, which was recorded with increased gain for convenient comparison of the spectra, shows the saturated lineshape recorded with H_1 =62 mG.

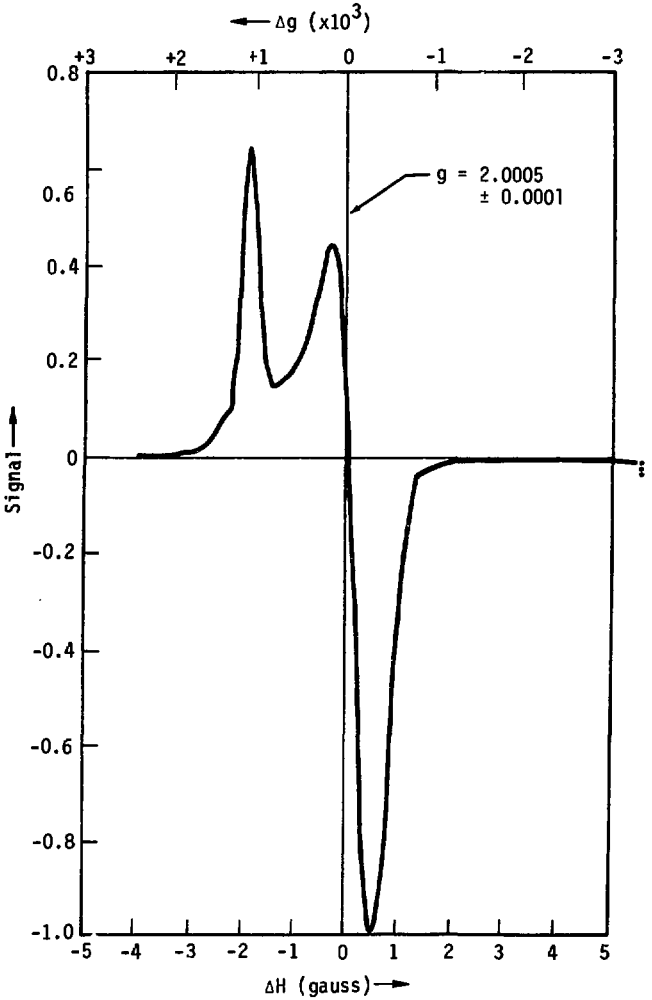

Figure 1.19 E' Spectrum of Co^{60} γ-ray Irradiated Suprasil W1

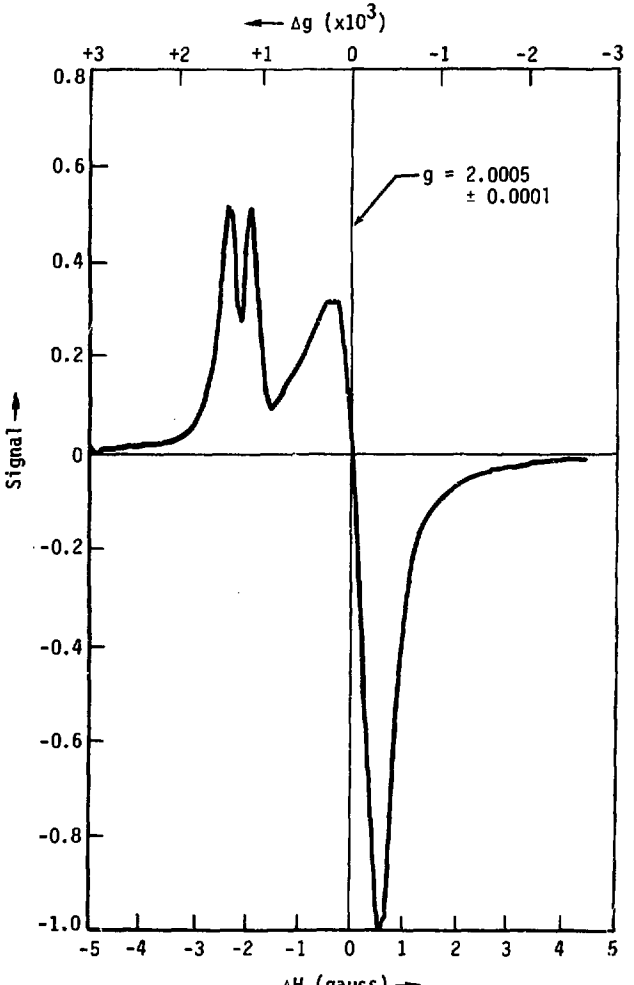

Figure 1.20 E' Spectrum of 14.8 MeV Neutron Irradiated Suprasil W1

is similar to the other E' lineshapes shown above. As with previous samples, the lineshape was found to be independent of total neutron fluence for the range of doses which were employed.

Exposure to the reactor core (n + γ) flux resulted in lineshapes which depended on the amount of exposure. Figure 1.21 shows the lineshape resulting from exposure to $1.4 \cdot 10^{17}$ n/cm^2. The line appears to have structure which is a mixture of the lines in Fig. 1.19 and Fig. 1.20.

Exposure of Suprasil W1 to the thermal column (n + γ) flux resulted in relatively low spin densities and a lineshape similar to the usual E' lineshape of Fig. 1.11.

2. Spin Density Measurements

Figure 1.14 also shows the results of absolute spin density measurements of Suprasil W1 exposed to Co^{60} radiation. It appears that the spin density is not linearly related to the total exposure, and there may be a slight "jump" in the density at an exposure of about 10^6 rads. At higher exposures the density increases in a smooth fashion as the irradiation increases, and there is no evidence of a "saturation" of the spin density.

Figure 1.15 also shows the spin density measurements of Suprasil W1 exposed to 14 MeV neutrons. Figure 1.22 shows the results for exposure to the reactor (n + γ) flux. For exposure to both 14 MeV neutrons and the reactor core, the Suprasil W1 linearly related to the total neutron fluence, with no evidence of saturation of the spin density. Figure 1.22 also shows the results for exposure to the thermal column (n + γ) flux; the spin density is relatively low and appears to be linearly related to the neutron fluence.

3. Saturation Behavior

Most of the Suprasil W1 EPR spectra exhibited saturation behavior which was typical of the E' saturation shown in Fig. 1.17.

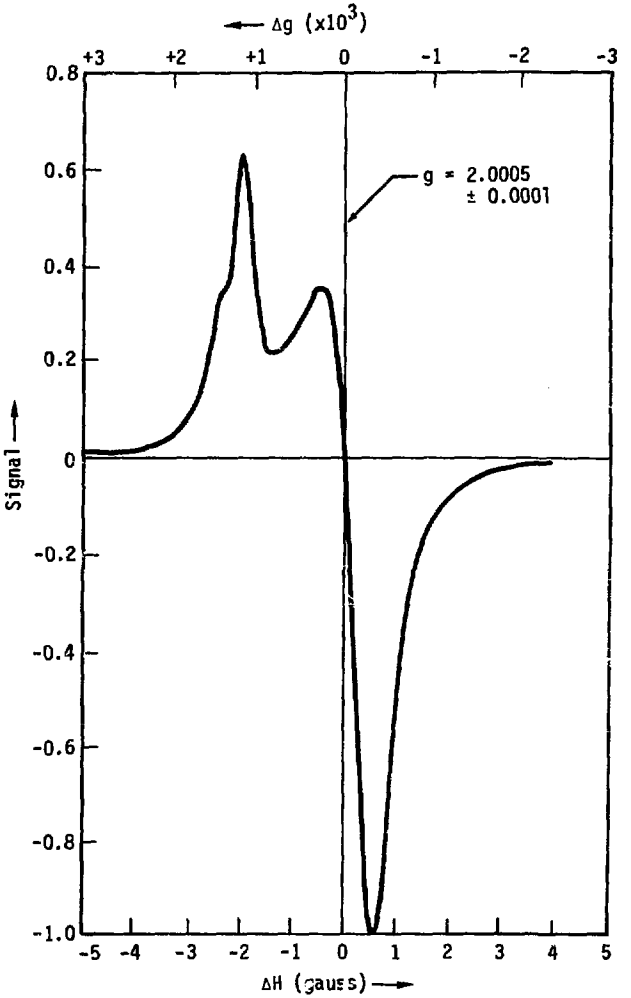

Figure 1.21 E' Spectrum of Reactor Core Irradiated Suprasil W1

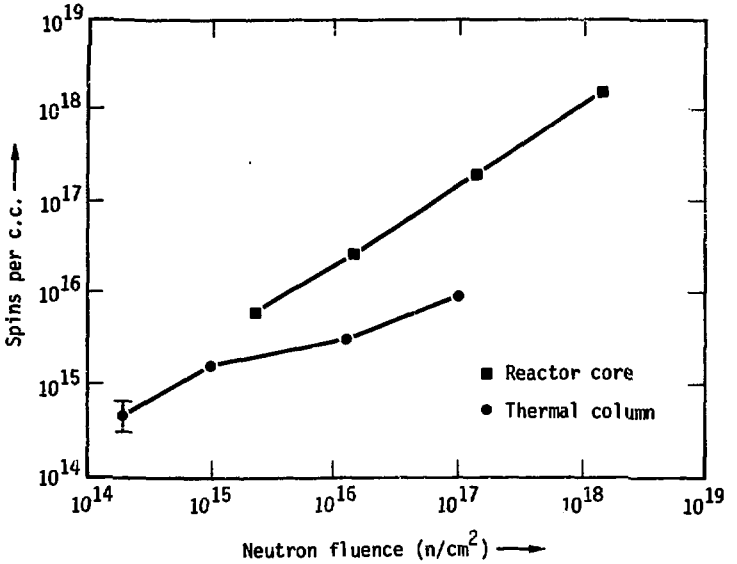

Figure 1.22 Spin Densities in Reactor Irradiated Suprasil W1

See Fig. 1.16 for an explanation of the neutron fluences in this figure.

However, Suprasil W1 samples exposed to about $5 \cdot 10^{16}$ 14 MeV n/cm^2 (or also to $1.4 \cdot 10^{18}$ reactor core neutrons) required about three times the normal amount of power to saturate the signal. Suprasil W1 samples exposed to the thermal column (n + γ) flux had spin densities too low to determine their saturation behavior.

D. Quartz Crystal

1. EPR Lineshapes

An EPR spectrum of Co^{60} irradiated quartz crystal is shown in Fig. 1.23. The lineshape of this system has very sharp (~40 mG) structure and is very sensitive to the crystal orientation in the magnetic field. Comparison of this lineshape with that of other samples was very difficult because we had no means for accurately and reproducibly orienting the samples in the field. In addition, power line voltage fluctuations rarely allowed the magnetic field stability necessary to precisely determine the lineshapes.

2. Spin Density Measurements

In spite of the problems associated with lineshape analysis for crystalline samples, we were able to obtain approximate spin density measurements for samples exposed to Co^{60} γ-ray and 14 MeV neutron irradiation. The results are shown in Figs. 1.24 and 1.25, respectively. In both cases, the spin density appears to be roughly proportional to the irradiation.

3. Saturation Measurements

Because of the magnetic field instability and the narrow quartz linewidths we were unable to determine the saturation behavior of the crystalline samples.

E. Experimental Problems

It has been mentioned in a previous section that many of our early EPR studies of radiation damage were characterized by confusing and irreproducible results. These problems were encountered during our first

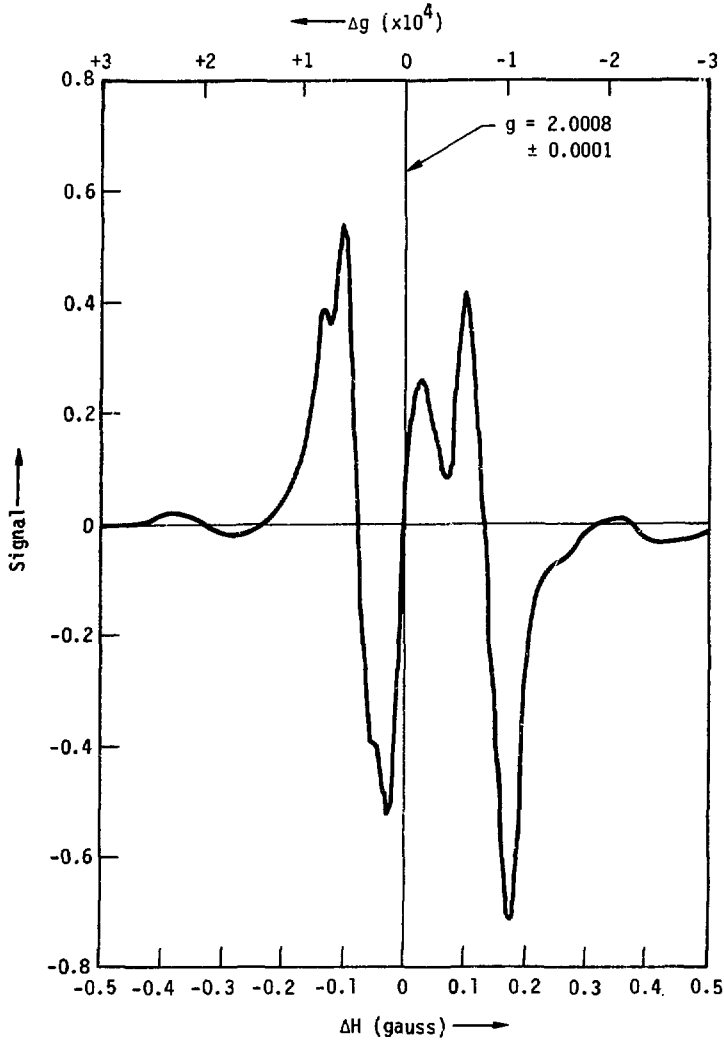

Figure 1.23 E' Spectrum of Co^{60} γ-ray Irradiated Quartz Crystal

This spectrum was recorded with the crystal c-axis approximately parallel to the magnetic field.

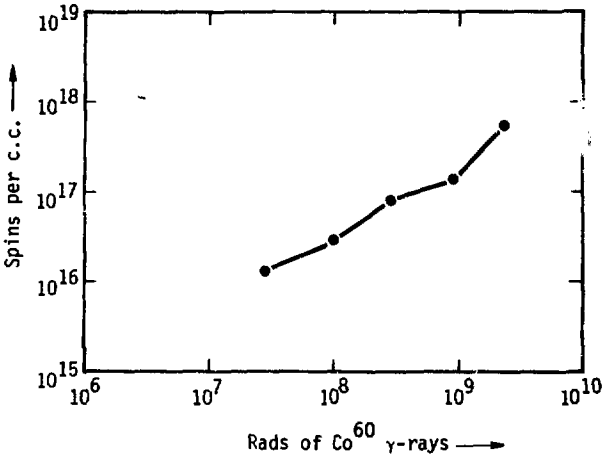

Figure 1.24 Spin Densities in Co^{60} γ-ray Irradiated Quartz Crystal

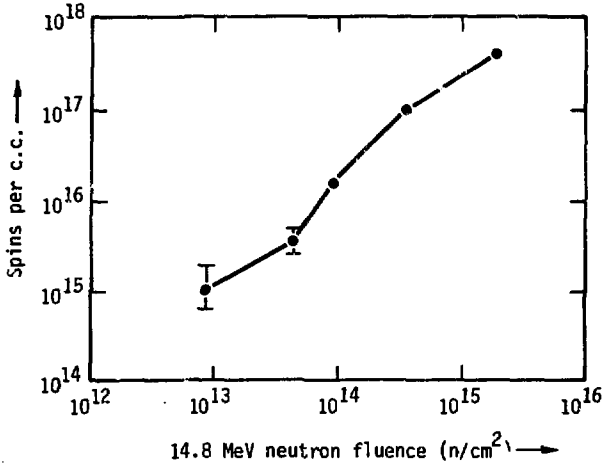

Figure 1.25 Spin Densities in 14.8 MeV Neutron Irradiated Quartz Crystal

attempts to characterize the EPR of E' centers due to Co^{60} gamma rays in Suprasil. The "puzzling" results included signals detected 90° out of phase from the absorption ($\chi''(\omega)$) signal (for a "pure absorption mode" measurement, there is no signal 90° out of phase), changes in the lock-in phases at which the signals were detected as a function of microwave power, an inability to reproduce previously published spectra of the E' center in Suprasil due to Co^{60} gammas and (sometimes) an inability to reproduce our own data. Eventually, the sources of these problems were isolated and eliminated; and all subsequently recorded spectra were free of the problems.

There were three major sources of the problems mentioned above: passage effects, saturation of inhomogeneous systems and improper tuning of the klystron frequency. Passage effects have been reported as the source of "out of phase" signals of the type observed here and the phenomena behind this behavior is well understood.[41,42] A combination of some unique features of inhomogeneous saturation and improper klystron frequency control also lead to an "out-of-phase" signal. These two different signals will be briefly described below.

It is well known that passage effects can lead to "out-of-phase" signals which have spectra similar to an ordinary absorption spectrum.[43,44] In addition, the phase of these signals is a function of microwave power and of the signal detection frequency. However, roughly speaking, this behavior occurs only when:

$$\omega_m > \frac{1}{T_1} \quad . \tag{1.104}$$

For the early E' EPR measurements, the spectrometer was operated in a simple homodyne arrangement which used a magnetic field modulation and signal detection frequency of about 100 khz. For the E' center, where

$$\frac{1}{T_1} \approx 500 \text{ hz} \tag{1.105}$$

this was clearly a situation where passage effects would occur. As a result, the characteristics of the E' spectra which were measured depended not only on the E' centers, but also on the spectrometer operation (microwave power and signal detection phase). In order to avoid the effects of passage effects, the spectrometer was converted to a superheterodyne receiver and modulation and detection frequencies of about 40 hz were used.

Much to our surprise, with the superheterodyne spectrometer operating with detection frequencies of 40 hz, "out-of-phase" signals were detected with spectra similar to a simple $\chi''(\omega)$ absorption curve. However, the lock-in phase at which this signal was detected did not vary with modulation frequency ω_m or microwave power, so it was not due to passage effects. However, this signal was detected only when microwave power sufficient to saturate the E' centers was used. The source of this signal is somewhat subtle and is due to a combination of improper klystron frequency control and inhomogeneous saturation. It has been mentioned above that when the klystron frequency exactly matches the cavity-sample resonant frequency, the signal detected coming from the cavity is due entirely to $\chi''(\omega)$. However, when the klystron frequency doesn't exactly match the resonant frequency, the reflected signal is due to a combination of $\chi'(\omega)$ and $\chi''(\omega)$. Figure 1.26 shows the "out-of-phase" spectrum as a function of klystron frequency mismatch. The signal is seen to yield a noisy spectrum whose amplitude and sign is proportional to the frequency mismatch. The relatively high level of noise is due to the frequency noise of the klystron output. This out-of-phase signal is due to $\chi'(\omega)$ (and is detected 90° out of phase from $\chi''(\omega)$), but has the spectrum of a simple $\chi''(\omega)$ absoption curve because the klystron frequency mismatch is maintained at the same value as the resonance is traversed by the spectrometer. As a result, the out of phase signal has an amplitude proportional to the reflected microwave power and leads to a simple absorption spectrum.

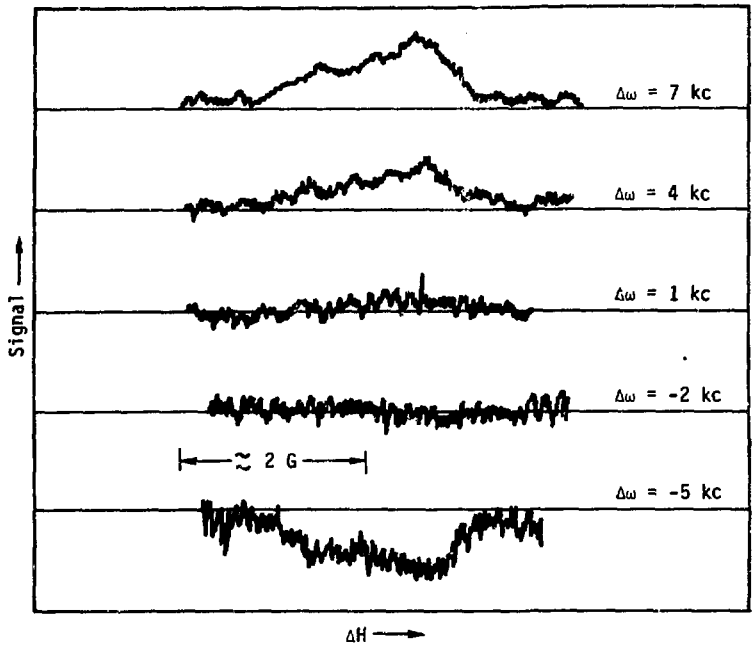

Figure 1.26 Out-of-Phase Spectra

This figure consists of several tracings of out-of-phase spectra which were recorded for different klystron settings. The deviation of the klystron frequency from the correct cavity resonant frequency is indicated for the individual spectra. It appears that the amplitudes and signs of the spectra are proportional to the klystron frequency mismatch.

The saturation properties of inhomogeneous systems tend to enhance the size of this out-of-phase signal as the resonance is saturated. We have shown above that the amplitude of $\chi''(\omega)$ saturates (roughly) as $S^{-1/2}$. Portis has shown in addition that the amplitude of $\chi'(\omega)$, to a first approximation, does not saturate, but has a constant value. Thus, while under extreme saturation $\chi''(\omega)$ may be reduced by 10 or 10^2, $\chi'(\omega)$ has a constant amplitude. As a result, a small klystron frequency mismatch will lead to only a small change in the absorption signal, but, because of the relatively large amplitude of $\chi'(\omega)$, may also lead to a much larger dispersion signal than would normally be expected.

After isolating the sources of the out-of-phase signals in the system it was relatively simple to eliminate them. Using a detection frequency of about 40 hz and carefully controlling the klystron frequency resulted in conventional EPR spectra. The resulting spectra are believed to be correct, although they do not exactly match previously reported spectra[95] (see Fig. 1.27). This is because the previously reported spectra were recorded with experimental conditions where passage effects and inhomogeneous saturation occurred. It is because of the extreme care which was used to record the spectra presented here that distinctions between the EPR of fused silicas exposed to different radiation sources have been resolved.

F. Bk7 Glass

1. EPR Spectra

All four radiation sources were used for irradiation of Bk7 samples. The resulting lineshapes depended on the kind and amount of radiation that the sample was exposed to.

The EPR spectrum resulting from exposure of Bk7 to Co^{60} γ-radiation is shown in Fig. 1.28. The line is seen to be a broad, asymmetric line with a zero crossing near g = 2.0. For Co^{60} irradiation, the lineshape was independent of the amount of exposure.

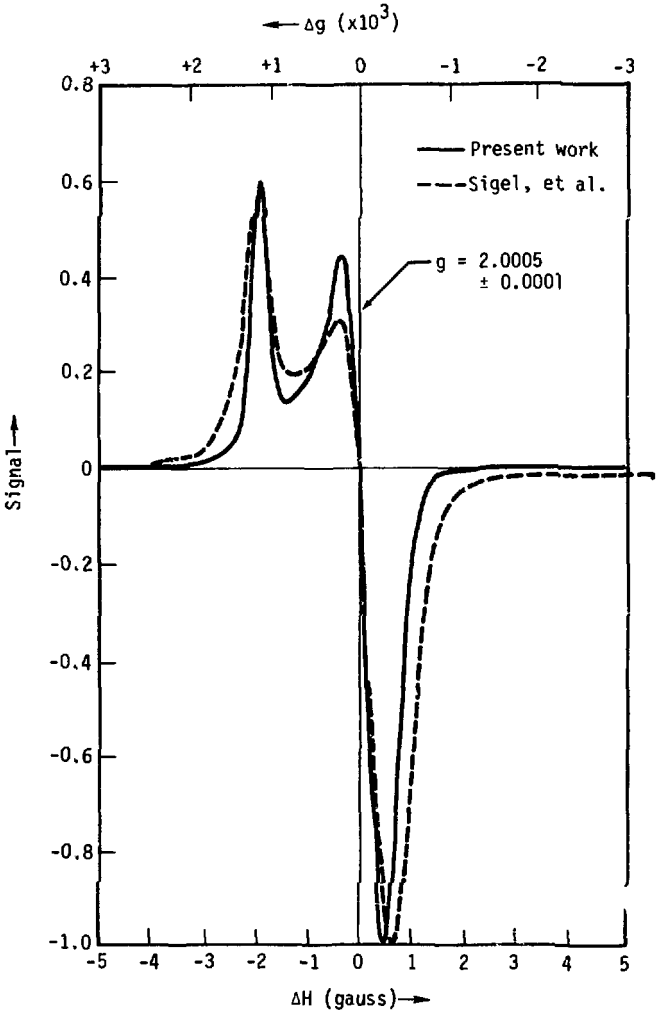

Figure 1.27 Comparison of E' Spectra

This figure shows our simplest E' spectrum (Co^{60} γ-ray irradiated Suprasil 1) and a similar spectrum recorded by Sigel, et al.[45] for comparison purposes.

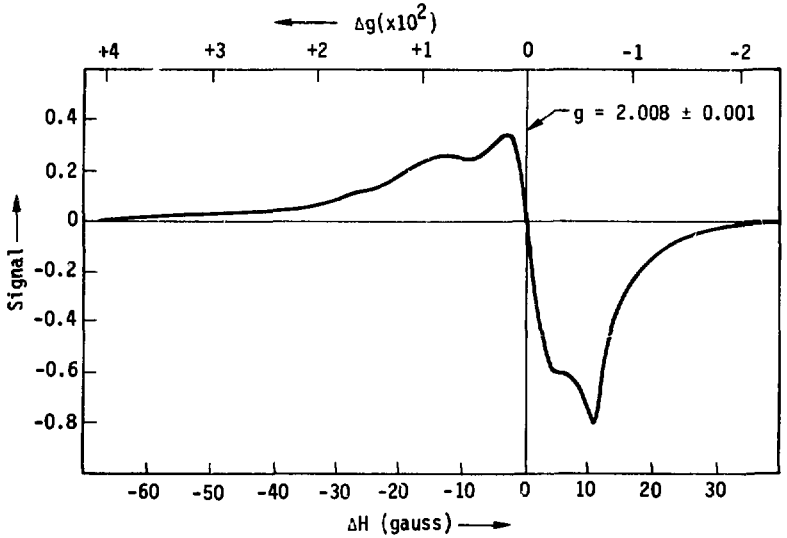

Figure 1.28 EPR Spectrum of Co^{60} γ-ray Irradiated Bk7 Glass

Figure 1.29 shows an EPR spectrum resulting from exposure to 14 MeV neutrons. The lineshape is basically the same as the line in Fig. 1.28, except that a narrow spike has been added at g = 2.0009. For exposure to 14 MeV neutrons, the lineshape was independent of the exposure over the range of doses which were used.

Exposure to $1.8 \cdot 10^{18}$ reactor core n/cm^2 resulted in the spectrum of Fig. 1.30. This spectrum appears to be a combination of the spectra due to Co^{60} γ-rays (Fig. 1.28) and 14 MeV neutrons (Fig. 1.29). For lower doses of reactor core neutrons, the EPR spectra were very similar to the spectra associated with 14 MeV neutrons.

Figure 1.31 shows the EPR spectrum resulting from exposure to 10^{17} neutrons in the thermal column. The lineshapes for exposure to the thermal column depended slightly on the total dose.

2. Spin Density Measurements

Figure 1.32 shows the results of the absolute spin measurements on Bk7 exposed to Co^{60} radiation. The plot is nearly constant at a relatively high spin density and roughly linear for the exposures between 10^6 and 10^9 rads. Since we performed no irradiations with doses less than 10^6 rads, we were unable to determine at what dose the spin density reaches its roughly constant value of 10^{18}/cm^3.

Exposure to 14 MeV neutrons resulted in the spin density measurements shown in Fig. 1.33. Below integrated fluences of $2 \cdot 10^{15}$ n/cm^2, the spin density decreases linearly as the fluence decreases; for doses above 10^{15} n/cm^2, the density levels off slightly but continues to increase.

Figure 1.34 shows the spin density measurements for exposure of Bk7 to the reactor core and thermal column (n + γ) fluxes. The two different

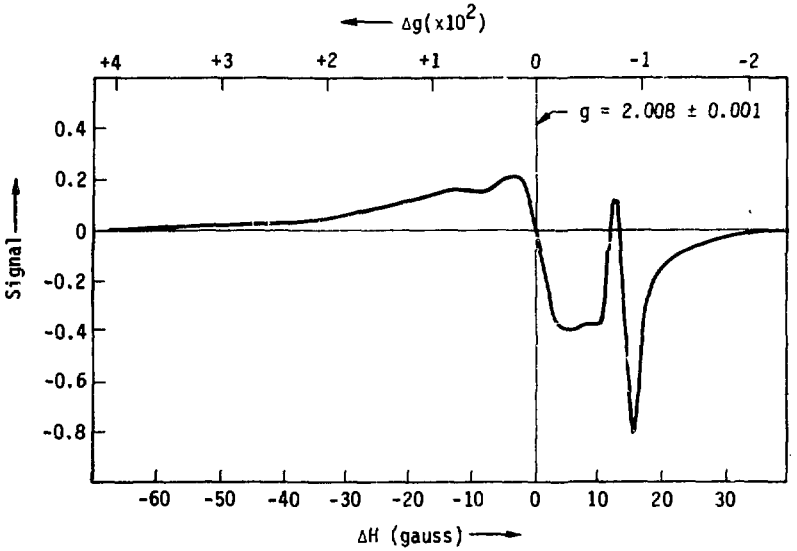

Figure 1.29 EPR Spectrum of 14.8 MeV Neutron Irradiated Bk7 Glass

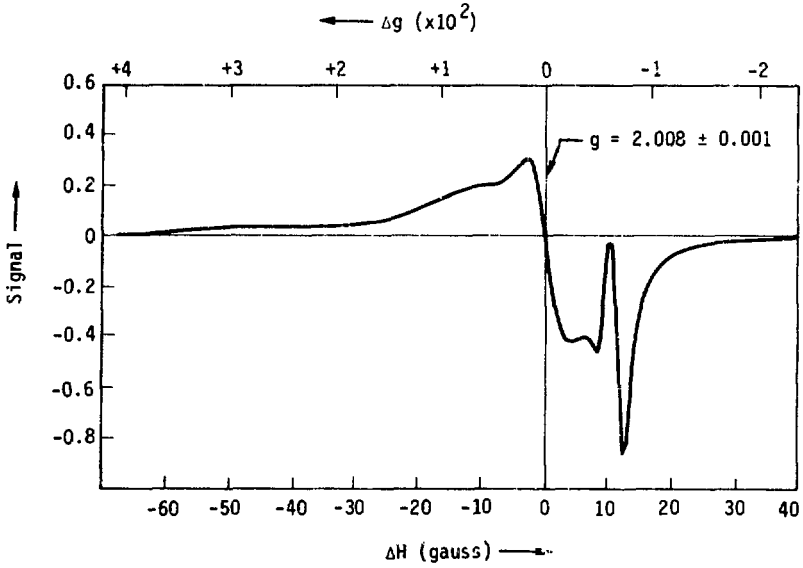

Figure 1.30 EPR Spectrum of Reactor Core Irradiated Bk7 Glass

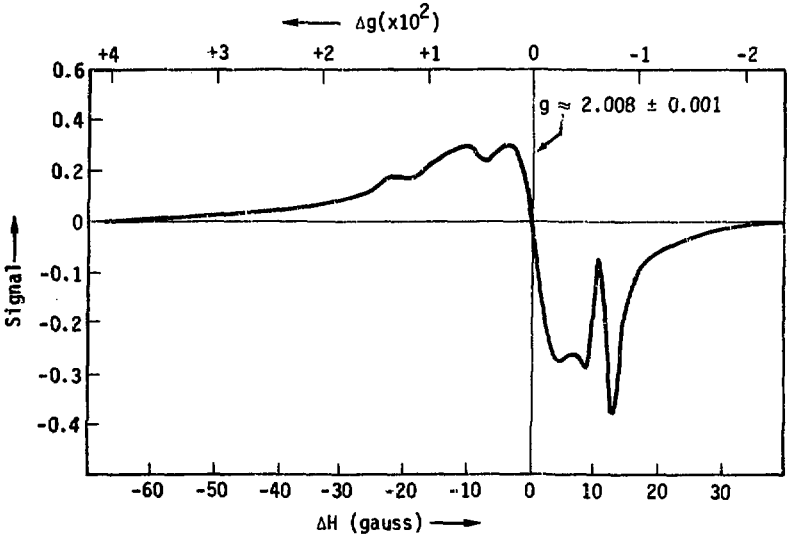

Figure 1.31 EPR Spectrum of Thermal Column Irradiated Bk7 Glass

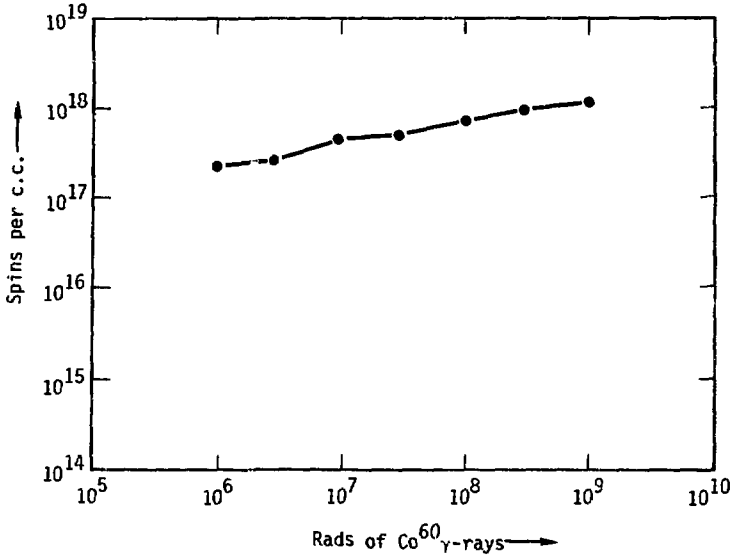

Figure 1.32 Spin Densities in Co^{60} γ-ray Irradiated Bk7 Glass

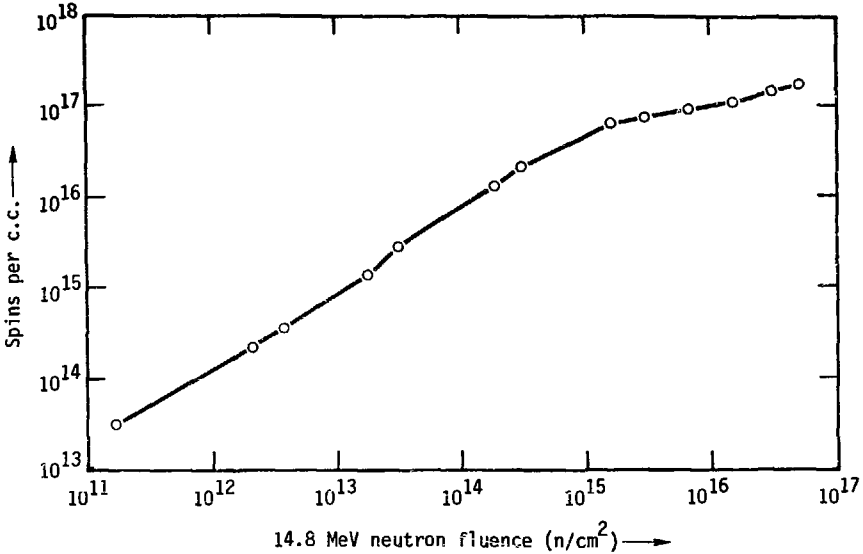

Figure 1.33 Spin Densities in 14.8 MeV Neutron Irradiated 6k7 Glass

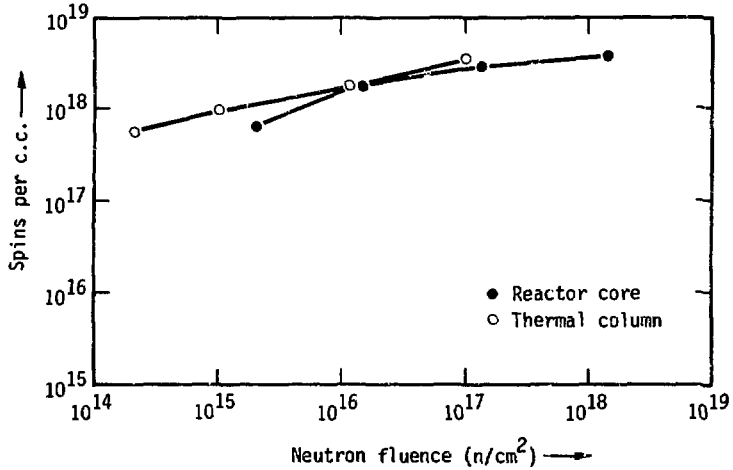

Figure 1.34 *Spin Densities in Reactor Irradiated Bk7 Glass*

See Fig. 1.16 for an explanation of the neutron fluences in this figure.

radiations yield similar spin densities. The spin density appears to be nearly saturated at a value of about $5 \cdot 10^{18}/cm^3$.

3. Saturation Behavior

No careful study has been made of the saturation behavior of the Bk7 spectra. The main reason for this is that our klystron power was insufficient to induce large saturation effects on the broad, asymmetric line. We were unable to saturate the line shown in Fig. 1.28. However, we were able to saturate and saturation-broaden the narrow g = 2.0009 peak of some of the Bk7 spectra (as in Fig. 1.29).

Figure 1.35 shows the effect of saturation-broadening of the g = 2.0009 peak. With H_1 equal to 200 mG the spike cannot be clearly resolved from the rest of the line, but with H_1 equal to 20 mG the peak is well-resolved.

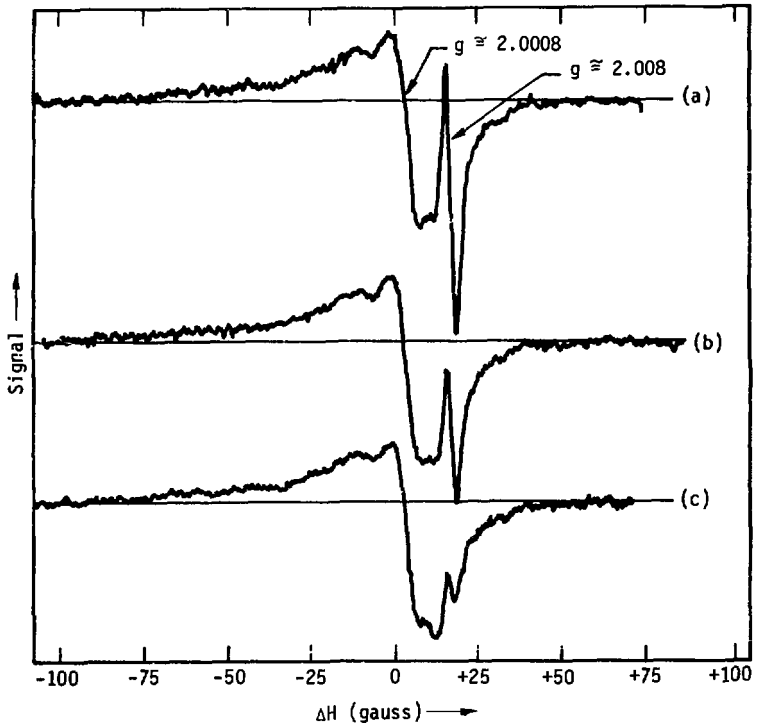

Figure 1.35 Differential Saturation of Bk7 Spectrum

These spectra demonstrate the saturation of the g = 2.0008 spike in the EPR spectrum of 14.8 MeV neutron irradiated Bk7 glass. For H_1 = 0.2 G, the spike is nearly completely saturated, while the broad, asymmetric lineshape is unaffected. In plots (a), (b), and (c) the microwave magnetic field amplitudes are 3, 30, and 100 milligauss, respectively.

V. DISCUSSION

A. Introduction

In this section, analysis of the data presented above will be applied to the investigation of radiation damage in glasses. Much of the data analysis is based on the comparison of EPR data for different experimental situations. Comparison of EPR lineshapes, paramagnetic spin densities and power saturation behavior associated with exposure to different radiation sources (e.g., Co^{60} gammas vs. 14 MeV neutrons) has been particularly useful. Rather than attempting an extensive, detailed analysis of the EPR data in order to determine the precise microscopic nature of particular paramagnetic centers, the present analysis exploits a number of different interpretations of the data in an effort to illuminate fundamental physical behavior associated with radiation damage. These efforts have resulted in a number of interesting conclusions concerning radiation damage and have demonstrated the internal self-consistency of our data and analysis.

EPR lineshapes, spin densities and power saturation behavior are the three main aspects of the data that are used in our analysis. The analysis of EPR spectral lineshapes in glasses has a number of advantages and disadvantages as a technique for investigation of radiation damage. The EPR spectra associated with radiation damage are interesting and important because they are directly related to the microscopic nature of the paramagnetic centers. In addition, comparison of EPR spectra for different experimental situations can be an extremely powerful analytical tool even when the natures of the individual EPR spectra are not completely understood, because differences in EPR spectra imply differences in the nature of the associated microscopic paramagnetic centers. However, because of the poorly understood relationship between EPR spectra and the nature of radiation damage, interpretation of EPR spectra must be performed very carefully. This is particularly true for glasses, where many different

types of centers may contribute to a particular EPR signal (as in Bk7 glass) and where anisotropic g-tensors associated with particular types of paramagnetic centers lead to inhomogeneous broadening of the systems. For example, the measurement of identical EPR spectra for two different experimental situations does not necessarily imply that the nature of radiation damage in both systems is identical; it only demonstrates that the EPR spectra of the paramagnetic centers in both systems is the same.

Measurements of the spin density and relaxation times (from power saturation behavior) of a system are also very useful. In addition to providing fundamentally useful data, these measurements can sometimes be used to demonstrate the overall self-consistency of the EPR data. This is the case, for example, in systems with high paramagnetic spin densities where interactions between individual dipoles result in observable effects in the associated EPR spectra.[46] The changes in the EPR spectra can then be analyzed to predict the spin densities or power saturation behavior to be expected for the system. Analysis of this type for one of our samples has verified the self-consistency of the EPR data and has also suggested that paramagnetic centers in the sample occur at isolated sites, rather than in "clusters."

While the analysis of EPR data from irradiated Suprasil samples is necessarily beset with the complications associated with EPR powder lineshapes in glasses, the overall properties of these glasses make them a nearly ideal system for the study of radiation damage. The chemical purity and relative simplicity of these glasses establishes them as an extremely well-defined system to study. The linewidths (~1 gauss) and relaxation times ($T_1T_2 \gtrsim 100$ ns) of the E' centers in these glasses are such that the centers can be investigated by a number of different techniques. For example, the spectral resolution of the experiments has resulted in the resolution of details in the EPR spectra which establish that there are

at least two different kinds of paramagnetic centers which occur in these materials. One of these centers occurs with very low densities with Co^{60} γ-ray irradiation, but with relatively high densities for fast neutron irradiation, suggesting that this defect is associated with atomic displacement events in the material. The narrow linewidth of the F' spectra has also allowed the use of saturation and dipole-dipole broadening in these materials to roughly determine the relaxation times associated with these centers. These have been a few examples of the conclusions and speculations that have been made on the basis of EPR studies of irradiated Suprasil samples.

Analysis of the EPR data obtained from irradiated Bk7 glass has also yielded a number of interesting results. Because of the complicated nature of Bk7, it is not as ideal a material as the Suprasils for EPR investigations. While, in principle, a detailed analysis of Bk7 lineshapes to determine the nature of the related paramagnetic centers is possible, such a study is well beyond the scope of the present experiments. Our interpretation of the EPR data obtained from Bk7 glass is based largely on the comparison of data for different experimental conditions. For example, comparison of the EPR lineshapes resulting from exposure to Co^{60} gamma and 14 MeV neutron radiations suggests that the broad asymmetric lineshape in Bk7 (see Fig. 1.27) is due primarily to electron occupation of excited state energy levels at multivalent atomic sites in the glass structure. Further analysis of the data has led to additional information and will be presented below.

While the information gained from EPR investigations of radiation damage is interesting and useful, the results of these studies will attain their maximum usefulness if they can be related to gross physical properties of the material of interest. In order to examine the possibility of the existence of such relationships, the results of our EPR investigations

have also been compared to several quantities of fundamental interest in radiation damage. For example, energy deposited in a material through atomic displacement events is probably closely related to changes in the bulk mechanical properties of the material; thus, paramagnetic spin densities have been compared to the expected density of displacement events in the material. On the other hand, changes in material properties such as the optical absorption spectra are probably closely related to energy dissipated in ionizing electronic collisions in the material; thus, the energy expected to be dissipated in ionizing collisions has been compared to the measured spin densities for some systems. The results of these comparisons suggest that in some well defined experimental situations, EPR can probably be used as an excellent technique for the study and prediction of changes in bulk physical properties due to radiation damage.

B. Spin Densities

1. Introduction

Absolute measurements of the paramagnetic spin densities in irradiated materials supply unique data which can be used in a number of ways to investigate radiation damage behavior. Although a single spin density measurement cannot generally be directly related to the microscopic nature of radiation induced defects, the relative importance of different microscopic damage mechanisms can often be determined by comparison of spin densities associated with different radiations or materials. For example, comparison of spin densities resulting from x-ray and 14 MeV neutron irradiation can be used to compare the relative magnitude of spin densities resulting from primary collisions consisting of electron ionization (by x-rays) and atomic displacements (by elastic collisions with 14 MeV neutrons). Since radiation induced spin densities are sensitive to most of the experimental variables in a damage study, there is a large variety of comparative studies of this type which can be used to investigate specific systems.

In some cases, spin density measurements can be used to supplement the data obtained with other types of EPR measurements. For example, with relatively high levels of spin density, it is possible to produce an observable dipole-dipole broadening of inhomogeneous lines.[46] When this "dipole-broadening" can be measured, it can be analyzed to predict the average spin-spin separation (or average density) associated with the broadening. If the measured spin density is nearly equal to the density estimated from spectral broadening, the two measurements together imply that the paramagnetic spins occur at random positions in the material; because, if the paramagnetic spins occurred in clusters in the material, the spectral broadening would indicate higher spin densities (or smaller average separations) than the results of the spin density measurements. A similar type of comparison can also be used to help interpret the power saturation behavior of a system.

There are a number of difficulties with the use of spin density measurements to study radiation damage behavior. Most of these problems arise from the uncertain nature of the relationship between EPR and radiation damage. One particularly important problem is that microscopic damage sites not associated with an unpaired electron spin cannot be directly detected by EPR. Thus, it is possible for microscopic damage not associated with paramagnetic defects to be an important factor in radiation damage behavior without being detected in EPR measurements. This point emphasizes the statement made above that, while differences in EPR behavior imply differences in radiation damage, it is not necessarily true that the presence of identical EPR characteristics for two different systems implies the presence of identical radiation damage.

The discussions of the data in the remainder of this section are organized on the basis of the different types of radiation used in the experiments. This is because the well-defined radiation sources at LLL

allow the data obtained with the use of a particular source to be discussed with respect to the specific damage mechanisms expected to be associated with each type of radiation. This organization is not rigorously maintained, but only used as a guideline for directing the discussion. A similar approach will also be used to discuss the other types of EPR data in future sections.

2. Co^{60} radiation

For the 1.17 and 1.33 MeV gamma rays emitted by a Co^{60} source the dominant scattering mechanism in low-Z materials is collisions with electrons via the Compton effect. The scattered electrons produced by the primary Compton collisions dissipate their energy in a cascade of Coulombic collisions with electrons and ions in the material. Most of the scattered electron energy is dissipated in collisions resulting in electron ionizations;[47] but some of the energy is also dissipated in atomic displacement collisions.[48] For the convenience of the discussion of the spin density measurements, the radiation damage effects due to Co^{60} gamma rays will be assumed to be due primarily to electron ionization processes in the material. Atomic displacment events in the material may also make a significant contribution to the overall radiation damage behavior; and the importance of these contributions will be discussed in a later section.

Figure 1.36 shows the results of the absolute spin density measurements performed on Suprasils I and W1 and Bk7 glass exposed to Co^{60} gamma rays. This data has a number of interesting features. The most outstanding feature of this data is that the spin densities in Bk7 glass are from one to three orders of magnitude greater than the corresponding spin densities in the Suprasils. For the lower doses, the spin densities in Bk7 correspond to about 10^2 paramagnetic spins per initial Compton collision in the material, while the spin densities in the Suprasils correspond to about one paramagnetic spin per Compton collision. At a first glance, this

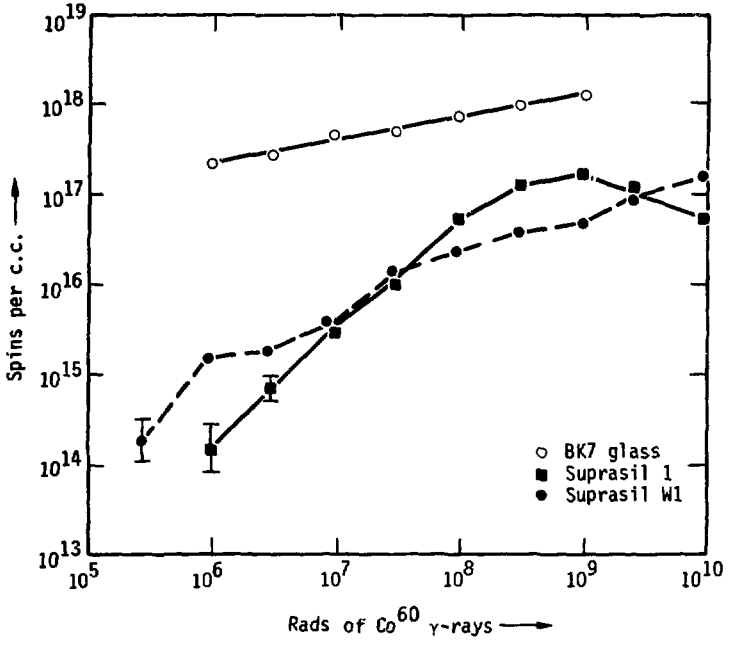

Figure 1.36 Spin Densities in Co^{60} γ-ray Irradiated Samples

difference in spin densities may seem surprising, because the rate of production of ionized electrons by gamma rays is roughly the same in all three different glasses (because they all have nearly the same electron density).

However, the differences in paramagnetic spin densities are not due to differences in the production of ionized electrons, but are due rather to differences in the nature of the states which can be occupied by ionized electrons in the different glasses. In Bk7, the fairly large densities of multivalent impurities and constituents acts as a large density of electron (or hole) trapping sites which can be occupied by ionized electrons—leading to large densities of paramagnetic spins. But in the Suprasils, the low concentration of metallic impurities (<1 ppm) results in the near absence of electron (or hole) traps at multivalent ion sites, and ionized electrons must occupy either a state vacated by an electron ionization collision or intrinsic traps in the glass structure—leading to relatively low densities of paramagnetic spins.

The spin densities in the Suprasil samples exhibit several interesting features. The spin densities versus Co^{60} dose for Suprasil I and Suprasil W1 are roughly the same order of magnitude, but also have differences in their behavior. While the spin density versus dose for Suprasil W1 is roughly a linear function of the doses used, the spin density versus dose for Suprasil I is a smooth function of Co^{60} does with a maximum value of about 10^{17} spins/c.c. at a dose of 10^9 rads. At doses higher than 10^9 rads, the spin density in Suprasil I actually decreased.

The differences in the spin densities versus dose of Suprasil I and Suprasil W1 illustrate an interesting problem in the comparison of the radiation damage behavior of two materials. For the Suprasils, at doses below 10^7 rads and above $3 \cdot 10^9$ rads, Suprasil W1 has a higher spin density than Suprasil I; but at doses between $3 \cdot 10^7$ rads and $3 \cdot 10^9$ rads, it

is Suprasil I which has the greater spin density. This behavior demonstrates that it is difficult to specify the relative radiation damage behavior of some materials. In order to make a meaningful comparison of the spin densities in Suprasil I and Suprasil W1 due to Co^{60} γ-rays, it is necessary to specify the behavior for the entire range of doses of interest.

The presence of different spin densities in Suprasil I and Suprasil W1 exposed to Co^{60} radiation is an interesting result in itself. The spin density results for the Suprasils demonstrates that when comparing the radiation damage behavior of two similar materials, it is necessary to consider possible consequences of the fabrication techniques used for the two materials. The measured spin densities in the Suprasils are relatively low because of the absence of metallic impurities in both of them. Any differences between Suprasil I and Suprasil W1 must be due to the different fabrication techniques used for them. The major resulting chemical difference between the two glasses is the relatively low OH content of Suprasil W1, but it is not clear how this difference can directly affect the radiation damage behavior.

3. 14 MeV neutrons

The 14.8 MeV neutron irradiation of our samples led to radiation damage primarily through elastic collisions with atomic nuclei in the material. The primary knock-ons produced in these collisions create atomic displacements in the material in a cascade of elastic collisions; and if the knock-on energy is high enough, also dissipate energy in ionizing collisions with electrons in the material. The relative importance of atomic displacement and electronic ionization mechanisms depends on the fast neutron energy and the type of material being irradiated.

There is also a variety of inelastic nuclear scattering mechanisms (such as the (n,γ) reaction) which can interact with the incident neutron

flux.[49] For SiO_2, the contribution to radiation damage effects by these mechanisms is generally much less than the effects associated with elastic scattering of atomic nuclei. The magnitude of the importance of inelastic scattering events will be briefly considered later in the discussion of the data.

Figure 1.37 shows the results of the absolute spin density measurements performed on Suprasil I, Suprasil W1 and Bk7 glass exposed to 14.8 MeV neutrons. The most striking feature of this data is that, compared to spin densities due to Co^{60} irradiation, the measured spin densities are remarkably similar for all three glasses. Except for the "jump" in the spin density of Suprasil I at a fluence of about 10^{15} n/cm^2, the spin density versus dose is a roughly linear function for all three glasses. The presence of the "jump" in the Suprasil I spin density at fluences about 10^{15} n/cm^2 was repeatedly confirmed with about eight different Suprasil samples.

It is interesting to speculate on the significance of the similar spin densities measured in all three glasses. If radiation damage effects due to exposure to 14.8 MeV neutrons are caused only by atomic displacement events in the glasses, then the similar spin densities are easy to understand because the number of atomic displacements should be roughly the same in all three glasses.[50] The spin densities in Fig. 1.36 correspond to the creation of about 50 paramagnetic spins per primary collision with 14.8 MeV neutrons, and this is not an unreasonable number of displacements to be caused by the primary knock-ons. Thus, an assumption that paramagnetic spin densities due to exposure to 14.8 MeV neutrons are due entirely to atomic displacement collisions would be completely consistent with the spin density data.

But it is difficult to understand how electronic ionization processes cannot be an important factor in 14 MeV neutron radiation damage effects.

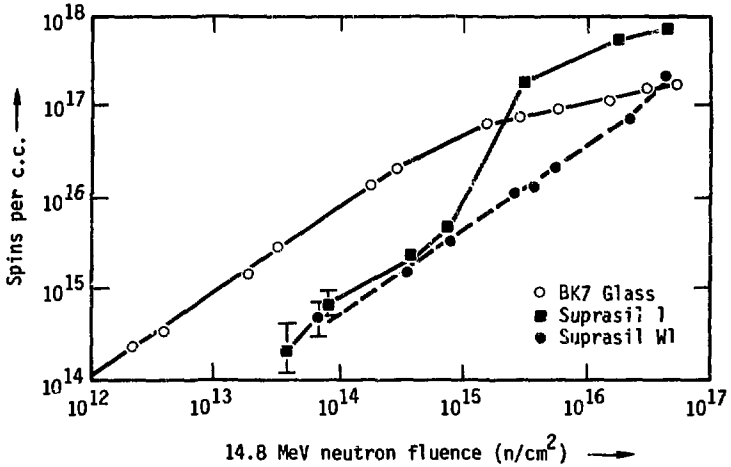

Figure 1.37 Spin Densities in 14.8 MeV Neutron Irradiated Samples

The energies of the Si and O primary knock-ons (~1.5 MeV) is high enough that a majority of their energy should be dissipated in electronic scattering events.[50] In general, ionization events are important scattering mechanisms whenever the energy of the ion in KeV is greater than the atomic number of the ion (see eq. (1.61)).[51] Thus, although there is a well defined source of ionized electrons in 14 MeV neutron irradiation, the spin densities suggest that these ionized electrons do not appear to result in paramagnetic spin states, as they do in Co^{60} irradiation of Bk7 glass.

There is a potentially important difference in the energy spectra of electrons ionized during 14.8 MeV neutron irradiation and Co^{60} γ-ray irradiation. During 14.8 MeV neutron irradiation, energetic Si and O ions (with energies ($\sim 10^4$ MeV), as they propagate through the material, ionize atomic electrons and transfer about 10^2 eV kinetic energy to them. But during Co^{60} irradiation, Compton collisions create electrons with an average energy of about 0.5 MeV.[47] The relativistic electrons propagate through the materials ionizing additional electrons in a collision cascade and losing a significant fraction of its remaining energy to each collision. Because of their low energy ($\sim 10^2$ eV), the electrons ionized during 14 MeV neutron irradiation will not propagate through the material creating large numbers of additional energetic electrons, and will only be able to ionize a few additional electrons, without imparting large kinetic energies to them. These differences in the electron dynamics of the two systems may be a major reason for the differences in paramagnetic spin densities resulting in Bk7 glass from Co^{60} and 14.8 MeV neutron irradiation. Some details of the consequences of these different scattering mechanisms will be considered in a section below.

4. Thermal Neutrons

The thermal neutron irradiations were performed in the West-thermal-column stringer irradiation facility of the LPTR. The radiation field of this facility does not consist solely of thermal neutrons (E_n = .025 eV) but consists of a graphite-moderated spectrum of reactor core neutrons with ratios of thermal-to-fast neutron fluxes varying from 10:1 to 300:1.[37] There is also a sizeable γ-ray flux with a spectrum similar to the reactor core γ-ray spectrum. Thus, radiation damage in this facility is due to the effects of thermal neutrons, fast neutrons and gamma rays. The radiation behavior of fast neutrons and gamma rays has been discussed above and their importance for these irradiations depends on the relative fluxes involved.

The radiation flux in the thermal column is dominated by the thermal neutron flux ($\simeq 10^{11}$ n/cm^2·s). In Bk7, the thermal neutrons will have important radiation damage consequences due to the nuclear reaction

$$n + B^{10} \rightarrow Li^7 + \alpha + 3.3 \text{ MeV} \qquad (1.4)$$

which has a very large cross section ($\sigma \sim 4 \cdot 10^3$ barns) for thermal neutrons. The energetic Li and α charged particles released by this reaction will propagate through the glass structure and are capable of creating atomic displacements and electronic ionizations by the mechanisms discussed above. In the Suprasils, the absence of nuclear reactions with large cross sections and the low energy of the incident neutrons means that the thermal neutrons are not expected to induce high levels of radiation damage or the associated paramagnetic spins.

Figure 1.38 shows the results of the spin density measurements performed on Suprasil I, Suprasil W1 and Bk7 glass exposed to the thermal column radiation flux. The thermal column radiation field is the most complicated radiation source encountered thus far in the discussion of

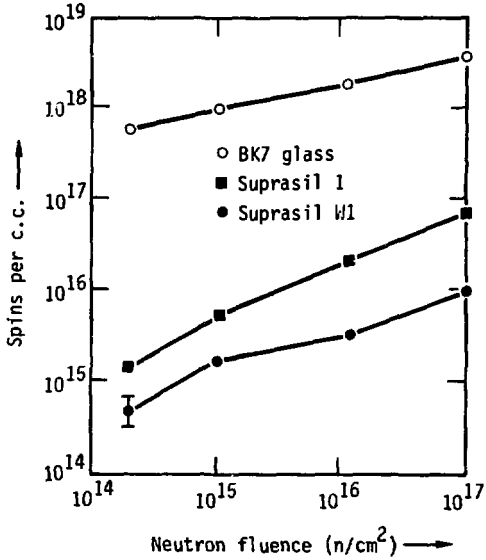

Figure 1.38 Spin Densities in Thermal Neutron Irradiated Samples

the data, but the results in Fig. 1.38 indicate some specific types of behavior. The low levels of spin densities in the Suprasil samples is due to the low flux of high energy radiation (γ-rays or fast n), as expected. The spin density versus dose for Suprasil I and Suprasil W1 is roughly a linear function, and this is the first data discussed thus far which demonstrates a consistent difference in the paramagnetic spin densities of Suprasil I and Suprasil W1.

The relatively high spin densities in Bk7 in Fig. 1.38 are probably due to a combination of electronic ionizations associated with γ radiation and the energetic charged particles produced by the B^{10} nuclear reaction. The fast neutron flux in the thermal column may contribute to the damage processes in the Bk7 glass, but from the spin density associated with 14.8 MeV neutron irradiation, it appears likely that fast neutrons cannot be responsible for the large differences in spin densities between Bk7 glass and the Suprasils in Fig. 1.36. The gamma ray flux in the thermal column is of sufficient intensity to be responsible for a large part of the spin densities in Bk7. But, from the nature of the B^{10} nuclear reaction, it is clear that the energetic Li and α particles will contribute to the radiation damage. Some clues to the relative importance of gamma rays and nuclear reactions in Bk7 radiation damage will be obtained from the EPR spectral data to be discussed below.

5. Reactor Core

The E-1 irradiation facility of the LPTR reactor core has the most complicated and intense radiation flux of any of the sources used in the present experiments. The reactor core has a fast neutron flux (E >.1 MeV) of about 10^{13} n/cm^2·s, a thermal neutron flux of about $2 \cdot 10^{13}$ n/cm^2·s and a gamma ray dose rate of about $2 \cdot 10^8$ rads/hour. Radiation damage in the reactor core will obviously have significant contributions from all of the mechanisms which have been discussed above:

the fast neutrons will create atomic displacements and ionize electrons, the gamma rays will lead to intense levels of electron ionization, and the thermal neutrons will induce nuclear reactions at the B^{10} sites in Bk7 glass.

The results of the absolute spin density measurements on Suprasil I, Suprasil W1 and Bk7 glass samples exposed to the reactor core radiation flux are shown in Fig. 1.39. Since there are a number of different basic mechanisms leading to radiation damage in each of the samples, it is difficult to interpret this data in terms of the individual radiation damage mechanisms. For the four different exposures used, the spin density versus dose is seen to be a roughly linear function. The spin densities observed in Bk7 glass are similar to the high levels observed with Co^{60} gamma ray and thermal column neutron irradiations. But the spin densities in the Suprasil samples at high doses are at least ten times greater than the values observed in the previously discussed data. The relative values of the spin densities between the samples change from a difference of a factor of 10^2 between Bk7 and Suprasil W1 at a dose of about $2 \cdot 10^{15}$ fast n/cm^2 to a difference of only a factor of three at a dose of about 10^{18} fast n/cm^2. In fact, the spin densities in the different glasses seem to be approaching a common value at high doses. Whether or not the spin densities actually saturate at the same value can only be determined by further measurements with higher reactor core radiation doses.

C. EPR Spectra

1. Introduction

This section describes the use made in the present experiments of EPR spectra to investigate the nature of radiation damage. EPR spectra provide a useful source of information which is complementary to the spin density measurements discussed in the previous section. Spin densities specify the number of paramagnetic spins associated with a particular EPR

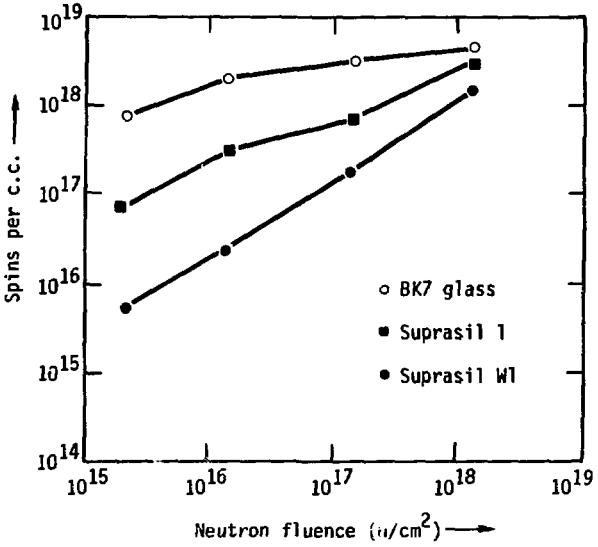

Figure 1.39 Spin Densities in Reactor Core Irradiated Samples

spectrum, but the spectral features of an EPR spectrum are determined by the microscopic nature of the associated paramagnetic centers. The amount of information which can be obtained from a particular EPR spectrum and the techniques which can be used to extract that information depend on the nature of the particular system. The features of the discussion of the data in this section reflect the advantages and disadvantages associated with different types of systems.

There are two basically different types of systems which are discussed in this section. The spectra of E' centers in the Suprasil samples form an ideal system for study and a number of different techniques have been used to interpret the spectral data. The other system, paramagnetic centers in Bk7 glass, form an immensely complicated system and the techniques which can be used to interpret these spectra are severely restricted. For the E' center spectra, the lineshapes and linewidths, and changes in the lineshapes and linewidths with changes in experimental conditions have been used to investigate the nature of radiation damage in the Suprasils. However, in Bk7, interpretation of the EPR spectra has been largely limited to an investigation of the significance of the presence of a narrow spectral feature with a g-value of 2.0009 after irradiation by fast neutrons.

The discussion of the data in this section is again organized on the basis of the different sources used for sample irradiation. In addition, because of the large differences in their EPR characteristics, the discussions of the Suprasil spectral data and the Bk7 spectral data have been separated much more than they were for discussion of the spin density data. But, as in the previous section, the organization of the discussion has been left somewhat loosely defined in order that a variety of considerations can be included as they apply to the discussion.

2. Co^{60} Irradiation

a) Suprasil Samples

A wide variety of EPR spectra due to radiation induced defects have been observed in different forms of SiO_2.[9,16,22,45,52] For crystalline and glassy forms of SiO_2 which are relatively free from multivalent impurities, the EPR spectra have been characterized by narrow linewidths, g-values near the free electron g-value $g_e = 2.0023$ and long relaxation times ($T_1 \simeq 0.25$ m sec).[40] In α-quartz there have been two centers (E_1' and E_2') which have been specifically identified with the g-value tensors in Table 1.1. A detailed study of the E_1' spectra in α-quartz has concluded[16] that this center is associated with the electron occupation of an sp^3 hybrid orbital at an incompletely bonded silicon atom.

In the glassy forms of SiO_2, an asymmetric lineshape similar to the powder lineshape in Fig. 1.7 with a magnetic field width $\Delta H \simeq 2$ Gauss and a zero crossing g-value of about $g = 2.0005$ has been called the E' lineshape.[22,40] Much of the analysis of the E' spectra in fused silica has relied on the assumption that the paramagnetic defects responsible for the E' spectra in fused silica have the same microscopic structure as the E_1' and E_2' defects in α-quartz. This assumption is supported by several experimental results. First, computation of a powder lineshape assuming axial symmetry and using for $g_{||}$ and $g_\perp$ the extreme g-tensor values for the E_1' center in α-quartz in Table 1.1 often results in an excellent approximation to experimentally observed lineshapes.[53,54] Secondly, correlations of the ultraviolet absorption spectra of E' centers in α-quartz with those of fused silica suggest that defects with similar structures exist in both materials. And finally, a detailed analysis of the hyperfine structure of the E' spectra in a Si^{29} enriched fused silica has determined[52] that the associated paramagnetic defect has a structure which is consistent with the E_1' structure in α-quartz.

	E_1'	E_2'	E'
	$g1$, $g2$, $g3$	$g1$, $g2$, $g3$	$g_{\parallel}$, $g_{\perp}$
present work			2.0003, 2.0017 and 2.0003, 2.0017 + 2.0020
Siqel, et. al.[45]			2.0003, 2.0017
Silsbee[16]	2.00176, 2.00049, 2,00029		
Weeks and Nelson[22]	2.0018 2.0006, 2.0003	2.0020, 2.0007 + 2.0009 2.0003	

Table 1.1 Summary of Measured g-values Associated with E' Centers

Here, the g-values of E_1' and E_2' centers were measured in crystalline quartz. The E' g-values are the principal values of the powder lineshape of E' centers in fused silica, assuming axial symmetry for the g-tensor.

The E' spectra measured in Suprasil I and Suprasil W1 due to Co^{60} radiation and shown in Figs. 1.11 and 1.19 show small but interesting differences from previously published spectra. The Suprasil I spectrum is characterized by g-values which are consistent with previous measurements, but the lineshape is distinctly different. In addition, the spectrum of Fig. 1.11 cannot be accurately modeled by a straightforward calculation of the powder lineshape associated with the g-tensors in Table I or by assuming axial symmetry in the system and using the appropriate g-values.[53]

Although the major features of the Suprasil W1 E' spectrum due to Co^{60} radiation (see Fig. 1.19) are the same as the corresponding Suprasil I there is one interesting difference, viz. a slight peak at a g-value of 2.0020. The intensity of this peak is too low to be able to make any careful studies of it; but its presence suggests that there may be a paramagnetic center in Suprasil W1 which is different from the paramagnetic centers associated with the E' spectrum in Suprasil I. This is another piece of data which suggests that there are fundamental differences in the radiation damage behavior of Suprasil I and Suprasil W1.

b) Bk7 Samples

The EPR spectrum of Co^{60} γ-ray irradiated Bk7 (see Fig 1.28) has a broad asymmetric lineshape whose spectral features appear to be independent of the γ-ray dose. The overall spectrum is presumably the sum of contributions associated with several different electron traps at multivalent sites in the material. A detailed analysis of this spectrum is beyond the scope of the present experiments. However, the differences in this spectrum and those produced when Bk7 is exposed to 14 MeV neutrons lead to a number of conjectures concerning radiation damage in Bk7 glass and will be discussed below.

3. 14 MeV Neutrons

a) Suprasil samples

Comparison of the EPR spectra in the Suprasil and Bk7 samples resulting from 14.8 MeV neutron and Co^{60} γ-ray irradiations has provided some of the most interesting results in the present experiments. There are several major differences in the EPR spectra of samples exposed to these two different radiation sources, and the spectral differences reflect differences in the radiation damage mechanisms associated with the two different types of radiation.

Figure 1.12 shows the E' spectrum in Suprasil I resulting from exposure to 14.8 MeV neutrons. This spectrum differs from the spectrum of Suprasil I exposed to Co^{60} γ-rays by the presence of a weak peak in the spectrum with a g-value of 2.0020. Further examination of the data reveals that the E' spectrum in Suprasil I exposed to 14.8 MeV neutron radiation is nearly identical to the E' spectrum in Suprasil WI due to Co^{60} γ-ray radiation, with both having a weak peak with a g-value of 2.0020.

The EPR spectrum of radiation induced defects in Suprasil WI exposed to 14.8 MeV neutrons clearly establishes the existence of a spectral peak with g = 2.0020. Figure 1.20 shows this, where the "normal" E' peak at g = 2.0017 is accompanied by a peak of equal amplitude at g = 2.0020. This spectrum indicates that there are at least two different kinds of paramagnetic centers in the glass structure; but the overall EPR characteristics of these centers suggests that they may be due to structurally similar defects. The g-value tensors of both centers are very similar and differ only by the peaks at g = 2.0017 and 2.0020. The relaxation characteristics of both peaks have been measured and found to be identical, within experimental accuracy - implying that both centers have the same relaxation times T_1 and T_2.

Identification of the defects associated with the spectrum in Fig. 1.20 is a difficult task. A detailed analysis to determine the nature of the electronic wave functions is a task which is well beyond the scope of the present work and is also one which does not necessarily have a unique solution.[25] If the spectrum in Fig. 1.20 is interpreted in terms of the E_1' and E_2' centers in α-quartz, then the peaks with g = 2.0017 and g = 2.0020 can be associated with the E_1' and E_2' centers, respectively.[22] While this association cannot constitute a definite identification, because other measurements (such as optical absorption spectra) are needed to more clearly identify the nature of these centers, the association with E_1' and E_2' centers is certainly consistent with the experimental results. For the convenience of the remainder of this thesis, the spectral features with g = 2.0017 and g = 2.0020 will tentatively be associated with the E_1' and E_2' centers, respectively.

The EPR spectra of Suprasil Wl samples show that the E_2' peak is nearly absent for γ-ray irradiation, but has a large amplitude for 14.8 MeV neutron irradiation. This association with fast neutrons suggests that the E_2' center occurs in Suprasil Wl as a result of atomic displacement collisions. This interpretation is also consistent with the small E_2' peak in the Co^{60} irradiation EPR spectrum of Suprasil Wl, because Co^{60} γ-rays can be expected to result in atomic displacement events (with densities about ten times less than the total spin density associated with Fig. 1.19). It is not particularly surprising that there is a specific type of defect associated with atomic displacement events in Suprasil Wl, but it is surprising that Suprasil I exhibits such different behavior from Suprasil Wl. And further, if the E_2' spectrum is associated with displacement damage mechanisms, the different behaviors of Suprasil I and Suprasil Wl implies that there are

significant atomic structural differences between the two glasses. If the two glasses were essentially identical with respect to their atomic structure, then atomic displacement events would be expected to lead to similar defects in both materials.

Since the starting material used to fabricate Suprasils ($SiCl_4$) is always the same, the different radiation damage behaviors of Suprasil I and Suprasil W1 must be due to differences in the glasses resulting from the different techniques used to fabricate them. The detailed differences in atomic structure between Suprasil I and Suprasil W1 are not well understood; but, chemically, Suprasil W1 has a higher Cl content (200 ppm vs. 100 ppm) and a much lower OH content (5 ppm vs. 1200 ppm) than Suprasil I. The large difference in OH content of the two glasses may be an important factor in their different radiation damage behavior, but it isn't possible to determine the details of the relationship between OH content and radiation damage behavior on the basis of the presently available data.

b) Bk7 Samples

Spectra of Bk7 samples irradiated with Co^{60} γ-rays and 14.8 MeV neutrons also show interesting differences. While the overall character of the broad asymmetric lines due to γ-ray irradiation (see Fig. 1.28) and fast neutron irradiations (see Fig. 1.29) are roughly similar, the narrow spectral "spike" with a g-value of about 2.0009 is a major distinction between them. This difference has a qualitative similarity to the different radiation damage behaviors in Suprasil samples discussed above.

The overall EPR behavior of the g = 2.009 spike in the Bk7 spectrum implies that it is due to the presence of the E' center in Bk7 glass. The signal saturates with microwave powers above $\approx$2 μW and the g-value and linewidth are all consistent with the EPR characteristics of the E' center. Because it occurs with relatively low spin densities (roughly 10% of total

for 14.8 MeV neutron irradiation) and because it occurs on the "tail" of the broad, asymmetric Bk7 EPR lineshape, it is very difficult to accurately measure the EPR characteristics of the "E'" spike.

The interpretation of the spectral spike in terms of E' spectra is also subject to some doubt because we have noted that bombardment by H^+ or He^+ ions results in EPR spectra which are qualitatively similar to the E' spectra. These spectra may be due to paramagnetic ions created by these bombardments, or may be due to some new type of defect in the glass structure. Recognizing these other possibilities, it is still convenient to interpret the g = 2.0009 spectral spike in terms of the possible presence of E' centers in Bk7 glass.

The presence of E' centers in multicomponent glasses would not be a new result because they have been reported in a number of other multicomponent silicate glasses.[27,55] One of these[27] reports behavior similar to that in the present experiments where the E' spectrum is observed in response to fast neutron irradiation, but not with γ-ray radiation.[55] But the lack of complete specification of important experimental variables, such as sample composition, makes it difficult to compare these results with the results of the present experiments, and the complicated nature of these materials also makes it difficult to draw unambiguous conclusions.

It is interesting to speculate on the mechanisms responsible for the radiation damage behavior observed in Bk7 glass in the present experiments. The E' spectra occur in Bk7 in response to 14.8 MeV neutron irradiation, but not in response to Co^{60} γ-ray irradiation; so it appears that this feature is associated with atomic displacement events in the glass structure. Now, E' centers have been associated with the electron occupation of an incompletely bonded silicon sp^3 hybrid orbital.[16] And it is also known that, because of its high alkali content, the Bk7 glass has an excess

of oxygen available to its atomic structural network.[18] If the excess oxygen in the glass structure tends to saturate silicon bonding orbitals, and if the E' center is indeed the electron occupation of an incompletely bonded silicon atom, then it is easy to understand how the presence of an E' center is associated with atomic displacement events. This is because, in order to have an incompletely bonded silicon in Bk7 glass (and, thus, an E' center), it is necessary to create one by displacing an oxygen atom from a silicon-oxygen bonding position. Thus, in this situation, 14.8 MeV neutrons would be expected to result in the presence of E' centers, while Co^{60} γ-rays would not.

If it is correct, the interpretation of the occurrence of E' centers in Bk7 glass in terms of excess oxygen and incompletely bonded silicon in the material would be an interesting result. This result would further the identification of the E' center with incompletely bonded silicon atoms and would also establish a procedure which could be used to estimate the density of incompletely bonded silicon atoms in a glass. If the above interpretation is correct, a measurement of E' spin densities resulting from Co^{60} irradiation of glasses may be used to estimate the density of incompletely bonded silicons in the glass. There is presently no well-defined way to determine the density of incompletely bonded silicons in silicate materials, and because of its relation to physical properties of a material, it would be an extremely useful number to know.

4. Thermal neutrons

The EPR spectra of Suprasil and Bk7 samples exposed to the LPTR thermal column radiation flux showed no new features that had not already been detected in response to 14.8 MeV neutron and Co^{60} γ-ray irradiations. The spectra resulting from thermal column irradiations were consistent with the spectra which would have been expected on the basis of the 14.8 MeV neutron and Co^{60} γ-ray experiments.

The EPR spectra of Suprasil samples irradiated in the thermal column were essentially the same lineshapes which had been observed in response to Co^{60} irradiations. This is exactly what would be expected for thermal column irradiations because the low energy neutron flux in the thermal column should be ineffective for inducing damage in the glass through atomic displacements, but the gamma ray flux (with median γ-ray energy $\approx$ 0.7 MeV) should be capable of inducing damage similar to that associated with Co^{60} γ-ray irradiation.

The EPR spectra of Bk7 glass irradiated in the thermal column (see Fig. 1.31) were also consistent with those expected on the basis of EPR spectra associated with Co^{60} γ-ray and 14.8 MeV neutron irradiations. This is an interesting result because a significant portion of the radiation damage in Bk7 samples irradiated in the thermal column is due to charged particles created by $^{10}B(n,\alpha)^{7}Li$ nuclear reactions. The γ-ray flux in the thermal column is probably responsible for a large portion of the high total spin densities in Bk7. But the spectrum of Fig. 1.31 also exhibits the g = 2.0009 E' spike which has been associated above with displacement damage in the glass. This feature does not occur with Co^{60} γ-ray irradiation, as it is unlikely that the thermal column γ-ray flux can be responsible for its presence. And it is also unlikely that the low energy neutron flux of the thermal column can induce atomic displacements through elastic collisions. The only probable source of radiation which can induce atomic displacements in the glass is the energetic α and Li particles created by the B^{10} nuclear reaction (see eq. (1.4)). Thus, the EPR spectrum of Bk7 irradiated in the thermal column reflects the combination of electron ionization events by gamma rays and atomic displacement events by α particle and Li ions in the glass structure. It is interesting that although the fundamental radiation damage processes are different, the EPR spectra of Bk7 irradiated by 14,8 MeV neutrons and the thermal

column radiation are roughly the same. This is an example of where the presence of similar E' spectra for two different experimental situations does not necessarily imply that the same radiation damage mechanism occurs in both situations.

5. Reactor Core Irradiations

The EPR spectra of samples irradiated in the LPTR reactor core reflect the fact that radiation damage due to exposure to the reactor core has contributions from all of the different damage mechanisms which have been discussed above. The reactor γ-ray flux leads to electronic ionization via the Compton effect and results in normal E' spectra in Suprasil samples and in the broad asymmetric lineshape in Bk7 samples. The fast neutron flux results in atomic displacement events through elastic collisions, leading to the E_2' spike in Suprasil W1 and the E' spike in Bk7 samples. The thermal neutron flux leads to the B^{10} nuclear reaction in Bk7 glass and contributes to the E' spike in the corresponding EPR spectra. The EPR spectra of the reactor core irradiated samples showed no previously undetected features and were consistent with the spectra expected on the basis of the EPR spectra resulting from exposure to the other types of radiation sources.

The EPR spectrum of Suprasil I sample #642 which was exposed to about 10^{18} n/cm^2 in the reactor core was a particularly important piece of data. The E' spectrum of this sample is shown in Fig. 1.13, where it can be seen that the lineshape is substantially different from the other E' lineshapes which have been discussed above. The g-values of the major features of this spectrum are the ones normally associated with E', but the spectral width of the component peaks of this spectrum are broadened, resulting in a qualitatively different lineshape. There are a number of mechanisms which could cause this broadening, but the high spin density in this sample ($\sim 3.6 \cdot 10^{18}$ spins/c.c.) makes it likely that the broadening is due to

dipole-dipole interactions between neighboring paramagnetic spins in the sample. Since the dipole-dipole interaction between like spins is a homogeneous broadening mechanism, the spectrum in Fig. 1.13 exhibits homogeneous broadening which is the same order of magnitude as the inhomogeneous broadening normally associated with the anisotropic g-tensor of the E' center. Thus, Fig. 1.13 represents an E' spectrum for which a dominant broadening mechanism is homogeneous.

When dipole-dipole broadening is due to high densities of randomly distributed paramagnetic spins in a solid, the analysis of Kittel and Abrahams[32,56] can be used to relate the magnitude of homogeneous broadening and the average spin density:

$$\Delta H = 5.3\ g\beta N\ . \qquad (1.106)$$

Here, N is the total paramagnetic spin density and ΔH is the full magnetic field width associated with dipole-dipole broadening. For sample #642 with $N = 3.6 \cdot 10^{18}$ spins/c.c., eq. (1.106) specifies a full width due to dipole broadening of

$$\Delta H \approx 0.7G \qquad (1.107)$$

This result is in excellent agreement with the qualitative broadening which is evident in the spectrum of Fig. 1.13. Thus, the spectral broadening expected from dipole-dipole interactions at high paramagnetic spin densities is consistent with the corresponding EPR spectrum. This is one example of a situation where two different kinds of measurements have demonstrated the self-consistency of our data. In this case, the results of absolute spin density measurements have been found to be consistent with changes in the associated EPR spectra.

The agreement of eq. (1.107) with the observed spectral broadening can be used to further characterize the nature of radiation damage in the Suprasil I sample. The result of eq. (1.107) demonstrates that dipole-dipole

broadening is observed in a situation which is consistent with the assumption of randomly distributed paramagnetic spins. If the paramagnetic spins were not randomly distributed, but existed in "clusters" of defects, then a much larger degree of broadening would have been observed for sample #642. Or, conversely, clusters of defects would lead to the observation of dipole-dipole broadening with much lower spin densities than than in sample #642. One of the most striking features of the E' spectra of Suprasil I samples in these experiments has been the nearly complete uniformity of the spectra for different radiation sources and doses. In view of these uniform spectra, the observation of spectral broadening which is consistent with the presence of a random distribution of spins in the sample strongly suggests that radiation induced defects occur in the sample in a random distribution.

The presence of a random distribution of radiation induced paramagnetic defects is a significant result with respect to radiation damage. For gamma ray and fast neutron irradiation of a material, the radiation damage mechanisms are initiated at random locations in the material structure. For fast charged particle bombardment or fast ions created by γ-ray or fast neutron irradiation, most radiation damage effects are expected to occur at or near the end of the particle path. Thus, it is generally expected that damage associated with charged particles will exist in groups or clusters near the end of charged particle paths, rather than being randomly distributed over the particle trajectory. The presence of a random distribution of radiation induced defects implies that there is nothing intrinsic in the nature of the glass structure which results in clusters of paramagnetic defects, and that, for the radiations used here, the damage events are not dominated by processes which lead to clusters of defects in the material.

Since it is the dominant homogeneous broadening mechanism, the dipole broadening in sample #642 can also be used to determine the transverse

relaxation time T_2 associated with this system. Using eq. (1.64) and the result of eqs. (1.53) and (1.107) we can estimate the T_2 of this system:

$$T_2 \approx 2.3 \cdot 10^{-7} \text{ sec} \tag{1.108}$$

The present data has demonstrated that dipole-dipole broadening is the dominant homogeneous broadening mechanism of this system. Dipole-dipole broadening is probably also the dominant homogeneous broadening mechanism for other irradiated samples where the spin density is lower and the associated homogeneous broadening cannot be resolved from the E' spectrum. For example, for sample #060 exposed to Co^{60} γ-rays and with an E' spin density N of about $1.5 \cdot 10^{17}$ spins/c.c., we obtain:

$$\Delta H \approx 0.03 \text{ G} \tag{1.109}$$

$$T_2 \approx 3.8 \cdot 10^{-6} \text{ sec} \tag{1.110}$$

0.03G is clearly much too small a level of broadening to be readily resolved from the E' spectrum but it may still be the dominant homogeneous broadening mechanism in the sample. Unfortunately it is difficult to determine for what spin densities dipole-dipole interactions are the dominant homogeneous broadening mechanism when the dipole broadening cannot be spectrally observed. However, for systems for which detailed studies of the power saturation can be used to determine both T_1 and T_2, comparison of the power saturation determined T_2's and the "dipole broadening" T_2's will be a useful correlation. In the discussion below, this correlation is discussed for samples #642 and #060.

D. Saturation Behavior

1. Introduction

This portion of the discussion of the data describes the use of continuous wave power saturation of EPR signals to investigate radiation induced paramagnetic centers. Power saturation data can be used in a variety of ways. Since different paramagnetic centers saturate differently,

power saturation data may sometimes be used to establish that more than one type of paramagnetic center is contributing to a given EPR spectrum. Portions of the EPR theory section above described the manner in which measurement of the saturation of the susceptibility $\chi''(\omega)$ associated with a particular paramagnetic system can be used to determine the relaxation time product T_1T_2, and also described how spectral measurements of saturation broadening of an EPR spectrum can be used to determine the longitudinal relaxation time T_2. These results provide unique, specific information about the EPR systems of interest. In addition, since spin density and unsaturated spectral broadening measurements can sometimes be used to determine the T_2 of a system, saturation measurements can serve as an independent verification of these other techniques.

Power saturation techniques can be applied to any system of paramagnetic centers. The major experimental requirement for these experiments is that sufficient microwave power be available to saturate the appropriate signals. For many of the samples in the present experiments it was possible to easily saturate the EPR signals, but for other samples it was not possible to do so at all. For example, the broad asymmetric lineshape associated with Co^{60} γ-ray irradiated Bk7 glass (Fig. 1.28) could not be saturated with the available microwave power (~250 mW). However, as has been discussed above, the narrow spike with g = 2.009 for the Bk7 samples exposed to fast neutrons could be very easily saturated. The saturation behavior of this feature distinguished it from the remainder of the Bk7 spectrum and encouraged its identification as a signal due to the presence of E'-type centers in the glass.

In contrast to the Bk7 samples, the E' spectra of the different Suprasil samples provided an ideal system to investigate with power saturation techniques. The unusually long relaxation times associated with E' centers and the relatively narrow inhomogeneous linewidths made it possible to use both saturation of the EPR signal amplitude and saturation broadening

of the E' spectra to investigate these systems. The combination of both of these measurements made it possible to determine both T_1 and T_2. And the results for T_2 could, in turn, be compared with the values which were estimated from spectral broadening measurements and from estimates of dipole-dipole broadening.

The discussion of saturation measurements will be centered around the results obtained for two different samples. Suprasil sample #060 was exposed to Co^{60} γ-rays and had a total spin density of about $1.5 \cdot 10^{17}$ spins/c.c. Suprasil sample #642 was irradiated in the LPTR reactor core and had a total spin density of about $3.6 \cdot 10^{18}$ spins/c.c. As with the E' spectra of different samples, one of the most striking aspects of the saturation data was the similar behavior exhibited by most of the samples. For most samples, the amplitude of the susceptibility $\chi''(\omega)$ could be saturated by a factor of two with microwave magnetic fields as small as 5 mG. The major exception to this uniform behavior was the saturation behavior of sample #642, which required microwave magnetic fields as large as 50 mG to saturate $\chi''(\omega)$ to one half of its unsaturated value. Thus, although the discussion only includes two main samples, the behavior of most of the Suprasil samples can be represented by the behavior of samples #060 and #642.

2. Signal Saturation

The saturation of an EPR signal can be used to characterize the saturation of the associated susceptibility $\chi''(\omega)$ as a function of microwave power. And the saturation of the amplitude of $\chi''(\omega)$ of a paramagnetic system can be used to determine the relaxation time product T_1T_2 of that system. In the EPR theory section above it has been shown that the power saturation of the amplitude of $\chi''(\omega)$ can be described in terms of a function of the form $(1 + S)^{\alpha}$, where

$$S = \gamma^2 H_1^2 T_1 T_2 \ . \qquad (1.49)$$

For homogeneous systems, $\alpha = -1$ and the amplitude of $\chi''(\omega)$ is proportional to:

$$\chi''(\omega) \propto \frac{1}{1+S} \tag{1.111}$$

For perfectly inhomogeneous systems (where $T_2^* \ll T_2$) $\alpha = -1/2$ and $\chi''(\omega)$ has an amplitude proportional to:

$$\chi''(\omega) \propto \frac{1}{\sqrt{1+S}} \tag{1.112}$$

For systems which are only mildly inhomogeneous ($T_2^* \lesssim T_2$), and when the precise nature or the inhomogeneous broadening is not specified, we have

$$-\frac{1}{2} \geq \alpha > -1 \ . \tag{1.113}$$

where α is determined by the specific situation; and the amplitude of $\chi''(\omega)$ has the proportionality:

$$\chi''(\omega) \propto (1+S)^{\alpha} \tag{1.114}$$

Equations (1.111) through (1.114) can be used to help interpret the signal saturation data in terms of the relaxation times of the EPR system. Fig. 1.40 shows the measured saturation of the amplitude of $\chi''(\omega)$ as a function of applied microwave field. The microwave field for which $\chi''(\omega)$ is reduced to half of its unsaturated amplitude can be used with eqs. (1.111) through (1.114) to determine the product T_1T_2.

For sample #060, it is seen that $\chi''(\omega)$ is saturated by a factor of two when $H_1 \approx 50$ mG. Since the dipole-dipole broadening estimate for this sample suggests homogeneous spin packet widths of about 30 mG, it is probably an excellent approximation to assume that this system is perfectly inhomogeneous. Thus, eq. (1.112) and Fig. 1.40 yield:

$$\frac{1}{2} = \frac{1}{\sqrt{1+S^2}} \tag{1.115}$$

Therefore:

$$S^2 = 3 \tag{1.116}$$

and:

$$T_1T_2 = \frac{3}{\gamma^2 H_1^2} = 3.9 \cdot 10^{-10} \text{ sec}^2 \tag{1.117}$$

The data in Fig. 1.40 shows that $\chi''(\omega)$ is much more difficult to saturate for sample #642 than for #060. For sample #642, $\chi''(\omega)$ is saturated by a factor of two for a microwave magnetic field amplitude $H_1 = 50$ mG. Since the homogeneous dipole-dipole broadening in sample #642 results in spin packets which are nearly as broad as the entire inhomogeneous linewidth, this system is neither homogeneous or extremely inhomogeneous. As an approximate description of this situation, we choose $\alpha = -3/4$ to describe the saturation behavior. We now have that when $\chi''(\omega)$ is saturated to one-half its unsaturated amplitude:

$$\frac{1}{2} = \frac{1}{(1 + S)^{3/4}} \tag{1.118}$$

or:

$$S \approx 1.52 \tag{1.119}$$

and:

$$T_1T_2 \approx \frac{1.5}{\gamma^2 H_1^2} \approx 2 \cdot 10^{-12} \text{ sec}^2 \tag{1.120}$$

The product T_1T_2 for sample #642 has been found to be more than two orders of magnitude smaller than the product for sample #060. Since the errors associated with the approximate value of α can be no larger than a factor of two (in the worst possible case), the large difference in T_1T_2 for these two samples clearly reflects major differences between the relaxation times of the two systems.

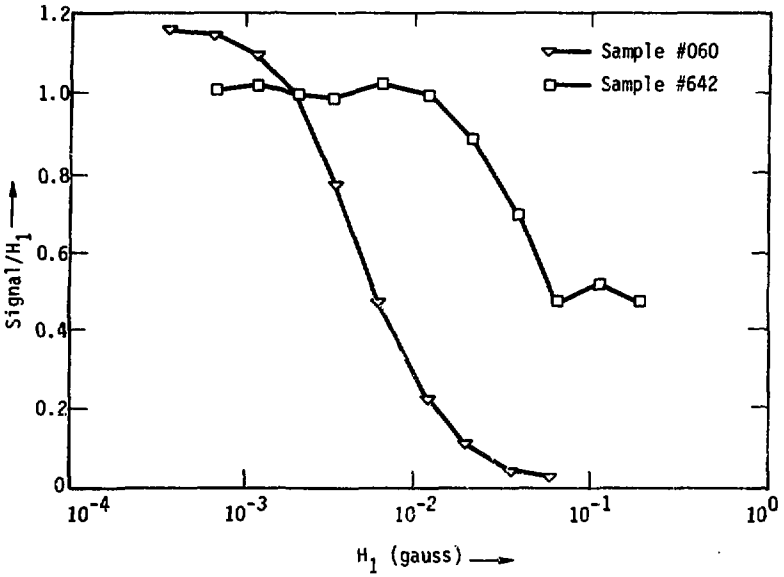

Figure 1.40 Power Saturation of $\chi''(\omega)$ for E' Centers

This figure displays two different saturation curves for E' spectra. Sample #060 was irradiated by Co^{60} γ-rays and has a spin density of about $1.5 \cdot 10^{17}$ spins/c.c. Sample #642 was irradiated in the reactor and has a spin density of about $3.6 \cdot 10^{18}$ spins/c.c.

3. Saturation Broadening

Saturation broadening was the second method used to investigate the relaxation times of the E' centers in Suprasil samples. The long relaxation times together with the narrow overall inhomogeneous linewidth of E' centers in Suprasil make them an ideal system for this type of study. The basis of saturation broadening is eq. (1.70) where is is shown that the spectral width $\Delta\omega_{sp}$ of a single spin packet is given by the relation:

$$\Delta\omega_{sp} = \frac{2\sqrt{1 + S}}{T_2} \quad . \tag{1.70}$$

Since this result applies only to a single spin packet, it is not affected by inhomogeneous collections of spin systems. We see here that saturation broadening provides a homogeneous mechanism whereby the width of a spin packet can be externally broadened and controlled. In the present experiments, microwave power to the system was increased until the spectral width of a spin packet was nearly the same as the inhomogeneous width of the E' lineshape. When the spin packet width can be resolved from the E' spectrum, $\Delta H \approx 0.7G$ and we have:

$$\Delta\omega = \gamma\Delta H \approx 1.23 \cdot 10^7 \tag{1.121}$$

Using this width together with eq. (1.70) and experimentally determined values of S (from amplitude saturation of $\chi''(\omega)$) it is possible to determine the relaxation time T_2.

For sample #060, it was found that when the spin packets were broadened to the point defined by eq. (1.121), the microwave power to the system corresponded to a saturation parameter of $S \approx 1505$. Thus, from eq. (1.70) we have:

$$T_2 = \frac{78}{1.23 \cdot 10^7} = 6.3 \cdot 10^{-6} \text{ sec.} \tag{1.122}$$

Using this vaule for T_2, together with the T_1T_2 product (eq. 1.117) for this sample, T_1 can be obtained as:

$$T_1 = 6.2 \cdot 10^{-5} \text{ sec.} \tag{1.123}$$

For sample #642, amplitude saturation of $\chi''(\omega)$ and saturation broadening occurred at the same microwave powers. The saturation broadening could be resolved from the E' lineshape because the dipole-dipole broadening in this sample had already broadened the spin packets so that they could be resolved from the E' lineshape. Thus, from eqs. (1.70) and (1.121) when S = 1.52, we have:

$$\Delta\omega = \frac{2\sqrt{2.52}}{T_2} \quad , \tag{1.124}$$

or:

$$T_2 = 2.6 \cdot 10^{-7} \text{ sec.} \tag{1.125}$$

And, once again, using the T_1T_2 product determined for this sample in eq. (1.120) we obtain:

$$T_1 = 7.7 \cdot 10^{-6} \text{ sec.} \tag{1.126}$$

These results and some previously reported results are summarized in Table 1.2. As far as the present data is concerned, the agreement between the T_2's determined by dipole-dipole broadening estimations from spin densities, spectral broadening, and power saturation demonstrates the internal self-consistency of the data. The T_2's determined by these different techniques are all within a factor of two of each other. Considering the complicated and poorly understood nature of these systems, this agreement between the data is very satisfactory. While there are errors of about a factor of two in the results, the data for samples #060 and #642 have shown differences of orders of magnitude in the relaxation times associated with the two samples. These results serve as a quantitative indication of the distinct

	Spin Density	E'	
		T_1	T_2
present work	$1.5 \cdot 10^{17}$ spins/c.c.	62 μsec	6.3 μsec
	$3.6 \cdot 10^{18}$ spins/c.c.	7.7 μsec	0.26 μsec
Castle, et. al.[40a]	-	~250 μsec	-
Castle, et. al.[40b]	$3.4 \cdot 10^{18}$ spins/c.c., $1 \cdot 10^{17}$ spins/c.c.	~250 μsec	-
Bozanic, et. al.[57]	$\sim 3 \cdot 10^{16}$ spins/c.c.	200 μsec	40 μsec

Table 1.2 Room Temperature Relaxation Times Measured for E' Centers

behavior shown by these two samples. Once again, for the vast majority of Suprasil samples in these experiments, an outstanding characteristic of their EPR behavior was the uniform spectral features and saturation characteristics for different samples. The heavily irradiated sample #642 showed major deviations from this uniform behavior and the results of eqs. (1.117) and (1.120) serve to specify the nature and extent of the observed differences.

The results summarized in Table 1.2show that there are differences in the relaxation time T_1 for our measurements and for the measurements of Castle[40] and Bozanic.[57] Bozanic's sample had a spin density of about $3 \cdot 10^{16}$ spins/cm^3. His measured T_2 is consistent with dipole-dipole broadening in the sample and, therefore, is consistent with our results. But he also measures a room temperature T_1 of about 0.2 msec, which is very different from our results of about .06 msec and .008 msec. However, if T_1 is dependent on concentration, extrapolation of our measured T_1's to a sample with about $3 \cdot 10^{16}$ spins/cm^3 would reveal a result fairly near 0.2 msec. However, Castle, et al.,[40] found that T_1 did not depend on spin density for samples with about $1 \cdot 10^{17}$ spins/c.c. and $3.4 \cdot 10^{18}$ spins/c.c. However, they do not report the presence of any spectral differences for these two samples, while we have shown above that spin densities as high as $3 \cdot 10^{18}$ spins/c.c. should lead to easily detectable changes in the E' lineshape. Thus, we suspect that either the spin density measurements were incorrectly performed, that spectral measurements were incorrectly performed, or that the spectra were not E' spectra, but were EPR spectra characteristic of the particular glasses and associated impurities.

The discussion of E' power saturation behavior has carefully avoided the mention of distinctions between the saturation behavior of the E_1' and E_2' spectra which have been observed in some of the samples. Suprasil W1 samples irradiated by 14.8 MeV neutrons with equal intensity E_1' and

E_2' "peaks" provided an excellent opportunity to isolate differences between the saturation behavior of these two features. However, within the limits of experimental accuracy, the saturation behavior of the E_1' and E_2' features was identical. Thus, the relaxation times of the paramagnetic centers associated with the E_1' and E_2' peaks have very similar, if not identical, relaxation times T_1 and T_2. Any differences in the saturation behavior of samples showing significant spectral contributions from the E_2' peak could be explained in terms of the measured spin density in that sample.

E. Microscopic Damage Mechanisms

1. Introduction

The purpose of this final portion of the discussion is to further probe the nature of microscopic radiation damage. There are a number of different microscopic damage mechanisms which have been mentioned in connection with the EPR data above. Gamma rays have been associated with electron ionization events, while fast neutrons have been associated with atomic displacement events. A number of other processes, such as the B^{10} nuclear reaction have also been mentioned. The character of microscopic damage in a material depends on the relative contributions from these different mechanisms, so it is important to understand as well as possible the nature of damage mechanisms which are important for specific experimental conditions.

The discussion below will use the EPR spin density and spectral measurements to characterize microscopic damage for exposure to Co^{60} γ-rays and 14.8 MeV neutrons. The data for γ-ray and fast neutron irradiations will be used because they can be associated with fairly well defined damage mechanisms. The spin densities will be compared to the number of primary collisions expected for the different experimental conditions. These comparisions can be used to characterize damage events in terms of quantities such as the primary knock-on range, the number of paramagnetic centers resulting from a single primary collision and the amount of energy absorbed per paramagnetic

defect. These different characterizations will be related to the behavior which is expected for the specific experimental situations.

2. Co^{60} γ-rays

For Co^{60} γ-rays, the dominant primary scattering mechanism in silicate glasses is the Compton effect, resulting in the production of energetic ionized electrons. Pair production and the photoelectric effect may also occur, but they will not be explicitly considered because they also result in the production of energetic electrons. The average energy transferred to the primary scattered electrons by Co^{60} γ-rays (with energy of about 1 MeV) is about 0.5 MeV. These primary electrons dissipate most of their energy in a cascade of collisions which produce additional ionized electrons. The cascade of electron ionizing collisions will continue until the resulting electrons no longer have sufficient energy to ionize additional electrons.

A very small fraction of the primary electron energy may also be dissipated in elastic collisions with atomic nuclei leading to the production of atomic displacements. For 0.5 MeV electrons in silicate glasses, the maximum energy transferred to atomic nucleii in elastic collisions is about 150 eV,[58] but the average transferred energy is less than 1 eV,[58] so that very few atomic displacements occur. For the samples in the present experiments, the number of atomic displacements by ionized electrons which were expected[48] were always at least ten times less than the observed paramagnetic defect spin densities. The relative absence of atomic displacement events for Co^{60} irradiation was also supported by the differences in E' spectra observed for Co^{60} γ-ray and 14.8 MeV neutron irradiation of Suprasil W1 samples (see Figs. 1.19 and 1.20).

For low dose γ-ray irradiations, the production of ionized electrons results in the occupation of electron and hole traps in the glass microstructure. If these defects in the non-irradiated material are nonparamagnetic, then their occupation by an unpaired electron or hole results in an unpaired

electron spin and a magnetic dipole at the defect. Paramagnetic defect centers formed in this way can often be detected and studied by EPR. EPR spin density measurements performed on these systems are used to determine the densities of specific defects which result from a given type of sample irradiation.

For relatively low radiation doses, the radiation damage spin densities should be a linear function of radiation dose. This is true as long as the total number of ionized electrons is much less than the number of trapping defects in the material. In this case, ionized electrons, most of which were scattered from atomic bonding orbitals in the material, will "see" a relatively large number of available trapping sites, and a relatively low number of unoccupied bonding orbitals. As a result, most of the ionized electrons will occupy defect trapping sites, resulting in a linear relation between defect dose and damage defect density.

For higher radiation doses, when the total number of ionized electrons is roughly equal to the number of trapping sites originally available to the system, the defect density will no longer be a linear function of dose, but will saturate, or approach a maximum with increasing dosage. This is because the ionized electrons will "see" roughly equal numbers of defect trapping sites and unoccupied bonding orbitals in the material and will have roughly equal probability for occupying either of these states. Thus, not all of the ionized electrons will result in defect occupation, but will finally occupy bonding orbitals which were vacated by ionization even's. Thus, when the number of defect sites and unoccupied bonding orbitals available to ionized electrons is equal, the defect density will "saturate" and remain roughly constant with increasing radiation dose.

The Co^{60} γ-ray irradiated Bk7 spin density measurements can be used to illustrate these types of behavior. From Fig. 1.32 we see that for a γ-ray dose of 10^9 rads, the measured spin density is about 10^{18} spins/c.c.

Now, the number of primary Compton collisions N_p expected for this radiation dose is:

$$N_p = \sigma F \quad , \tag{1.127}$$

where

N_e = material electron density

σ = Compton scattering cross section

F = total photon flux

For Bk7 glass, and 10^9 rads of 1 MeV γ's, we have:

$N_e = 1.3 \cdot 10^{-24}$ e$^-$/c.c.

$\sigma = 10^{-25}$ cm^2

$F = 2 \cdot 10^{18}$ photons/cm^2 ,

and:

$$N_p = 2.6 \cdot 10^{17} \text{ e}^-\text{/c.c.} \tag{1.128}$$

Thus, the Bk7 spin density for this dose corresponds to the creation of about 4 paramagnetic spins per primary Compton collision. And, since an average of 0.5 MeV is transferred to the primary scattered electron, the spin density also corresponds to the absorption of about 10^5 eV per paramagnetic spin. 10^5 eV is much more than the tens of electron volts required to ionize an electron and indicates that the Bk7 spin density is highly saturated. The saturated condition of the spin density is also evident in the data of Fig. 1.32, where an increase of three orders of magnitude in the γ-ray dose from 10^6 rads to 10^9 rads only resulted in an increase of a factor of five in the spin density from $2 \cdot 10^{18}$ to 10^{19} spins/c.c..

These results are interesting to compare with the spin density measured in Bk7 glass for an exposure of 10^6 rads of Co^{60} γ-rays. The spin density of $2 \cdot 10^{17}$ spins/c.c. corresponds to the creation of 800 paramagnetic spins per primary Compton collision and the deposition of about 650 eV per spin. Data of this type, if obtained for lower doses could be used to

determine the ionized electron kinetic energy necessary to create paramagnetic centers in the glasses. This number can be determined when γ-ray doses are low enough so that the paramagnetic spin density is a linear function of gamma ray dose.

The spin density behavior of the Co^{60} γ-ray irradiated Suprasil samples in Fig. 1.36 show very different behavior from the Bk7 data. The puzzling spin density behavior of Suprasil I and Suprasil W1 for doses above 10^6 rads is probably partly due to the fact that these doses probably lead to extremely saturated spin density conditions in these glasses. This is because saturation of the spin densities in the Suprasil samples will occur at much lower doses and spin densities than in the Bk7 glass samples. This is due to the fact that, while primary Compton collisions occur at nearly the same rate in all of the glasses, the Suprasil samples (with their low metallic impurity content) have a low density of extrinsic trapping sites, while the Bk7 glass has a high density of extrinsic defects associated with its metallic impurity content. And since the spin density in Bk7 appears to be saturated at exposures of 10^6 rads, then the Suprasil sample spin densities will also be highly saturated. The only impurity common to Suprasil I and W1 is Cl, and it is unlikely that the E' spin densities are associated with an electron or hole trap at a Cl site in the glass. If the E' centers were associated with a trap at a Cl site, the spin density would behave similarly to the densities observed in Bk7 glass—exhibiting high densities for low gamma ray doses. Thus, the confusing aspects of the spin densities observed in the Suprasil samples appear to be a reflection of the complications associated with saturated levels of spin densities in these glasses for doses above 10^6 rads.

3. 14.8 MeV neutrons

Much of the radiation damage resulting from exposure to 14.8 MeV neutrons occurs as a result of mechanisms which are fundamentally

different from the mechanisms associated with Co^{60} γ-rays. There are two energy loss mechanisms for 14.8 MeV neutrons in silicate glasses which are of interest for the present discussion: elastic scattering of atomic nuclei and inelastic scattering of atomic nuclei leading to the emission of γ-rays from excited state nuclear energy levels. There is a variety of other types of collisions which may occur, but the two mechanisms just mentioned account for most of the scattering cross section for fast neutrons in silicate glasses. Both elastic and inelastic neutron scattering events lead to the production of atomic displacements and energetic ions in the glass microstructure. Elastic scattering of Si and O atoms by 14.8 MeV neutrons leads to the production of ions with an average kinetic energy of about 1.5 MeV. As the knock-on ions propagate through the solid, they experience Coulombic collisions with atomic electrons and nuclei. The vast majority (99.97%) of primary Si and O knock-on kinetic energy is absorbed in electron ionizing collisions, with only a small fraction (~0.03%) of the energy being absorbed in atomic displacement events.

At a first glance, it might appear that the microscopic damage associated with fast ions due to 14.8 MeV neutrons is similar to the damage associated with energetic electrons due to 1 MeV γ-rays. Both radiations lead to large amounts of energy absorbed in electron ionization events and both lose a small fraction of deposited energy to atomic displacement events. However, the differences in the energies of the particles produced by these radiations lead to major differences in their radiation damage characteristics. The electrons produced by γ-rays are high energy (~0.5 MeV) electrons which dissipate most of their energy in a cascade of Coulomb collisions leading to the production of additional energetic electrons. But the electrons associated with the fast ions produced by 14.8 MeV neutrons are fairly low energy (10-100 eV) electrons which are incapable of initiating an ionizing collision cascade. On the other hand, atomic

displacements associated with γ-ray irradiation lead to the production of low energy (~1 - 10 eV) ions which are incapable of producing large amounts of additional damage, while the atomic displacements associated with 14.8 MeV neutrons can lead to the production of additional atomic displacements and energetic ions in a cascade-type process.

Thus, while there are major distinctions between microscopic damage process associated with γ-rays and fast neutrons, it is difficult to specify the precise nature of radiation damage due to fast neutrons. Fast neutrons will lead to significant numbers of atomic displacements and electron ionizations. In addition, the γ-rays produced by inelastic scattering of neutrons may lead to large fluxes of energetic electrons in the material microstructure. The relative importance of these different mechanisms will depend strongly on the particular experimental conditions of interest. The EPR data in the present experiments can be used to investigate the relative importance of some of these mechanisms. This has already been done to some extent in previous sections of the discussion of the data, and the discussion below will attempt to use the EPR data to characterize some of the details of microscopic damage events associated with 14.8 MeV neutrons.

Because there are significant contributions from several different microscopic damage mechanisms, it is difficult to perform a detailed theoretical analysis of EPR data for 14.8 MeV neutron irradiated glass samples. But comparison of 14.8 MeV neutron radiation damage data with Co^{60} γ-ray radiation damage data can be used to help identify the nature of the dominant damage mechanisms for the neutron irradiations. Comparison above of EPR spectra for Co^{60} γ-ray and 14.8 MeV neutron irradiation of Suprasil W1 and Sk7 samples (Figs. 1.19, 1.20, 1.28, 1.29) has shown that fast neutrons lead to the creation of some paramagnetic defects which are not produced by the 1 MeV γ-rays. Since primary collisions consisting of energetic atomic displacements are the main difference in the microscopic

damage events associated with fast neutrons and γ-rays, it is likely that the centers produced by fast neutrons only are associated with atomic displacement events in the material. This is the conclusion which has been reached above for the "E_2'" peak in 14.8 MeV neutron irradiated Suprasil W1.

Qualitative characteristics of the EPR spin density measurements have been used to illuminate the nature of the microscopic damage mechanisms in these experiments. The differences in the spin density for Co^{60} γ-ray irradiation of Suprasil and Bk7 samples has been interpreted above in terms of electron ionization effects in these materials. The much smaller differences in spin densities in these samples from 14.8 MeV neutron irradiation has suggested that ionization events are not the dominant damage mechanism for fast neutron irradiation. This is because if radiation damage associated with energetic ionized electrons was a dominant mechanism for 14.8 MeV neutron irradiation, then the relative spin densities for fast neutron irradiated samples would probably have been very similar to the relative behavior observed for Co^{60} irradiation. These considerations further suggest that, for 14.8 MeV neutrons, displacement damage may be the dominant microscopic mechanism leading to paramagnetic defects, because the rates of displacement events should probably be the same in the different glasses.

The data also suggests that damage associated with γ-rays created by inelastic collisions with 14.8 MeV neutrons does not have a large contribution to the overall damage behavior. Inelastic scattered γ-rays from O^{16} and Si^{28} atoms have energies of 1.77 MeV and higher. These γ-rays would lead to radiation damage spin density behavior similar to that observed with the 1 MeV Co^{60} γ-rays.

Comparison of the E' spectra for Suprasil W1 samples irradiated by Co^{60} γ-rays and 14.8 MeV neutrons can be used to further speculate on the microscopic damage mechanisms associated with fast neutrons. For Co^{60} γ-ray irradiation, the E_2' peak has a very small amplitude (Fig. 1.19), and may

indicate the presence of small numbers of defects associated with atomic displacement. For 14.8 MeV neutrons, the E_2' and E_1' peaks have equal amplitude (Fig. 1.20), suggesting that microscopic defects associated with atomic displacements (i.e., E_2' centers) occur with densities equal to the defects associated with ionization processes. And if atomic displacement events can lead to both the E_1' and E_2' type defects in Suprasil I, then the majority of microscopic paramagnetic defects resulting from exposure to 14.8 MeV neutrons will be due to atomic displacement events.

Although it is not entirely justified, it is interesting to analyze the spin density data for 14.8 MeV neutron irradiations on the basis of the assumption that microscopic damage due to the neutrons is entirely due to atomic displacement events in the material. The number of primary collisions N_p for 14.8 MeV neutron irradiation of SiO_2 can be written approximately as:

$$N_p = N_A \sigma F , \tag{1.129}$$

where N_A is the density of Si and O atoms, σ is the average elastic scattering cross section and F is the neutron fluence. For SiO_2,[49]

$$N_A \approx 6.6 \cdot 10^{22}/\text{c.c.} , \tag{1.130}$$

and

$$\sigma \approx 1.7 \cdot 10^{-24} \text{ cm}^2 .$$

Thus, from eq. (1.129) for a neutron fluence of 10^{16} n/cm^2, we have:

$$N_p \approx 10^{15} \text{ primaries/c.c.} \tag{1.131}$$

For elastic collisions with Si or O atoms, an average of about 1.75 MeV kinetic energy is transferred to the knock-on ion.[49] Of this deposited energy, only about 1% is deposited in atomic displacements, and the remainder is dissipated in electronic ionizations. Thus we find that about $2 \cdot 10^{13}$ MeV/c.c. is deposited in atomic displacement events. And, using eq. (1.5) we find (assuming $E_d \approx 25$ eV) that about $4 \cdot 10^{17}$ atomic displacements per c.c. are expected for exposure to 10^{16} neutrons/cm^2. From Fig. 1.37 we see that this

result is in agreement with the data. Thus, if defects resulting from exposure to 14.8 MeV neutrons are due to atomic displacement events, then the data also suggests that most of the resulting defects are paramagnetic, because they have been detected with the expected spin densities.

The last topic which will be considered in this discussion is the nature of "clusters" of defects which may occur as a result of radiation damage by 14.8 MeV neutrons. The spin density and dipole broadened E' spectrum of sample #642 (Fig. 1.13) have been used to suggest that damage occurs randomly throughout the material microstructure. This behavior is certainly expected for γ-ray irradiation, but for 14.8 MeV neutrons and the resulting energetic ions in the material, it may be expected that clusters of defects will develop in the microstructure. It is interesting to consider the probable nature of these clusters in order to see if they are consistent with the random distribution of defects postulated for sample #642.

An Si or O primary knock-on from an elastic collision with a 14.8 MeV neutron has an average kinetic energy of about 1.75 MeV[49] and a range of about 2 microns.[50] From the results above, we know that each primary knock-on produces about 500 atomic displacements. But since the primary has a range of 2μm, the displacement events are restricted to occur within a volume[50] of about $5 \cdot 10^{-14}$ c.c. This volume, with 500 paramagnetic centers will have an average spin density of about 10^{16} spins/c.c. In eq. (1.106) we have seen that spin densities greater than 10^{18} spins/c.c. are required to lead to observable dipole-dipole broadening of E' spectra. Thus, the density of 10^{16} spins/c.c. is associated with dipole-dipole broadening which is much too small to detect in E' spectra. Thus, defect clusters resulting from 14.8 MeV neutrons in fused SiO_2 will not lead to dipole broadening which can be observed in the corresponding E' spectra. However, for high spin densities (as in sample #642), these clusters will overlap, leading to an effectively random distribution of spins and a corresponding magnitude of dipole-dipole

broadening of the E' spectrum. Thus, our analysis of the broadening of the E' spectrum of sample #642 in terms of dipole-dipole broadening appears to be consistent with the expected nature of microscopic damage in the glass.

VI. SUMMARY AND CONCLUSIONS

This portion of the thesis has described the use of EPR to study radiation damage in silicate glasses. Careful measurements of EPR spin densities, spectral lineshapes and power saturation behavior have been used to characterize radiation damage resulting from exposure to Co^{60} γ-ray, 14.8 MeV neutron and reactor core radiation sources. The EPR data has been used to interpret both microscopic and macroscopic aspects of radiation damage: EPR spectra are sensitive to the microscopic nature of radiation damage, while paramagnetic spin densities and power saturation behavior are related to bulk characteristics of the damage. Analysis of the data has relied strongly on the comparison of major quantitative and qualitative differences in the data for different experimental conditions. The data has been interpreted in a self-consistent manner in terms of the microscopic damage mechanisms associated with the different experimental situations. Aside from the knowledge gained about the specific systems studied, EPR has been shown to be a sensitive tool for quantifying the extent of radiation damage in dielectric materials.

In Bk7 glass, comparison of total paramagnetic spin densities resulting from exposure to Co^{60} γ-rays and 14.8 MeV neutrons has demonstrated the effectiveness of γ-rays for creating paramagnetic spin states at electron and hole trapping sites in the material, and the relative ineffectiveness of the fast neutrons for inducing occupation of these states. This difference in behavior for the two types of radiation is apparently due to the fact that Co^{60} γ-rays lead to the production (via Compton scattering) of energetic ($E \simeq 100$ KeV) electrons in the material, while the fast neutrons lead mainly to the production of scattered electrons with energies less than 100 eV. This comparison has also demonstrated that gamma rays produced by (n,γ) inelastic neutron scattering mechanisms in the samples do not play a major role in fast-neutron induced damage in the silicate glasses used in these experiments.

Absolute spin densities measured in Bk7 glass exposed to Co^{60} γ-rays have been interpreted in terms of the energy deposited in the material per

resulting paramagnetic spin. This energy is determined on the basis of the assumption that most of the radiation-induced spin centers result from the occupation of trapping sites by scattered electrons. Although we were unable to do so with our samples, data of this type can be used to determine the minimum scattered electron energy which is required to create a paramagnetic trapping state in the material. This energy will depend on the type and composition of the material of interest and is a fundamental characteristic of radiation damage mechanisms. In order to obtain this number for Bk7 glass, it would be necessary to use γ-ray doses in the range of 10^3 to 10^4 rads, so that the resulting spin densities would be well below their maximum possible values. This is because for larger gamma ray doses, nearly all of the trapping sites will be occupied and the corresponding spin densities will be "saturated". For Bk7 samples exposed to 10^6 to 10^9 rads of Co^{60} γ-rays, the energy deposited per resulting spin varied from 650 eV to 500 keV, respectively. These energies are quite large and reflect the fact that the spin densities are saturated for this range of doses. The saturation of the spin densities is also evident in the spin density data (Fig. 1.32), where an increase of three orders of magnitude in the gamma ray dose results in an increase in the corresponding spin densities of less than a factor of ten.

Absolute spin densities measured in Bk7 and Suprasil samples exposed to 14.8 MeV neutrons have been successfully interpreted in terms of atomic scattering mechanisms in the glasses. The measured spin densities were found to be roughly equal to the number of atomic displacement events expected on the basis of a simplified description of the microscopic aspects of fast-neutron induced damage. In this analysis, energetic ($E \approx 2$ MeV) Si and O primary knock-on ions (resulting from elastic collisions with the incident neutrons) are assumed to create additional atomic displacements (about 800 per primary knock-on) and energetic ions in a cascade of Coulombic collisions with nucleii in the material. The agreement between this simple description

of fast-neutron induced damage and the measured spin densities further supports the assertion made above that γ-rays produced by inelastic scattering of neutrons do not play a major role in the radiation damage behavior of these experiments.

Measurements of the EPR spectra of radiation induced paramagnetic defects in Suprasil samples (which are collectively termed E' lineshapes) described in this thesis are the most careful measurements performed to date on these systems. While recording the spectra, very low signal detection frequencies were used (≈ 40 Hz) in order to avoid undesirable passage effects associated with the long relaxation times of these systems. In addition, ultra-low microwave powers (≤ 0.1μW) were used in order to avoid complications associated with the power saturation of inhomogeneous spectral systems.

The spectral measurements have resolved a previously unreported feature with g = 2.0020 and a number of qualitative variations in the E' lineshapes of Suprasil 1 and Suprasil W1 samples irradiated in the different neutron and gamma-ray facilities. Because the E_2' center in crystalline quartz has closely corresponding g-values, the spectral feature with g = 2.0020 has been tentatively interpreted as the occurrence of the E_2' center in the Suprasil samples.

Measurements of the continuous-wave power saturation of the E' spectra have been used to estimate the relaxation times, T_1 and T_2, for specific samples. In contrast with previously reported results, T_1 has been found to vary inversely with the total paramagnetic spin density. T_2 has been found to be consistent with the value expected on the basis of dipole-dipole interactions between the individual centers.

Comparison of spin densities in Suprasil 1 and Suprasil W1 has failed to establish any systematic relationship between the radiation damage behavior of these two glasses for the radiation sources used in the present experiments. The observed differences in behavior emphasize the care which must be used when

comparing the effects of radiation on generic materials which may differ in base composition, impurity content or fabrication technique.

The differences between the radiation-induced EPR spectra of Suprasil 1 and Suprasil W1 samples suggest that there are differences between the microscopic structure of these two glasses. This is a surprising result because any differences between these two glasses must result entirely from the different techniques used for their fabrication. In particular, the presence of the g = 2.0020 spectral peak in 14.8 MeV neutron irradiated Suprasil W1 and its near absence in Suprasil 1 indicates the presence of large numbers of an additional type of defect in Suprasil W1; implying an associated difference between their base structures. The latter is a consequence of the fact that fast-neutron induced damage occurs largely as a consequence of atomic displacement events in the base glass microstructure.

For Suprasil samples, the correlation between the observed spectral broadening of the E' lineshape and that expected on the basis of dipole-dipole broadening has established an upper limit on the net spin densities of "clusters" of defects which may occur in the samples. The expected dipole broadening was determined on the basis of the assumption that damage centers were randomly distributed in the samples. From this analysis, dipole broadening was expected to be observed in samples with spin densities greater than 10^{18}/c.c. Spectral broadening with the expected amplitude was observed in a sample with $3.4 \cdot 10^{18}$ spins/c.c. Thus, if clusters of defects do occur, then they must have net spin densities less than 10^{18} spins/c.c. This result is consistent with the relatively large defect clusters which can be expected for 14.8 MeV neutron irradiation, where a primary knock-on ion has a range of about 2 μm and can be expected to produce a cluster of defects with a net spin density of about 10^{16} spins/c.c.

In conclusion, the internal self-consistency of the data and the agreement of the data with that expected on the basis of simplified descriptions of

radiation damage mechanisms demonstrates the usefulness of EPR to quantify radiation damage in dielectrics. This will be useful for interpreting radiation induced changes in bulk physical properties through changes in the associated EPR characteristics. For gamma-ray irradiation, where damage occurs as a consequence of electron scattering, a close relationship is expected between paramagnetic spin densities and changes in bulk physical properties related to the occupation of trapping states in the material (e.g., electrical conductivity or optical absorption). For fast neutron irradiation, where the relationships are much more difficult to predict than for gamma-rays, useful empirical relationships can be expected between changes in EPR behavior and changes in the bulk mechanical properties of a material (e.g., stress-strain coefficients, or brittleness).

REFERENCES

1. a) F. L. Vook, *et al.*, "Report to the American Physical Society by the study group on physics problems relating to energy technologies: Radiation effects on materials," *Rev. Mod. Physics*, vol. 7, suppl. 3, pp. S1-S44, Winter 1975.

   b) F. L. Vook, "Effects of radiation on materials," *Physics Today*, vol. 28, no. 9, pp. 34-40, Sept. 1975.

2. R. J. Teitel, "Anticipated radiation damage problems to laser optics," *Nucl. Mat'ls.*, vol. 53, pp. 349-353, 1974.

3. "Intern. Conf. on radiation effects and tritium technology for fusion reactors," Oct. 1-3, 1975, Gatlinburg, Tenn.

4. A. Bishay, "Radiation Induced color centers in multicomponent glasses," *J. Non-Cryst. Sol.*, vol. 3, pp. 54-114, 1970.

5. D. L. Griscom, "E.S.R. studies of radiation damage and structure in oxide glasses not containing transition group ions," *J. Non-Cryst. Sol.*, vol. 13, pp. 251-285, 1973/1974.

6. J. B. Bates, R. W. Hendricks, and L. B. Shaffer, "Neutron irradiation effects and structure of noncrystalline SiO_2," *J. Chem. Phys.*, vol. 61, no. 10, pp. 4163-4176, Nov. 1974.

7. W. Primak, "A review of the gross structural effects of energetic atomic particles on vitreous and crystalline silica," *J. Phys. Chem. Sol.*, vol. 13, pp. 279-286, 1960.

8. a) R. DiSalvo, D. M. Roy, and L. N. Mulay, "EPR studies of radiation damage in hydrogen-impregnated glass," *J. Am. Ceram. Soc.*, Vol. 55, no. 10, pp. 536-537, Oct. 1972.

   b) S. P. Faile and D. M. Roy, "Mechanism of color center destruction in hydrogen impregnated radiation resistant glasses," *Mat. Res. Bull.*, Vol. 5, pp. 385-390, 1970.

9. E. J. Friebele, R. I. Ginther, and G. H. Sigel, Jr., "Radiation protection of fiber optic materials: Effects of oxidation and reduction," *Appl. Phys. Lett.*, Vol. 24, no. 9, pp. 412-414, 1 May 1974.

10. W. Primak, "A review of the gross structural effects of energetic atomic particles on vitreous and crystalline silica," *J. Phys. Chem. Sol.*, Vol. 13, pp. 279-286, 1960.

11. a) D. S. lington and J. H. Crawford, "Radiation damage in solids," Prince Univ. Press, Princeton, N.J., 1961.

    b) J. F. Kircher and R. E. Bowman, "Effects of radiation on materials and components," Reinhold Publ. Co., New York, 1964.

12. H. M. Presby and W. L. Brown, "Refractive index variations in proton bombarded fused silica," *Appl. Phys. Lett.*, vol. 24, no. 10, pp. 511-513, 15 May 1974.

13. V. E. Culler and H. E. Rexford, "Gamma-radiation-produced conductivity in glasses," *Proc. IEE*, vol. 112, no. 7, pp. 1462-1467, July 1965.

14. S. Weissman, T. Imura, K. Nakajima, and J. E. Wisnewski, "Lattice defects of Quartz induced by fast neutron irradiation," Proc. Int. Conf. on Crystal Lattice Defects, 1962, *Conf. Journ. Phys. Soc. Japan*, Vol. 18, Suppl. III, pp. 179-188, 1963.

15. C. M. Nelson and J. H. Crawford, Jr., "Optical absorption in irradiated quartz and fused silica," *J. Phys. Chem. Sol.*, vol. 13, pp. 296-305, 1960.

16. R. H. Silsbee, "Electron spin resonance in neutron irradiated quartz," *J. Appl. Phys.*, vol. 32, no. 8, pp. 1459-1462, Aug. 1961.

17. Two standard textbooks were used as the main references for the material in this section. They are:

    a) D. S. Billington and J. H. Crawford, "Radiation damage in solids," Princeton Univ. Press, Princeton, N. J., 1961.

    b) J. F. Kircher and R. E. Bowman, "Effects of radiation on materials and components," Reinhold Publ. Corp., New York, N.Y., 1964.

18. Much of the background information on glasses that we use in this report is contained in the following review article:

    E. U. Condon, "Physics of the glassy state. I constitution and structure," *Am. J. Phys.*, vol. 22, no. 2, pp. 43-53, Feb. 1954.

19. G. J. Dienes, "Defects in Silicas," *J. Phys. Chem. Solids*, vol. 13, pp. 272-278, 1960.

20. a) B. E. Warren, "X-ray determination of the structure of liquids and glass, *J. Appl. Phys.*, Vol. 8, pp. 645-54, Oct. 1937.

    b) B. E. Warren, H. M. Krutter and O. Morningstar, "Fourier analysis of x-ray patterns of vitreous SiO_2 and B_2O_3," *J. Amer. Ceram. Soc.*, vol. 19, no. 7, pp. 202-206, 1936.

21. C. V. Gokularathnam, R. W. Gould, and L. L. Hench, "Effect of water on the structure of vitreous silica," *Phys. and Chem. Glasses*, Vol. 16, no. 1, Feb. 1975, pp. 13-16.

22. a) C. M. Nelson and R. A. Weeks, "Trapped elections in irradiated quartz and silica I, Optical Absorption," *J. Am. Ceram. Soc.*, Vol. 43, No. 3, pp. 396-398, Aug. 1960.

    b) R. D. Weeks and C. M. Nelson, "Trapped electrons in irradiated quartz and silica II, Electron spin resonance," *J. Am. Ceram. Soc.*, Vol. 43, No. 3, pp. 399-404, Aug. 1960.

23. I. Ebert, "On the interpretation of an ESR spectrum of γ-irradiated silicate glasses," *Phys. Stat. Sol.*, (6), 60, K103-4, 1973.

24. D. Loveridge and S. Parke, "Electron spin resonance of Fe^{3+}, Mn^{2+}, and Cr^{3+} in glasses," *Phys. and Chem. Glasses*, vol. 12, no. 1, pp. 19-26, Feb. 1971.

25. G. E. Peterson, C. R. Kurkjian, and A. Carnevale, "Random structure models and spin resonance in glass," *Phys. and Chem. Glasses*, vol. 15, no. 2, pp. 52-58, April 1974.

26. P. C. Taylor, I. F. Baugher and H. M. Kriz, "Magnetic resonance spectra in polycrystalline solids," *Chem. Rev.*, vol. 75, no. 2, pp. 203-39, 1975.

27. Sook Lee and P. J. Bray, "Electron-Spin-Resonance studies of irradiated alumino-silicate glasses," *Phys. and Chem. of Glasses*, vol. 3, no. 2, pp. 37-42, April 1962.

28. G. E. Pake, "Paramagnetic Resonance," W. A. Benjamin, New York, 1962.

29. C. P. Slichter, "Principles of Magnetic Resonance," Harper and Row, New York, 1963.

30. A. Abragam, "The principles of nuclear magnetism," Oxford University Press, London, 1961.

31. C. P. Poole, "Electron Spin Resonance," Interscience Publishers, 1967, John Wiley and Sons, New York.

32. R. S. Alger, "Electron Paramagnetic Resonance," Interscience Publishers, New York, 1968.

33. A. M. Portis, "Electronic structure of F centers: saturation of the Electron Spin Resonance," *Phys. Rev.*, vol. 91, no. 5, pp. 1071-8, Sept. 1953.

34. T. G. Castner, "Saturation of the Paramagnetic Resonance of a V center," *Phys. Rev.*, vol. 115, no. 6, Sept. 1959.

35. R. H. Sands, "Paramagnetic Resonance in glass," *Phys. Rev.*, vol. 99, no. 4, pp. 1222-6, Aug. 1955.

36. R. A. Van Konynenburg, H. H. Barschall, R. Booth and C. Wong, "Characteristics of rotating target neutron source and its use in radiation damage studies," International Conference on Radiation Test Facilities for the CTR Surface and Materials Program, July 15-18, 1975, Argonne National Laboratory, Argonne, Ill., Report No. ANL/CTR-75-4, p. 171.

37. Wade J. Richards, "User's guide Livermore Pool Type Reactor," unpublished.

38. Bk7 is a borosilicate glass manufactured by the Schott Glass Co.

39. Trademark of W.C. Heraeus-Schott Company, Germany; and Amersil division, Engelhard Industries, Inc.

40. a) J. G. Castle, Jr., D. W. Feldman, and P. G. Klemens and R. A. Weeks, "Electron spin-lattice relaxation at defect sites; E' centers in synthetic quartz at 3 kilo-oerstads," *Phys. Rev.*, vol. 13, no. 2, pp. 577-88, April 1963.

b) J. G. Castle and D. W. Feldman, "Temperature dependence of Paramagnetic Relaxation at point defects in fused silica," *J. Appl. Phys.*, vol. 36, no. 1, pp. 124-8, Jan 1965.

41. A. M. Portis, "Magnetic resonance in systems with spectral distributions," Technical Note No. I, Sarah Mellon Scaife Radiation Laboratory, Univ. Pittsburgh, Pittsburgh, Pa., Nov. 1955.

42. J. A. Carruthers and N. S. Rumin, "Measurement of spin-lattice relaxation at 890 Mc/s by a resonance dispersion technique," *Canad. J. Phys.*, Vol. 45, pp. 576-93, April 1965.

43. A. M. Portis, "Rapid passage effects in Electron Spin Resonance," *Phys. Rev.*, vol. 100, pp. 1219-21, 1955.

44. M. Weger, "Passage effects in paramagnetic resonance experiments," *Bell Syst. Tech. J.*, vol. 39, pp. 1013-1113, Feb. 1960.

45. G. H. Sigel, Jr., B. D. Evans, R. J. Ginther, E. I. Friebele, D. L. Griscom and J. Babiskin, "Radiation effects in fiber optic waveguides," N.R.L. Memorandum Report 2934, p. 53, Nov. 1974, Naval Research Laboratory, Washington, D.C.

46. C. Kittell and E. Abrahams, "Dipolar broadening of magnetic resonance lines in magnetically diluted crystals," *Phys. Rev.*, vol. 90, no. 2, pp. 238-9, April 1953.

47. R. D. Evans, "Gamma rays." American Institute of Physics Handbook, third edition, D. E. Gray, ed., McGraw-Hill Book Co., 1957, pp. 8-190-8-209.

48. O. S. Oen and D. K. Holmes, "Cross sections for atomic displacements in solids by gamma-rays," *J. Appl. Phys.*, vol. 30, no. 8, Aug 1959, pp. 1289-95.

49. E. F. Plechaty, D. E. Cullen, R. J. Hawerton and J. R. Kimlinger, "Tabular and graphical presentation of 175 neutron group constants derived from the LLL evaluated neutron data library," Lawrence Livermore Laboratory report #UCRL-50400, vol. 16, rev. 1, April 1976.

50. J. F. Gibbons, W. S. Johnson and S. W. Mylroie, "Projected range statistics," Dowden, Hutchinson & Ross, Inc., Stroudsburg, Pa., 1975.

51. G. J. Dienes and G. H. Vineyard, "Radiation effects in solids," Interscience Publishers, inc., New York, 1957.

52. D. L. Griscom, E. J. Friebele and G. H. Sigel, Jr., "Observation and analysis of the primary Si^{29} hyperfine structure of the E' center in non-crystalline SiO_2, *Solid State Commun.*, vol. 15, pp. 479-483, 1974.

53. John Vitko, private conversation.

54. R. A. Weeks, "Paramagnetic resonance of lattice defects in irradiated quartz," *J. Appl. Phys.*, vol. 27, no. 11, pp. 1376-81, Nov. 1956.

55. J. W. H. Schreurs, "Study of some trapped hole centers in χ-irradiated alkali silicate glasses," *J. Chem. Phys.*, Vol. 47, no. 2, pp. 818-30, July 1967.

56. C. Kittel and E. Abrahams, "Dipolar broadening of magnetic resonance lines in magnetically diluted crystals," *Phys. Rev.*, Vol. 90, No. 2, pp. 238-39, April 1953.

57. D. A. Bozanic, D. Mergerian and R. W. Minarik, "Electron spin-echo measurements of E_1' centers in crystalline quartz," *Phys. Rev. Lett.*, Vol. 21, No. 8, pp. 541-2, Aug. 1968.

58. J. W. Corbett, "Electron radiation damage in semiconductors and metals," *Solid State Physics, Suppl. 7*, Academic Press, New York, 1966.

PART II: MEASUREMENT OF THE NONLINEAR OPTICAL INDEX COEFFICIENT N_2

I. INTRODUCTION

Neodymium doped silicate laser glasses are the most important solid state laser materials in use today. This dominance is due partly to the nearly exclusive use of these glasses in the construction of high power, short pulse laser systems. While a large variety of solid state materials have been used in the design of short pulse lasers, a combination of physical and economic characteristics make silicate glasses the most convenient materials at the present time. Continuing materials research hopes to lead to the development of laser media with the economic advantages of glasses but with far superior physical and lasing characteristics than the present silicate glasses. Because of the mammoth laser systems under development, relatively modest gains in materials technology can lead to significant savings in laser construction.

Solid state laser materials generally consist of an optically passive host material doped with a controlled quantity of lasing ions. The host material may be either crystalline or glassy, and a variety of lasing ions have been used for generating a wide spectrum of infrared and visible laser wavelengths. The choice of laser material depends both on the desired optical characteristics of the laser and on the expense of realizing the desired behavior.

The major advantages of glassy host materials is that, compared to crystalline hosts, they are inexpensive to fabricate in a large size with excellent optical quality and have a relatively high slope efficiency. On the other hand, crystalline laser materials often result in lasers with lower laser threshold energies and better spectroscopic properties (such as narrow laser spectral bandwidth) than glasses. Many of these differences result from the nearly identical laser ions sites in well-

ordered crystals compared to the varied, nearly random sites which seem to prevail in the amorphous glasses. This contrast is well-illustrated by the differences between common Nd:glass lasers and Nd:YAG crystal lasers. A glass laser rod 1/4" by 3" may cost several hundred dollars and have a laser bandwidth of about 100Å, while a comparable YAG rod may cost several thousand dollars and have a characteristic laser bandwidth of about 10Å. The laser threshold pumping energy for YAG can be an order of magnitude less than that for glass.

The usefulness of a laser material is determined not only by its lasing characteristics, but also by its more mundane physical properties. It is desirable that the optical quality of a laser rod be maintained during laser operation in spite of the mechanical and thermal strasses caused by flashlamp pumping. A laser material must also have a heat conductivity large enough to allow the dissipation of excess heat. Many problems of this kind must be considered in the design of a solid state laser.

The nonlinearity of the index of refraction is another important physical property of laser materials. Electric field intensities of laser beams often reach levels which alter the fundamental behavior of the laser medium. This change is often observed as a change in the index of refraction. These self-induced changes can profoundly alter the propagation of the laser beam and in some cases lead directly to permanent damage in the laser material. Such behavior is a fundamental limitation in the operation of current laser systems.

Beam propagation effects associated with an intensity dependent index of refraction have been an important design factor in the development of short pulse, high peak intensity lasers. This is especially true for solid

s . e lasers. The radial dependence of the laser beam intensity distribution leads to both gross spatial beam distortions[1] and small scale fluctuation instabilities;[2] while the time dependence of the intensity distribution leads to self-phase modulation[3] and optical shocks[4] (particularly when linear chromatic dispersion is important).[5] For pulse durations near T_2 (the transition dephasing time) of the system, the presence of an intensity dependent refractive index can further complicate the coherent pulse propagation problem.[6]

At high peak laser powers, most of the above effects can result in catastrophic instabilities leading to damage in the laser materials. The most common source of damage is optical self focusing caused by spatial irregularities in the laser beam intensity distribution. Because the small signal or perturbation analysis of these effects involves exponentially growing Fourier Components, the magnitude of n_2 must be accurately determined in order to characterize the pulse propagation problem.

The nonlinear index coefficient n_2 is defined by the equation

$$n = n_0 + n_2\langle E^2\rangle = n_0 + \Delta n \quad , \tag{2.1}$$

where n_0 is the linear index of refraction of the material, $\langle E^2\rangle$ is the electric field intensity associated with the laser beam, and Δn is the change in the dex of refraction.

Many me ods[7] have been employed to measure n_2, or more generally, the full te sor[8] $\chi_{ijkl}(-\omega,\omega,\omega,-\omega)$. Because direct measurement of the nonlinearity of the refractive index is inherently difficult, most previous determinations of n_2 have been inferred from indirect data. For example, Duguay, et al.,[7] estimated the n_2 of Nd:laser glass from spectral broadening measurements of the Nd:glass laser emission. For high power laser design,

the most useful n_2 measurements are those which directly measure optical perturbations, such as slight changes in frequency or wave length of the laser radiation. Interferometric measurements of n_2 are one way of directly measuring these effects of optical nonlinearities.

Although the interferometric technique has long been recognized as a desirable procedure for measuring n_2,[8] experimental capabilities for performing the experiment have only recently been realized. A particularly attractive technique for performing this class of measurements is to use a Mach-Zehnder interferometer. This technique was first attempted[9] in 1968 in a form where the output fringe pattern was time integrated. A time resolved fringe pattern for this experiment yields both more information and improved precision[10,11] than previously used techniques. However elimination of systematic errors and the establishment of the actual peak laser intensity still limit the experimental accuracy in references 10 and 11.

In this thesis, the author describes measurements of the nonlinearity of the index of refraction performed with time resolved interferometry and a 1 nsec laser system. The experiments use a Mach-Zehnder interferometer, where one arm of the interferometer contains a sample of unknown nonlinearity and the second arm contains a compensating cell of CS_2 with nearly the same linear optical path length and a known nonlinear response.[12] The experiments determine the ratio of the nonlinearity in the unknown sample to that in CS_2 in a situation where systematic errors are removed and high precision is possible. Relative numbers are believed to be correct to ±10% absolute accuracy.

These measurements are performed with a 1.06 um Nd:glass laser system on a variety of materials relevant to high power solid state laser systems. We examine several different Nd doped laser glasses and look for differences

in the index nonlinearity. The n_2 of ruby and Nd:YAG are also determined. We also examine passive optical materials such as lucite and a lead-doped Faraday rotator glass.

The absence of an accurate and versatile theoretical method for predicting the n_2 of optical materials makes the accurate experimental determination of these numbers even more desirable. Current formalisms[13,14] for predicting n_2 tend to describe a rather narrow range of materials and are sensitive to small changes in the data used for calculating n_2's. Experimental measurements of n_2 can help to clarify the theoretical problems and perhaps illuminate the mechanisms responsible for n_2. Such an understanding of the problem would eventually lead to techniques for further optimization of laser materials.

II. THEORY OF EXPERIMENT

A. Introduction

Nonlinearity of the index of refraction of a material can affect the propagation of a laser beam. For solid materials, the nonlinearity is usually small enough so that it can be neglected; but with the intense laser beams currently available, the optical nonlinearity becomes significant.

The theoretical description of nonlinear propagation is a straightforward extension of the description of linear propagation. For linear propagation, the microscopic response of the material to optical fields is specified in terms of an electric susceptibility $\chi(\omega)$ and a resultant polarization $\vec{P}(t)$ with the same frequency as the applied field:

$$\vec{P}(t) = \chi(\omega)\vec{E}(t) \quad , \tag{2.2}$$

where $\vec{E}(t)$ is the optical electric field. When this polarization is included in Maxwell's equations, the resulting differential equations lead to the standard descriptions of linear propagation.

For nonlinear propagation, the dielectric response of the material is described by expanding the induced polarization in a power series in the applied optical electric fields. When this nonlinear polarization is inserted into Maxwell's equations, the result is a set of coupled nonlinear differential equations which allow few analytic solutions. For an arbitrary situation, accurate solutions to these equations can be obtained only with numerical techniques.

For many commonly encountered situations, approximations in the propagation equations allow the derivation of results which approximately predict nonlinear propagation behavior. While these results are not exact, they are useful because they establish useful parametric relationships

between the optical nonlinearities, the laser beam intensity, and characteristics of nonlinear propagation.

B. Linear Electric Susceptibility and Polarization

The electric field associated with an optical traveling wave can be written:

$$\vec{E}(t) = \vec{\mathcal{E}}(t) \cos(\omega_0 t - k_0 z - \Phi(z,t)) \tag{2.3}$$

where $\vec{E}(t)$ is the electric field amplitude, $\vec{\mathcal{E}}(t)$ is the "envelope" of the electric field, ω_0 is the laser beam frequency, k_0 is the wave number, and $\Phi(z,t)$ is a function allowing for description of an arbitrary phase factor. The electric field can also be expressed in frequency space by its Fourier transform:

$$\vec{E}(t) = \frac{1}{\sqrt{2\pi}} \int_{-\infty}^{\infty} \vec{E}(\omega) e^{-i\omega t} \, d\omega \quad , \tag{2.4a}$$

where

$$\vec{E}(\omega) = \frac{1}{\sqrt{2\pi}} \int_{-\infty}^{\infty} \vec{E}(t) e^{i\omega t} \, dt \quad . \tag{2.4b}$$

The response of dielectric materials to optical electric fields is described in terms of the susceptibility $\chi(\omega)$ and polarization $\vec{P}(t)$ of Eq. (2.2). For linear systems, Eq. (2.2) is a perfectly adequate definition of electric susceptibilities, but for nonlinear systems, it is useful to make the definition in frequency space:

$$\vec{P}(\omega) = \chi(\omega)\vec{E}(\omega) \tag{2.5}$$

The time dependent polarization $\vec{P}(t)$ is obtained from the Fourier transform of $\vec{P}(\omega)$:

$$\vec{P}(t) = \frac{1}{\sqrt{2\pi}} \int_{-\infty}^{\infty} \vec{P}(\omega) e^{-i\omega t} \, d\omega \quad . \tag{2.6}$$

Appendix 1 demonstrates that this equation can be used to derive the useful relation for $\vec{P}(t)$:

$$\vec{P}(t) = \chi_{op}(i\frac{\partial}{\partial t})\vec{E}(t) \quad , \tag{2.7}$$

where

$$\chi_{op}(i\frac{\partial}{\partial t}) = \chi(\omega_o) + \frac{i}{2!}\frac{\partial \chi}{\partial \omega}\Big|_{\omega = \omega_o}\frac{\partial}{\partial t} - \frac{1}{3!}\frac{\partial^2 \chi}{\partial \omega^2}\Big|_{\omega = \omega_o}\frac{\partial^2}{\partial t^2} + \ldots$$

Here, $\chi_{op}(i\frac{\partial}{\partial t})$ is a differential operator which describes the electric susceptibility and all orders of dispersion through the differential time operators. The first term $\chi(\omega_o)$ is the usual linear susceptibility. The $\frac{\partial \chi}{\partial \omega}$ term accounts for linear chromatic dispersion, while the $\frac{\partial^2 \chi}{\partial \omega^2}$ term describes second order dispersion. Higher order terms can also be included in the expansion, but are not of interest here. When the first two terms of χ_{op} are included in Maxwell's equations, the resulting propagation equations give the correct group velocity $\frac{d\omega}{dk}$ for light propagation, rather than the phase velocity $\frac{\omega}{k}$ which would result if dispersion was neglected.

When linear chromatic dispersion is small, the electric field envelope $\vec{E}(t)$ has negligible variations during an optical cycle and nonlinear contributions are not significant, the rigorous result of Eq. (2.7) reduces to the original definition of Eq. (2.2):

$$\vec{P}(t) = \chi(\omega_0)\vec{E}(t) \tag{2.2}$$

For most situations, $\chi(\omega_0)$ is sufficient to describe light propagation. Strictly speaking, $\chi(\omega_0)$ is in general a second order tensor with nine elements; but for isotropic materials reduces to a single constant which specifies the index of refraction through the relation:

$$n_0 = \sqrt{1+4\pi\chi(\omega_0)} \quad . \tag{2.8}$$

C. Nonlinear Susceptibility and Polarization

When applied electric field intensities reach levels associated with nonlinear propagation, the response of dielectric materials is significantly altered. In this situation, it is convenient to express the polarization vector as a power series in the applied electric field amplitude:

$$\vec{P}(\omega) = \chi^{(1)}\vec{E}(\omega) + \chi^{(2)}\vec{E}^2(\omega) = \chi^{(3)}\vec{E}^3(\omega) + \ldots \tag{2.9}$$

The polarization is expressed in frequency space because the induced polarizations for nonlinear systems will generally have different frequencies than the driving optical fields. Here, $\chi^{(1)}$ is identical to the susceptibility $\chi(\omega)$ seen above, $\chi^{(2)}$ is a third rank tensor describing second order nonlinearities and $\chi^{(3)}$ is a fourth rank tensor which describes the third order nonlinearities.

Each of these susceptibilities is associated with specific aspects of light propagation. $\chi^{(1)}$ specifies the linear index of refraction through Eq. (2.8). The $\chi^{(2)}$ term is associated with nonlinear effects such as second harmonic generation, optical rectification, and parametric up or down conversion. Nonlinear effects associated with $\chi^{(3)}$ include third harmonic generation, Raman scattering, four-wave mixing, AC and DC Kerr effects, and

two photon absorption. Nonlinear effects due to $\chi^{(3)}$ which involve an induced polarization of the same frequency as the driving optical field are largely responsible for self-induced effects such as self-focusing and self-phase modulation. While $\chi^{(4)}$ and higher order terms can be included in the expansion of Eq. (2.9), they are responsible for nonlinear behavior which are either negligible or irrelevant to the present experiment and will not be discussed further. For discussing specific nonlinear behavior, it is advantageous to rewrite Eq. (2.9) in the form:

$$\vec{P}(\omega) = \sum_{i} \vec{P}^{(i)}(\omega) \quad ,$$

where

$$\vec{P}^{(i)}(\omega) = \chi^{(i)}(\omega)\vec{E}^{(i)}(\omega) \tag{2.10}$$

This definition simply establishes a notation for individually discussing different orders of optical nonlinearity.

The equations above show that a nonlinear optical polarization depends on a variety of frequency-dependent tensor operators. For a description of light propagation in isotropic materials, these tensor operators can be considerably simplified. In isotropic media, simple parity arguments demand that $\vec{P}^{(2)}(\omega)$ be identically equal to zero, so that second order nonlinearities can be neglected in isotropic materials.

Similar simplification of the $\chi^{(3)}$ tensor is also sometimes possible. The fourth rank tensor $\chi^{(3)}_{ijkl}(-\omega,\omega,\omega,-\omega)$ has 81 possible independent elements, where the subscripts refer to the direction of the appropriate electric field vectors. For isotropic materials and a monochromatic light source, the 81 elements reduce to only two independent terms. In this situation, the third order nonlinearity can be written:[7,15]

$$\vec{P}_i^{(3)}(\omega) = 6\chi_{1122}(-\omega,\omega,\omega,-\omega)|\vec{E}_j(\omega)|^2\vec{E}_i(\omega) + 3\chi_{1221}(-\omega,\omega,\omega,-\omega)\vec{E}_j(\omega)\cdot\vec{E}_j(\omega)\cdot\vec{E}_i^*(\omega) \tag{2.11}$$

The optical nonlinearities described above are directly related to nonlinear changes in the index of refraction. The relationship between the index of refraction and the electric susceptibility is specified by Eq. (2.8). When the third order nonlinearity is included, Eq. (2.8) takes the form:

$$n = \sqrt{\varepsilon_0 + \varepsilon_2 \langle E^2 \rangle}$$

where

$$\varepsilon_0 = 1 + 4\pi\chi^{(1)}$$

and

$$\varepsilon_2 = 4\pi\chi^{(3)} \tag{2.12}$$

When $\varepsilon_2 \ll \varepsilon_0$, this becomes

$$n \approx n_0 + n_2 \langle E^2 \rangle \quad ,$$

where

$$n_0 = \sqrt{\varepsilon_0} \quad ,$$

and

$$n_2 = \frac{\varepsilon_2}{2\sqrt{\varepsilon_0}} \quad . \tag{2.13}$$

The nonlinear index coefficient n_2 is the parameter most often employed to specify the optical nonlinearity of isotropic dielectrics. n_2 is not a refractive index, but is used to determine the index nonlinearity when the electric field intensity is known.

In transparent dielectrics, the fundamental origin of optical nonlinearities is either nuclear motion associated with the infrared or low frequency absorption edge or direct electronic excitations associated with the ultraviolet or high frequency cut-off of the material. The nonlinear susceptibilities can be related to these two different types of interactions.

In general, both nuclear and electronic motion may be induced by the electric field in a nonlinear manner. The basic idea of dividing the origin of the physical mechanisms responsible for the third order nonlinear susceptibilities was proposed by Hellwarth, et al.[16] They show that the third order polarization may be written (approximately) as the sum of an electronic contribution and a nuclear contribution:

$$\vec{P}^{(3)}(t) = \vec{P}_e^{(3)}(t) + \vec{P}_n^{(3)}(t) \tag{2.14}$$

Here, $\vec{P}_e^{(3)}(t)$ is the third order polarization resulting from nonlinear electronic interactions, and $\vec{P}_n^{(3)}(t)$ is the third order polarization resulting from nonlinear motion of nuclear positions in the material.

$\vec{P}_e^{(3)}(t)$ can also be considered to result from a distortion of electronic orbits about the nucleii in fixed position. $\vec{P}_e^{(3)}(t)$ is considered instantaneous because the distortion lifetime ($\sim 10^{-14}$ sec) is much shorter than the 1 nsec optical pulses of interest here. A single constant is sufficient to describe this contribution and is written:

$$\vec{P}_e^{(3)}(t) = \frac{1}{2}\chi \vec{E}^3(t) \tag{2.15}$$

Here, σ is an effective nonlinear susceptibility and the factor of $\frac{1}{2}$ is used to facilitate comparison with alternate definitions in the literature.

The situation is more complicated for the nuclear contribution to $\vec{P}_n^{(3)}(t)$. Since nuclear displacements are much slower typical electronic frequencies, time dependent response functions must be used. Also, nuclear motion has a second order contribution to nonlinear susceptibilities because electronic orbits depend on nuclear positions. Thus, two time response functions, a(t) and b(t), are needed to describe $\vec{P}_n^{(3)}(t)$:

$$\vec{P}_n^{(3)}(t) = \vec{E}(t)\int a(t-s)\vec{E}(s)\cdot\vec{E}(s)\,ds + \vec{E}(t)\cdot\int b(t-s)\vec{E}(s)\vec{E}(s)\,ds \qquad (2.16)$$

In this equation, the functions a(t) and b(t) serve as time dependent nonlinear susceptibilities.

In order to relate these results to the conventional susceptibilities discussed previously, it is convenient to transform to the frequency domain. The Fourier transforms of a(t) and b(t) give the frequency dependent susceptibilities $\alpha(\omega)$ and $\beta(\omega)$:

$$\alpha(\omega) = \frac{1}{\sqrt{2\pi}}\int_{-\infty}^{\infty} a(t)e^{i\omega t}dt \qquad (2.17a)$$

and

$$\beta(\omega) = \frac{1}{\sqrt{2\pi}}\int_{-\infty}^{\infty} b(t)e^{i\omega t}dt \qquad (2.17b).$$

These functions are related to the conventional susceptibilities through the equations:[15]

$$6\,\chi_{1122}(-\omega,\omega,\omega,-\omega) = 1/4[\sigma + 2\alpha(o)] \tag{2.18a}$$

$$6\chi_{1212}(-\omega,\omega,\omega,-\omega) = 6\chi_{1221}(-\omega,\omega,\omega,-\omega) = [\sigma/4 + \beta(o)] \tag{2.18b}$$

Eq. (2.18) have three independent contributions. For an experimental determination of these quantities, a single monochromatic light source with two polarizations is not sufficient. In order to independently determine the individual contributions, a second monochromatic light source light source at a different frequency would be necessary.

But useful information can be obtained with a single monochromatic light source. A comparison of nonlinear delays for linear and circular polarized light beams will determine the ratio:[17]

$$\frac{n_2(\text{linear})}{n_2(\text{circular})} = \frac{\chi_{1122} + \chi_{1212} + \chi_{1221}}{\chi_{1122} + \chi_{1212}} \tag{2.19}$$

Inspection of Eq. (2.18) will show that for nonlinearities with electronic contributions only, this ratio will be 3/2. But when nuclear contributions are present, the ratio will depend on the relative contributions for the specific system.

D. Nonlinear Propagation

Light propagation is described by the wave equation derived from Maxwell's equations. In a non-magnetic material with no free charges, this equation takes the form:

$$\nabla^2\vec{E} - \frac{1}{c^2}\frac{\partial^2\vec{E}}{\partial t^2} = \frac{4\pi}{c^2}\frac{\partial^2\vec{P}}{\partial t^2} \tag{2.20}$$

There are many approaches to solving this equation, and the most convenient approach depends on the situation being described.

For our experiment, the propagation problem can be greatly simplified. All of the characteristics of propagation that are of interest can be described in terms of a few parameters. We are interested in highly symmetric monochromatic laser beams with a finite beam diameter. Fig. 2.1 defines the parameters we use to specify the state of the laser beam. The beam propagates in the z-direction and has a cylindrically symmetric cross section with a Gaussian radial intensity distribution with a $\frac{1}{e}$ radius a(z). The radius of curvature R(z) specifies the local divergence of the beam. The wavelength of the light beam, λ determines the wave number, k, through the relation:

$$k = \frac{2\pi}{\lambda} \tag{2.21}$$

The laser beam used in the present experiment has a radial intensity profile which closely approximates a Gaussian distribution. This is fortunate, because propagation of a Gaussian beam in a linear dielectric medium is a completely solvable problem. This problem is solved in Appendix 2 and Fig. 2.1 can be used to illustrate the results. The results show that, for a beam with a plane wavefront at z = 0, as the beam propagates, the magnitude of the radius of curvature of the wavefronts decreases from $R = \infty$ at $z = 0$ to a minimum of $R = 2ka^2$ at $z = ka^2$ and then increases to $R = \infty$ at $z = \infty$. At the same time, the diameter of the beam increases hyperbolically with propagation distance. As the propagation distance z approaches infinity, the divergence angle of the beam asymptotically approaches the expected minimum uncertainty angle for the finite beam diameter. The most significant feature of this solution is that changes in the beam due to propagation occur in a smooth, continuous fashion, with the radial intensity distribution remaining Gaussian and

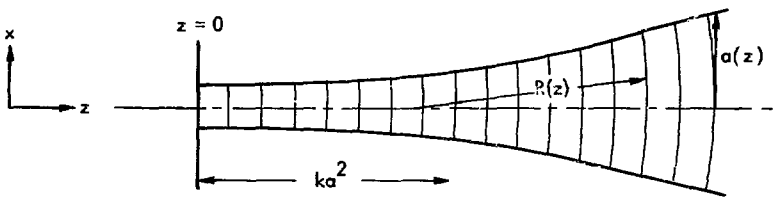

Figure 2.1 Gaussian Beam Propagation

Here, the propagation of a beam with a Gaussian radial intensity profile is schematically illustrated. The beam radius a(z) increases hyperbolically with the propagation distance from the beam waist. The radius of curvature of the beam wavefronts also changes as the beam propagates and has a minimum radius of curvature at a distance ka^2 from the beam waist.

developing none of the radial structure which is often characteristic of propagation (or diffraction) of cylindrically symmetric beams.

Propagation in a nonlinear medium can significantly alter propagation characteristics of a light beam. These differences enter the wave equation through the nonlinear polarization vector $\vec{P}(t)$. The resulting nonlinear differential equations can generally be dealt with by numerical techniques, but approximate solutions can be established for our highly symmetric situation.

Changes in the index of refraction, which alter the structure of the beam wavefronts, cause changes in the beam intensity distribution as it propagates. Details of the propagation depend on a competition between diffraction and nonlinear optical delays. For materials with a positive n_2 (which includes all known transparent solids), phase delays will increase with intensity. The total change in optical path length due to phase delay, $\Delta\ell$, is written:

$$\Delta\ell = \Delta n \ell$$

where

$$\Delta n = n_2 \langle E^2 \rangle \quad , \tag{2.22}$$

ℓ = linear optical path length of material traversed.

For intensity distributions similar to a Gaussian profile, nonlinear delays will be the greatest on the axis of the beam and will decrease as the radial distance increases. This variation in optical path length across the beam will induce curvatures in the phase fronts which are opposite to the curvatures due to diffraction of the beam.

The nature of the effects of nonlinear delays on beam propagation depends on the magnitude of the nonlinearities. For relatively small nonlinearities, the beam may simply develop a slightly different beam diameter or have an altered intensity profile. Significant nonlinear delays can lead to gross fluctuations in the radial intensity distribution or possibly to catastrophic self-focusing of the beam, and self-focusing is generally accompanied by irreversible damage in the material.

There are a number of different criteria for determining at what laser intensities nonlinear processes will become important. While it is a very loose definition, it is often true that when the variation in nonlinear delays across the beam cross section is greater than the optical wavelength of the light, nonlinearities will have significant effects on propagation of the beam.

A more exacting threshold for nonlinear effects is provided by the Talanov[18] power P_1, defined as:[18]

$$P_1 \equiv \frac{c\lambda^2}{32\pi^2 n_2} \tag{2.23a}$$

For a laser beam with a Gaussian intensity distribution and a power equal to one Talanov critical power, nonlinear processes will exactly cancel diffraction effects and the beam will propagate with no long term changes in diameter or intensity profile. When the beam power significantly exceeds P_1, self-focusing of the beam will occur.

The distance that a beam can propagate before the occurrence of self-focusing is called the self-focusing distance and is labeled Z_{sf}. From the complete wave equation (Eq.(2.20)), the relationship between the total power in an optical beam and the distance Z_{sf} has been obtained numerically as:[19]

$$\left(\frac{2P}{P_1}\right)^{1/2} = 2.322 + \left|\left(\frac{ka^2}{2Z_{sf}}\right) - 0.148\right| \qquad (2.23b)$$

where

P = total beam power

a = beam $\frac{1}{e}$ radius

This relation can be used for accurate predictions of self-focusing of Gaussian beams, but there are other less accurate relations which can be used for qualitative predictions of propagation behavior. When the length of nonlinear medium ℓ is greater than the self-focusing distance Z_{sf}, the self-focusing distance is approximated by the relation (derived in Appendix 3):

$$Z_{sf} \approx \frac{a^2}{2} \frac{n_o}{\Delta n \ell} \qquad (2.24)$$

When the length of nonlinear medium is much less than Z_{sf}, the nonlinear effects are approximately equivalent to the presence of a lens in the system. Appendix 3 also demonstrates that the focal length f_{eq} of this "equivalent lens" is approximately given by:

$$f_{eq} \approx \frac{a^2}{\Delta n \ell} \qquad (2.25)$$

In practice, small scale self-focusing of high power laser beams often occurs at intensities low enough so that $\ell \approx 0.1\ Z_{sf}$. This behavior has been noticed in liquids[1] and was attributed to micro-scale distortion of the beam intensity profile. These fluctuations are believed to lead to damage in optical materials through the growth of small-scale instabilities. Speck and Bliss[20] noticed this behavior when they reported the beginning of small scale self-focusing at 1-4 GW/cm^2, while the calculated Z_{sf} at this power was at least ten times longer than the sample used.

III. EXPERIMENT

A. Introduction

The nonlinear index coefficient n_2 is an inherently difficult quantity to measure. In order to execute a meaningful measurement, it is necessary to use laser intensities which produce large optical nonlinearities in the material of interest. Unfortunately, when laser systems are operated to produce these high intensities, the resultant beams often are characterized by spatial and temporal intensity fluctuations which negate the experiments by either damaging optical materials in the system or yielding questionable results. Thus, experiments intended to determine n_2 often self-destruct before the measurement has been completed.

The laser employed in the present measurements is specifically constructed for these experiments. The master oscillator of the laser is designed to produce 1 nanosecond (ns) pulses which are temporally bandwidth limited by the uncertainty principle. The spatial filter in the system insures that the beam intensity profile also approaches the limits imposed by the uncertainty principle. Finally, the system amplifier chain is arranged to minimized intensity fluctuations due to thermally induced index of refraction variations in the laser rods.

A Mach-Zehnder interferometer is used for these measurements because the resultant n_2 determinations are directly related to the nonlinear phase delays characteristic of nonlinear propagation. The interferometer also allows the use of an experimental technique which makes possible the quick and relatively easy measurement of the nonlinearities. Thus, our experiment establishes a method for efficient determination of the nonlinear index coefficient and is applicable to a wide variety of optical materials.

B. The Laser System

Figs. 2.2 are schematic representations of the laser system used for the experiments. The laser system consists of a Nd:YAG oscillator, a pulse selector, a spatial filter and five Nd:glass amplifiers.[21]

The oscillator cavity has a plane parallel mirror configuration, with resonant reflectors used as the mirrors in order to restrict the laser bandwidth. The cavity Q is actively modulated at a frequency which matches the cavity round trip time by a Pockels cell and linear polarizier combination. Thus, while the resonant reflectors restrict the laser pulse bandwidth, the cavity Q-switch minimizes its duration. Output pulses from pulse trains produced by this oscillator have durations from 0.7 ns to 0.3 ns, depending on whether one or two longitudinal modes oscillate. When only one longitudinal mode oscillates, the time duration of the pulse ($\approx$ 0.7 ns) is the shortest that the spectral width of the pulse will allow (spectrally bandwidth limited in time). A 2mm circular aperture in the cavity restricts the transverse laser modes of the cavity.

A conventional Pockels cell, linear polarizer combination is used to select a single pulse from the oscillator pulse train. The selected pulse is spatially filtered by a lens-pinhole-lens combination with a restricting aperture at the filter input and an aperture at the filter output which passes only the central lobe of the resulting Airy diffraction pattern. The resulting laser spatial intensity profile propagates with a beam divergence angle within 50% of the minimum uncertainty angle for the finite beam diameter. Fig. 2.3 shows the Airy pattern and resulting central lobe. These points are significant because practical and interpretational difficulties associated with either amplitude or phase modulated laser beams are avoided.

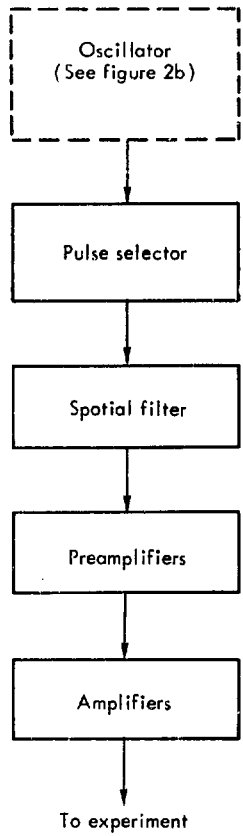

Figure 2.2a Schematic Diagram of the Laser System

This figure schematically illustrates the arrangement of the various components of the laser optical system.

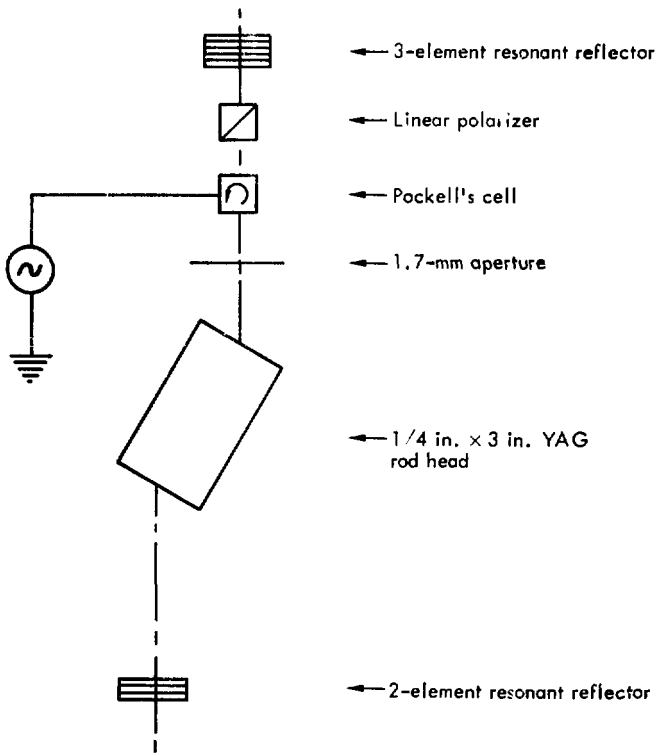

Figure 2.2b Schematic Diagram of the Laser Oscillator

This figure illustrates the physical arrangement of the individual components of the laser oscillator.

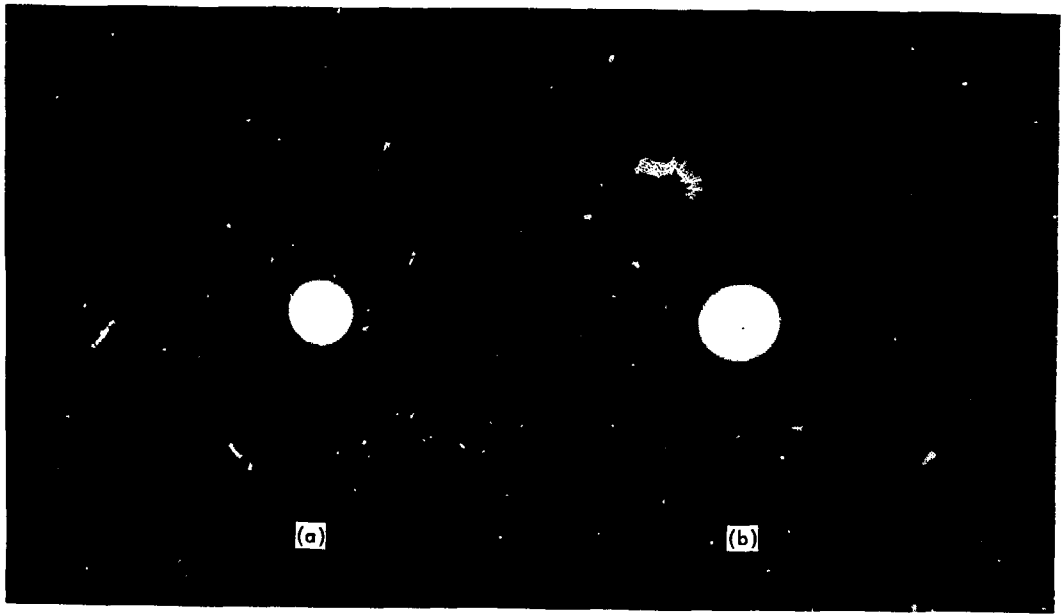

Figure 2.3 Spatially Filtered Laser Beam

Part (a) is a photograph of the Airy-type fringes of the output of the lens-pinhole-lens spatial filter. Part (b) is a photograph of the laser beam which results when the Airy pattern is apertured at the first zero of the diffraction pattern.

The laser pulse is amplified by three 3/8" x 6" Nd:Glass preamplifiers pumped by four linear flashlamps and is further amplified by two 9/16" x 9" Nd:Glass amplifiers pumped by six linear flashlamps. This abundant collection of amplifiers allows attainment of output pulse energies from the system as high as 1 joule without demanding excessive gain from the individual amplifiers. This approach avoids thermally induced index of refraction variations in the amplifier rods caused by the intense pumping necessary to achieve high gain from a single amplifier. Because of their higher gain coefficient, Nd:YAG amplifiers would be ideal for use in this system; but we find that refractive index variations in currently available rods cause spatial beam distortions which are unacceptable for the experiment. The output beam from the amplifier chain has a 1/2 intensity diameter of about 7 mm, and is then telescoped down to a 2-3 mm diameter at the entrance to the interferometer.

The spatial and temporal quality of the laser beam was carefully monitored at all stages of construction of the experiment. The temporal structure was observed with high speed streak cameras. The beam output of the spatial filter was stopped at the first Airy zero in order to avoid any possible unwanted diffraction fringes from the aperture edges. The laser beam diameter was always about 30% less than the diameter of the amplifier rods in order to prevent fringe structure caused by scattering from the rod edges.

C. The Interferometer

The effects of optical nonlinearities on laser beam propagation can be understood in terms of the optical delays that are introduced into the beam wavefronts. Thus a measurement of n_2 which is based on the observation of nonlinear phase delays is directly related to important aspects of

nonlinear propagation. A Mach-Zehnder interferometer allows the comparison of the phase delays in two different laser beams so that phase delays in an unperturbed beam can be compared with the phase delays in a beam which has propagated through a nonlinear medium. This technique for phase comparison is the basis of our nonlinear index coefficient measurement.

Fig. 2.4 is a schematic diagram of the interferometer and streak camera used for the experiments. The interferometer consists basically of two wedged glass substrates and two 50% mirrors which divide the input laser beam into the two separate beams of the interferometer and then recombines them at a slight angle after the beams have traversed equal linear optical path lengths. The output of the interferometer consists of a set of parallel straight fringes, where the spacing of the fringes depends on the wavelength of the laser and the angle of recombination of the beams. For the particular experimental arrangement used here, the two beams in the interferometer differ in intensity by a factor of about 16, but the final mirrors have reflectivities such that the intensities of the two beams are equal when they are recombined.

The streak camera used in the experiment is an LLL ultra fast streak camera[22] which is assembled from commercially available components and normally has a time resolution capability of about 10 picoseconds (ps). For our experiments, the camera is slightly modified so that the time resolution is degraded to about 13 ps. The streak camera was used to compare the linear optical path lengths of the interferometer arms with an accuracy of about 5 mm. The optical path lengths could be further compared by observing (with a normal image converter camera) interferometer

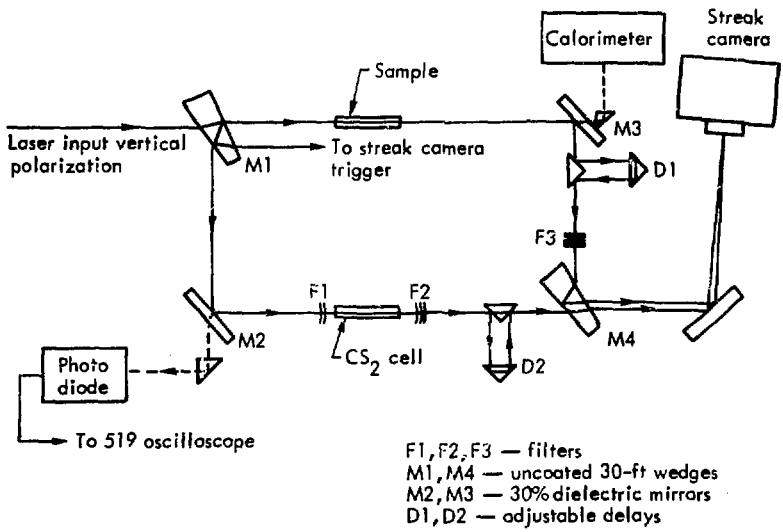

Figure 2.4 Experimental System

This figure illustrates the experimental arrangement used for the n_2 measurements. The unknown sample is placed in the high-intensity arm of the interferometer. Filters F1 and F2 are used to control the relative laser intensity in the CS_2 cell arm. Finally, the streak camera records the time-dependent Mach-Zehnder fringes from the interferometer.

fringes from a 20 ps mode locked ruby pulse, with equal path lengths indicated by a maximum in fringe contrast ratio. When the interferometer arms require optical path length adjustment, or when samples with differing optical path lengths are inserted into the interferometer, optical delay prisms in each arm are used to make the necessary adjustments.

D. Measurement Technique

Streak camera photographs of the Mach-Zehnder fringes are the raw data of the experiments. The camera photographs the time dependent intensity distribution across a 20 μm wide slit. When the interferometer beam is centered on the slit, the resulting intensity distribution consists of the Mach-Zehnder fringes. The fringe positions are sensitive to the relative optical delay between the two interferometer arms. If the optical path length, or phase delay, of one arm is changed by one half the laser wavelength, the fringes will shift by one half the fringe separation. In this way, the streak camera observation of fringe positions is used to observe time dependent changes in the relative phase delay between the two arms.

With no nonlinear samples in the interferometer, the phase delay of each arm will be constant during a laser pulse and the resultant streak camera picture will appear to be a set of straight fringes (see Fig. 2.5). If a nonlinear sample is inserted into one arm of the interferometer, the phase delay of that arm will be a function of the laser pulse intensity. Experimentally, this is observed as a curvature of the fringes on the streak photograph (see Fig. 2.6). The direction of the curvature depends on which interferometer arm contains the nonlinear sample. If identical nonlinearities are present in each arm, both arms will have equal linear

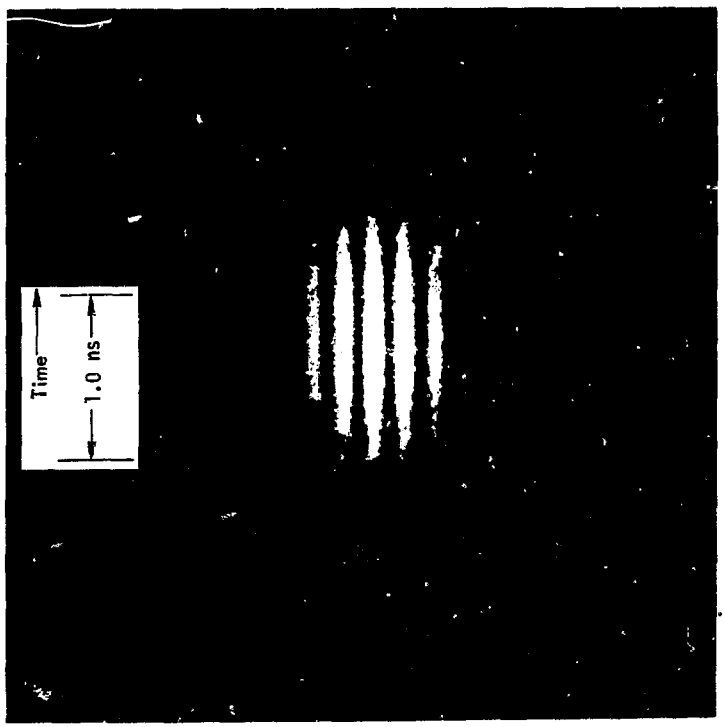

Figure 2.5 Streak Picture of Mach-Zehnder Fringes

This is a streak photograph of the time-dependence of Mach-Zehnder fringes in the absence of optical nonlinearities. Since there are no significant nonlinear optical delays in the system, the fringe positions are constant in time and the photograph shows the resulting time dependent fringes.

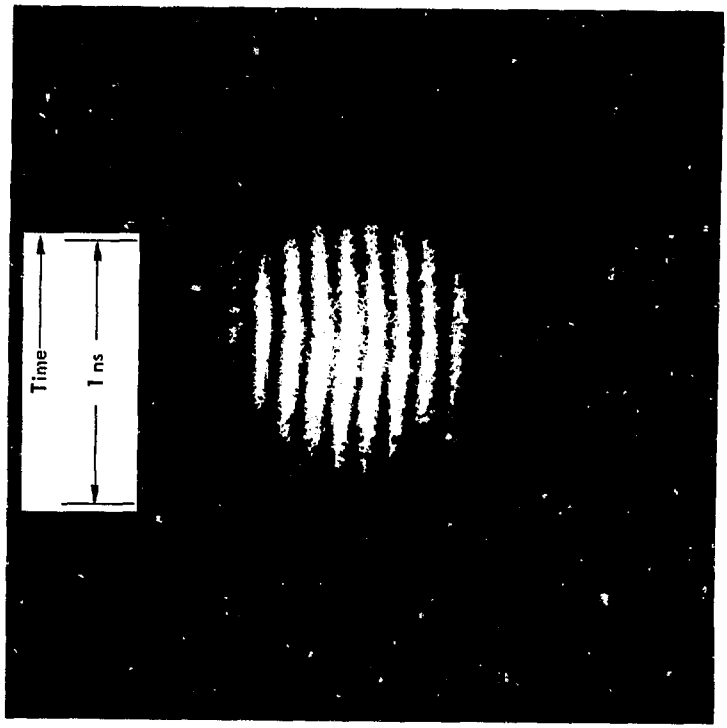

Figure 2.6 Time-Dependent Mach-Zehnder Fringes with Optical Nonlinearities

This streak picture is similar the one in Fig. 2.5, except that there is now an important al nonlinearity in one arm of the interferometer. As a result, the Mach-Zehnder fringe positions depend on the instantaneous laser intensity and exhibit the time dependent "curvature which is evident at the peak laser pulse intensity in this photograph.

and nonlinear phase delays and the streak photograph will again consist of a set of straight fringes. These changes in the curvature of the fringes are the basis of the nonlinear index measurement.

In the actual experimental arrangement, a 10 cm cell filled with CS_2 is inserted into the weak intensity arm of the interferometer (see Fig. 2.4). The sample with an unknown nonlinear index coefficient is then inserted into the high intensity arm. With both the sample and the CS_2 cell in the interferometer, the behavior of the curvature of the time resolved fringe pattern depends on a competition between the nonlinear delays in the two arms. The difference in laser beam intensity between the two arms is a factor of about 16. Appropriate attenuation with neutral density filters before and after the CS_2 cell can be used to alter the relative nonlinear delay of the two arms. Fig. 2.7 demonstrates the changes in fringe patterns associated with changes in relative intensity between the two nonlinear media. The pictures in Fig. 2.7 are taken from data for a measurement on ED-2 laser glass. In Fig. 2.7a the nonlinear delay is greater in the CS_2 cell, while in Fig. 2.7c, the delay is greatest in the ED-2 sample.

The total nonlinear path length change in a sample can be written:

$$\Delta\ell = \Delta n \cdot \ell \tag{2.26}$$

Here, $\Delta\ell$ is the effective change in optical path length due to a change Δn in the index of refraction. When the nonlinear delays are the same in both arms, the fringe positions are constant in time (as in Fig. 2.7b) and, therefore, the nonlinear path increases are the same. Under these conditions, we have:

$$\Delta\ell_{CS_2} = \Delta\ell_{sample} \tag{2.27}$$

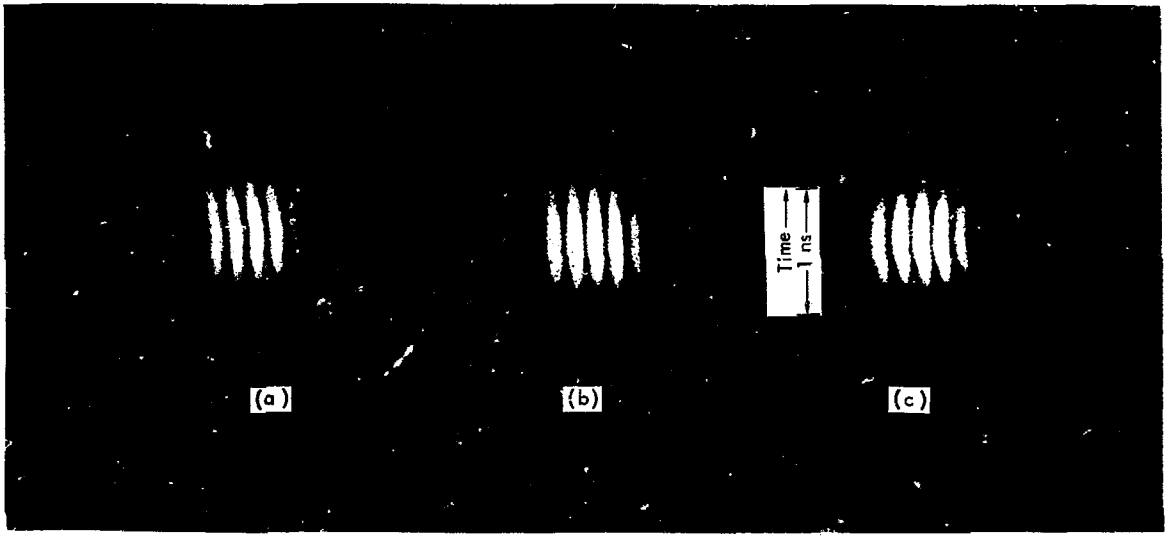

Figure 2.7 Mach-Zehnder Fringe Dependence on Optical Nonlinearities

These pictures illustrate the changes in fringe "curvatures" which accompany changes in the relative optical nonlinearities in the interferometer arms. In part (a), nonlinearities are greatest in the CS_2 arm; in part (b), nonlinearities have equal amplitudes in both arms; and in part (c), optical nonlinearities are greatest in the sample arm of the interferometer. The dark straight line in these pictures is used to accurately determine the direction of the camera "streak" and is due to a small wire on the camera slit.

or:

$$\ell_{CS_2} \cdot \Delta n_{CS_2} = \ell_{sample} \cdot \Delta n_{sample} \tag{2.28}$$

Eq. (2.28) can be used to determine the n_2 ratio of CS_2 and the unknown sample. The determination of a nonlinear index coefficient ratio is intentionally designed into the experiment. In experiments where absolute measurements are inherently difficult, a ratio measurement can often be advantageous. Ratio measurements are relatively independent of the particular experimental equipment used and should be consistent from one measurement to another; but absolute measurements will depend critically on precise absolute calibration of the experimental arrangement, which is difficult to achieve for different experimental approaches. And for comparison of the n_2's of different optical materials, ratio measurements are just as useful as absolute measurements on the same materials.

The nonlinear index coefficient ratio can be obtained from an expansion of Eq. (2.28). Using the form of n_2:

$$n_2 = \frac{\Delta n}{\langle E^2 \rangle} \tag{2.29}$$

and

$$\langle E^2 \rangle = \frac{4\pi I}{n_0 c} \quad , \tag{2.30}$$

where:

n_0 = linear index of refraction

I = instantaneous laser beam intensity.

Substituting these results, Eq.(2.28) takes the form:

$$\frac{n_2(\text{sample})}{n_2(CS_2)} = \frac{n_o(\text{sample})}{n_o(CS_2)} \left(\frac{\ell_{CS_2}}{\ell_{\text{sample}}}\right) \left(\frac{I_{CS_2}}{I_{\text{sample}}}\right) \tag{2.31}$$

Experimentally, it is desired to determine the intensity ratio $\left(I_{CS_2}/I_{\text{sample}}\right)$ for which the Mach-Zehnder fringe curvature is "null" or zero for all intensities. There are a number of experimental quantities which must be included in the determination of the "null" intensity ratio. The observed "null" condition can be written as:

$$\frac{I_{CS_2}}{I_{\text{sample}}} = \left(\frac{1}{16.25}\right) \left(\frac{1-R_{CS_2}}{1-R_{\text{sample}}}\right) \left(\frac{A_{\text{sample}}}{A_{CS_2}}\right) (\epsilon) \tag{2.32}$$

Here, 16.25 is the intensity ratio resulting from the first two interferometer mirror reflectivities. R_{CS_2} and R_{sample} are the reflection losses due to Fresnel reflections at the sample input face A_{CS_2} and A_{sample} account for changes in tensity due to changes in cross-sectional area as the beam refracts into samples with faces not perpendicular to the sample axis. Finally, ϵ is the relative nuetral density filtering required to "null" the fringe curvature.

When Eqs.(2.31) and (2.32) are combined, the resultant equation can be used to calculate the index coefficient ratio:

$$\frac{n_2(\text{sample})}{n_2(CS_2)} = \left(\frac{n_o(\text{sample})}{n_o(CS_2)}\right) \cdot \left(\frac{\ell_{CS_2}}{\ell_{\text{sample}}}\right) \cdot \left(\frac{1}{16.25}\right) \cdot \left(\frac{1-R_{CS_2}}{1-R_{\text{sample}}}\right) \cdot \left(\frac{A_{\text{sample}}}{A_{CS_2}}\right) (\epsilon) \tag{2.33}$$

One material which we examine (lucite) has a significant 1 μm absorption cross-section and required an additional correction in Eq. (2.33). This is because the absorption cross-section leads to a reduction of the laser intensity as it propagates. This correction can take the form of a substituted "effective" length[23] for the sample length ℓ_{sample}. To see this, observe that the nonlinear path length change in the sample is:

$$\Delta\ell \approx \int_0^{\ell} |E(z)|^2 n_2 dz \tag{2.34}$$

This can be approximated by:

$$\Delta\ell \approx n_2 |E|^2 \int_0^{\ell} e^{-\alpha z}\, dz \quad , \tag{2.35}$$

where we have assumed $|E^2(z)| \approx |E^2|\, e^{-\alpha z}$ and α is the 1 μm absorption cross-section. The integral can be evaluated and yields:

$$\Delta\ell \approx \frac{-n_2 |E|^2}{\alpha} (1 - e^{-\alpha\ell}) \tag{2.36}$$

For $\alpha = 0$, Eq. (2.36) becomes identical to Eq. (2.22), which we have used previously. For $\alpha \neq 0$, Eq. (2.36) can be written in the form

$$\Delta\ell = n_2 |E|^2 \ell' \quad , \tag{2.37}$$

where:

$$\ell' \equiv \left(\frac{1 - e^{-\alpha\ell}}{\alpha} \right) \tag{2.38}$$

This equation has the same form as Eq. (2.22), but contains an equivalent length ℓ'. The effects on nonlinear propagation of the absorption cross-secion α can be approximately corrected for by substituting ℓ' for ℓ_{sample} in Eq. (2.33).

There are two possible procedures for performing the ratio measurement. The first approach is to use neutral density filters to adjust the relative intensities in the interferometer arms until the fringe curvature is "nulled." The nonlinear index can then be evaluated. This method has two major disadvantages. First, it would be very tedious and time consuming to search for the appropriate combination of filters which would null the fringe shifts. Secondly, since the filters are not continuously variable, there could be situations where no available combination of filters would null the fringes to within the streak camera resolution.

The second approach is to measure the observed fringe shifts when filters are used to vary the relative intensity in the CS_2 cell and the sample. The fringe shift is then plotted as a function of relative intensity. For a pure n_2 nonlinearity this plot will be a straight line and the point at which the graph intersects the intensity axis (zero fringe curvature) will establish the "null" intensity ratio. Data of this type used for the determination of the n_2 of ED-2 is shown in Fig. 2.8. The line was established by using a least squares fit to the data points. This measurement procedure is not subject to the limitations of the first method and can make full use of the experimental resolution capability.

Since both nonlinear elements have an instantaneous response and both interferometer arms have the same pulse history, it is not necessary to measure the absolute laser intensity to determine the n_2 ratio. Only

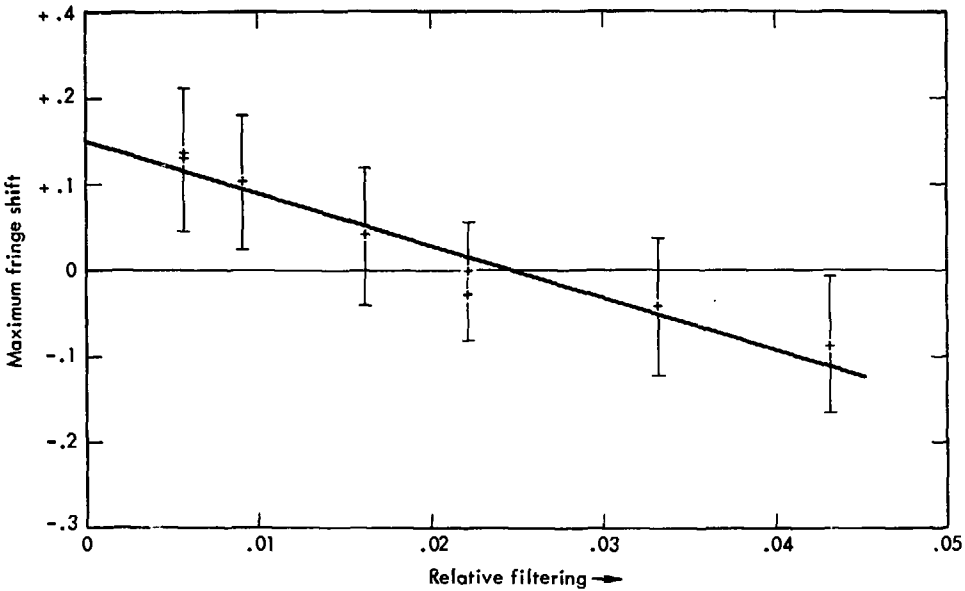

Figure 2.8 Relative Fringe Shifts vs. Relative Filtering of Interometer Arms

Here, the relative amplitude of the Mach-Zehnder fringe shifts (or fringe curvatures) is plotted as a function of the relative filtering of the laser intensity in the interferometer arms. The value of relative filtering which is associated with zero, or "null," fringe shift is the experimental result which is used to determine the nonlinear index ratios.

the relative pulse energies need be determined. The pulse energy ratios are determined using two LLL Gunn-type calorimeters[24] (good to ∿1%), and previously calibrated neutral density filters (good to ±5%). The filters are calibrated at 1.06 μm with a Cary spectrophotometer[25] and are used where the laser beam intensity was sufficiently low so that the filters respond as linear attenuators(which is also verified by calorimetry). In order to compare data on different laser shots, as in Fig. 2.8, it is necessary to normalize all plotted data to the same relative peak laser intensity, since the fringe shift is a function of both the relative and absolute laser intensity. We find that Tektronix 519 oscillograms[25] (system response ∿0.4 ns) are sufficiently accurate for this purpose.

The accuracy of our experiment improves as the amount of nonlinear phase delay occurring in the samples increases. But there are several considerations which impose an upper limit on the amount of phase delay that can be used. A major limitation is imposed by self-focusing phenomena. Self-focusing destroys the phase coherence of the laser pulse and no information can be obtained from the streak picture. To estimate this limitation, we use the relation (see Appendix 3)

$$Z_{sf} \approx \left(\frac{a^2}{2}\right) \frac{n_o}{\Delta \ell} \tag{2.24}$$

to find that $\Delta \ell \sim 1.5$ μ when the beam self-focuses at the end of a 10 cm sample.

The advantage of large diameter beams is obvious here because of the a^2 dependence of Z_{sf}. For a given sample length, doubling the beam diameter would allow four times the nonlinear phase delay, and would have

an associated increase in experimental accuracy. The maximum diameter of the beam is limited by the final amplifier rod diameter. In order to avoid nonlinear processes in the final amplifier, but still have sufficient intensity in the interferometer to observe nonlinear delays in glasses, it is necessary to reduce the beam diameter with a telescope at the interferometer input. With an ∿8 mm FWHM beam diameter at the laser output, we find that telescoping down to 3 mm is a convenient compromise.

As further evidence of our excellent beam quality, we are able to observe more than 0.5 λ phase delay in the interometer without the onset of self-focusing. Our consistent excellent fringe contrast ratio indicates that small scale self-focusing is not a factor in our experiments. Whole beam self-focusing can also be detected as a loss of fringe contrast ratio, but has never been observed during the experiments.

IV. EXPERIMENTAL RESULTS AND DISCUSSION

A. Introduction

Our results include data from several different experiments. We present the measured nonlinear index ratios relative to CS_2 for a number of laser system related materials. Due to our excellent laser beam quality, we are also able to observe details of nonlinear propagation in the absence of self-focusing. In the low intensity regime where optical nonlinearities are small, nonlinear propagation is adequately described by the "thin lens" analysis in which the effects of a nonlinear media are approximately by an ordinary lens. We observe both "thin lens" nonlinearities and nonlinear propagation at higher intensities where the nonlinearities are large enough so that the "thin lens" analysis is inadequate. These additional studies of nonlinear propagation are important because they establish experimental limitations on the nonlinear index ratio measurements and also because they relate directly to nonlinear propagation considerations in high power laser systems.

The nonlinear index measurements are performed on both active and passive optical materials related to laser systems. The active materials include several Nd:glass, Nd:YAG and ruby laser rods. The passive materials include SF6 Faraday rotator glass and lucite. The variety of materials measured demonstrate the versatility of our technique. For Nd-YAG and SF6 glass, the nonlinear index coefficient n_2 is large enough that we are able to perform the measurement with both linear and circular polarization. The measurement on lucite was executed in spite of a considerable absorption cross-section at 1.06 μm by using the analysis described above.

The "thin lens" analysis is a very useful technique for describing the effects of small nonlinearities. Fig. 2.9 demonstrates the use of the technique. In Fig. 2.9a an intense laser beam with initially plane wavefronts traverses a nonlinear medium of thickness ℓ. When the beam emerges from the medium, its intensity profile and the optical nonlinearities have induced spherical wavefronts in the beam and it will focus at a distance Z_f from the sample exit. Fig. 2.9b shows that the same behavior occurs in linear optical propagation when a lens with focal length f equal to the distance Z_f is inserted into the beam. Thus, characteristics of nonlinear propagation in Fig. 2.9a are approximately described by the behavior of the linear system in Fig. 2.9b.

When nonlinearities are small, the wavefronts induced in Fig. 2.9a will be approximately spherical. But with larger optical nonlinearities the wavefront distortions will probably no longer be spherical and the thin lens description will not describe the propagation behavior. This is because the distorted wavefronts will not lead to a well defined Z_f and may also result in gross perturbations in the beam intensity profile.

Our excellent temporal and spatial beam quality allow the detailed observation of nonlinear propagation effects both in the thin lens limit as well as at intensities where nonlinearities become large. At higher intensities, and in the absence of self-focusing, we observe novel and previously unobserved nonlinear behavior in which the time coherence of the laser pulse appears to be completely destroyed while the spatial coherence across the beam is maintained. A number of preliminary experiments intended to investigate this behavior are performed, but the fundamental interaction responsible is not identified.

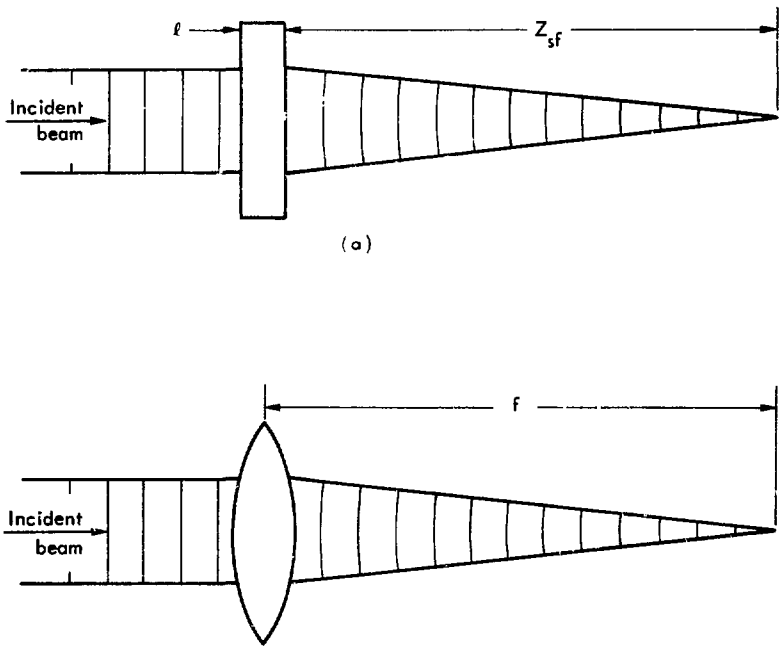

Figure 2.9 Equivalent "Thin Lens" Systems

Part (a) illustrates the behavior of a nonlinear "thin lens" system consisting of a piece of nonlinear optical media with an effective self-focussing focal length Z_{sf}. Part (b) shows the similar behavior associated with a linear optical system consisting of a "thin lens" with focal length f.

B. Nonlinear Propagation Without Self-focusing

In the limit of small optical nonlinearities the characteristics of nonlinear propagation can be predicted by the thin lens analysis described above. The thin lens analysis is useful because it allows a simple, well understood linear optical system to be used to describe the behavior of a complicated nonlinear propagation situation. However, with large optical nonlinearities, this approach is not adequate and more flexible descriptions of light propagation must be used.

For laser beams in a nonlinear medium which have constant spatial and temporal intensity distributions, the equivalent thin lens system has a single, constant equivalent focal length f_n, where f_n is approximately given by the relation (see Appendix 3):

$$f_n \approx \frac{a^2}{\Delta \ell} = \frac{a^2}{n_2 \langle E^2 \rangle} \tag{2.39}$$

But for pulsed laser beams, the focal length f_n of the equivalent thin lens system will depend on the instantaneous intensity, and both f_n and $|E|^2$ will be time dependent. The time dependent focal length $f_n(t)$ of Eq. (2.25) can be used to predict the chacteristics of nonlinear propagation when optical nonlinearities are small.

In order to verify these predictions, we use the experimental arrangement of Fig. 2.10. The camera is placed in the laser beam at a distance beyond the CS_2 cell which is less than the minimum focal length of the equivalent thin lenses for the nonlinear system. The camera is used to observe the time dependent radial intensity profile of the intermediate field of the laser beam into and out of the CS_2 cell.

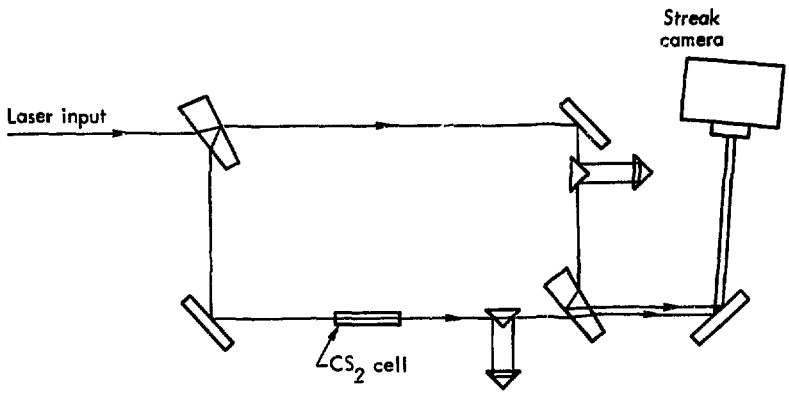

Figure 2.10 Experimental Arrangement Used for Observation of Nonlinear Optical Propagation Behavior

This system is a simplified version of the system used to measure nonlinear index ratios. The major difference here is that the two beams do not overlap to produce interference fringes.

Fig. 2.11 shows a typical resulting streak photograph. The input pulse shows the expected time dependent radial intensity profile, but the output pulse shows markedly different behavior. At the early and late portions of the laser pulse the intensity is relatively low, and the equivalent thin lens focal lengths are effectively infinite so that the resulting output pulse intensity profile is similar to that of the input pulse. But at the pulse peak intensities, the equivalent thin lens focal lengths decrease from infinity and approach the streak camera position, resulting in the observed narrowing of the radial intensity profile.

As the laser pulse intensity increases, the wavefront distortion increases and the equivalent thin lenses for the system have decreasing focal lengths. However, when the maximum nonlinear path length increase exceeds one laser wavelength, the wavefront distortions may no longer be spherical, and the thin lens analysis may not be applicable to the system. This is because linear optical lenses induce spherical wavefront distortions, and large optical nonlinearities induce wavefront distortions which are determined by the laser intensity profile. Only a very specific intensity profile will lead to spherical wavefront distortions in the presence of large optical nonlinearities. Thus, for large nonlinearities in the absence of self-focusing, the thin lens analysis is inadequate and nonlinear propagation characteristics are expected to differ from the case where nonlinearities are small and the thin lens analysis applies.

Fig. 2.12 shows a streak photograph of the input and output laser pulses from a CS_2 cell with large optical nonlinearities. The pulse energy in this case is about eight times greater than for the pulse

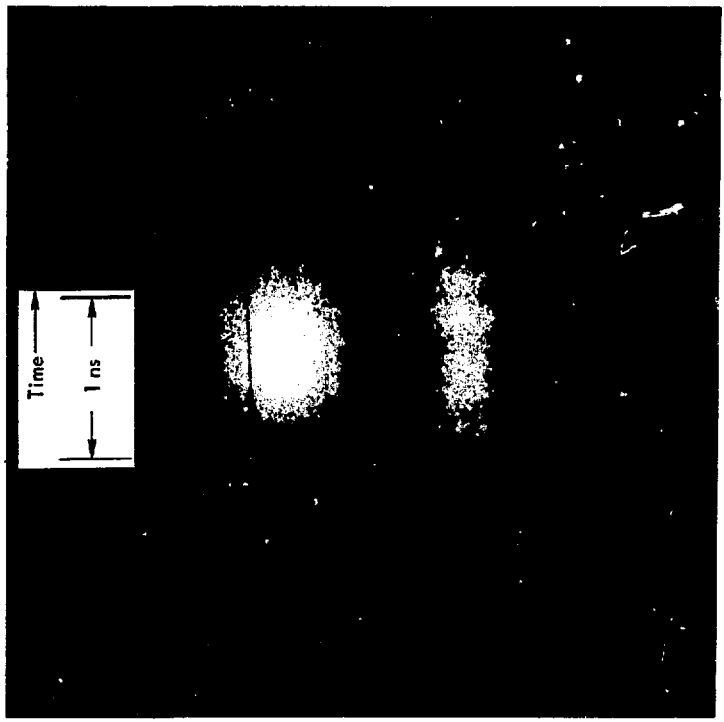

Figure 2.11 Near-Field "Thin Lens" Effects

This is a streak photograph of the input and output pulses from the CS_2 cell. The input pulse shows the expected spatial and temporal behavior. The output pulse is seen to be spatially narrowed, or focused, at the intense portion of the pulse due to the intensity-dependent "thin lens" behavior of the CS_2 cell.

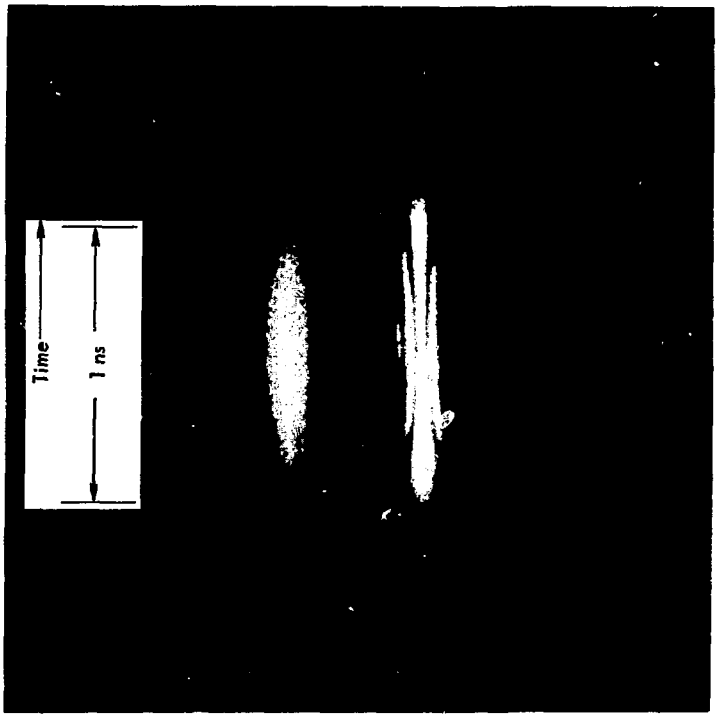

Figure 2.12 Optical Nonlinearity-Induced Beam Fringes

This streak photograph shows the time-dependent fringes which can be induced in a beam without the occurrence of catastrophic self-focussing. The number of fringes across the beam depends on the instantaneous laser pulse intensity. For this pulse, the fringes at the peak pulse intensity indicate the presence of nonlinear delays of about 5 wavelengths of the light.

of Fig. 2.11. In order to avoid self-focusing at these intensities, we impose a nearly 30 milliradian divergence on the beam at the entrance to the CS_2 cell. Fig. 2.12 demonstrates that large optical nonlinearities lead to propagation behavior which cannot be described by the thin lens analysis. The output pulse in Fig. 2.12 has acquired fringes in the radial intensity profile, with the number of fringes increasing with the instantaneous laser pulse intensity. At the low intensity extremes of the output pulse, the intensity profile is similar to that of the input pulse, as in Fig. 2.11. But at the peak pulse intensity there are seven or eight fringes across the beam cross section. A two dimensional streak picture corresponding to Fig. 2.12 would show the development of near-field Fresnel-type circular fringes in the intermediate field of the beam, with the number of fringes increasing with the instantaneous intensity.

Although a thin lens analysis will not explain the propagation behavior in Fig. 2.12 an alternate description of pulse propagation can be used to understand the origin of the fringing behavior. Rather than viewing pulse propagation as movement of light in the z-direction at the speed of light, propagation can also be expressed as the time dependent interference pattern due to the beam wavefronts and intensity profile from a plane at $z = 0$ (CS_2 cell exit) and $t = 0$. This description of light propagation can be derived from the integral representation of Maxwell's differential wave equation (Eq. (2.20). Both representations are equally valid, but they have differences in interpretation which make them convenient for different situations. For propagation of a diffraction limited laser pulse, the interference representation describes the beam as a time dependent distribution of constructive interference patterns, with the region of constructive

interference moving in the z-direction with the characteristic velocity $(\frac{c}{n_0})$. For nonlinear propagation, this approach determines the characteristics of propagation through the time dependent behavior of constructive interference of the perturbed beam wavefronts and intensity profile.

For the situation of Fig. 2.12, the wavefront distortion consists of a continuous variation (of up to ~5 wavelengths) of nonlinear delay across the beam cross section. As the beam propagates, the intensity profile is determined by the interference of the perturbed wavefronts. The fringes result from the interference properties of the beam wavefronts in a manner similar to the fringing associated with multiple slit diffraction patterns. Fig. 2.13 illustrates this analogy. In Fig. 2.13a, path length differences from the different slits result in the characteristic fringe patterns. When the path length differences between adjacent slits are an integral number of wavelengths, constructive interference occurs. In Fig. 2.13b, interference between different regions of the beam lead to fringes in the radial profile of the propagated beam.

For the pulse in Fig. 2.12, as the beam exits from the CS_2 cell (at $z = L$) its intensity profile is probably still nearly Gaussian, but the wavefronts are no longer spherical because of the large nonlinear path lengths in the sample. As the beam propagates, the intensity profile will develop fringe structure. The development of fringes can be understood with the help of Fig. 2.13b. As the beam propagates from $z = 0$; the radial profile develops fringes due to the constructive and destructive interference of the light wave amplitudes with different phases at $z = 0$; much in the same way as fringes result from an n-slit diffraction grating. As the beam propagates further, the contrast ratio of fringes will decrease and the beam will eventually acquire a divergence angle $\Delta\theta$ of roughly:

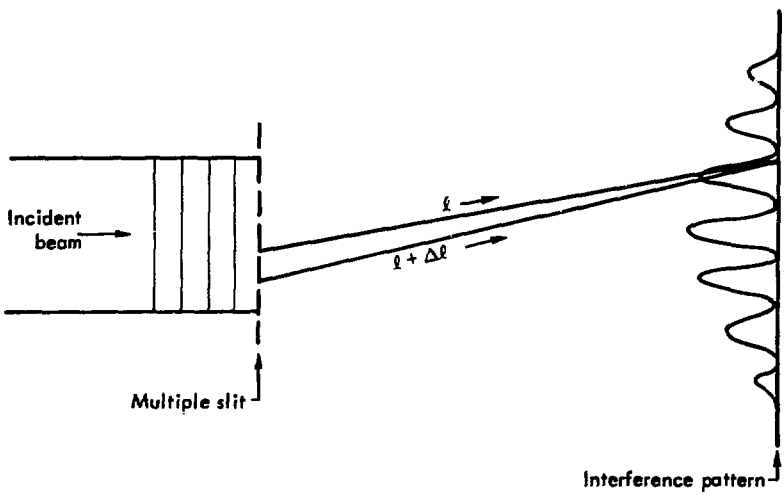

Figure 2.13(a) Multiple-Slit Diffraction Pattern

This figure schematically illustrates the behavior associated with N-slit diffraction systems. Here, differences in path lengths from different slits to the observation point result in the characteristic interference pattern.

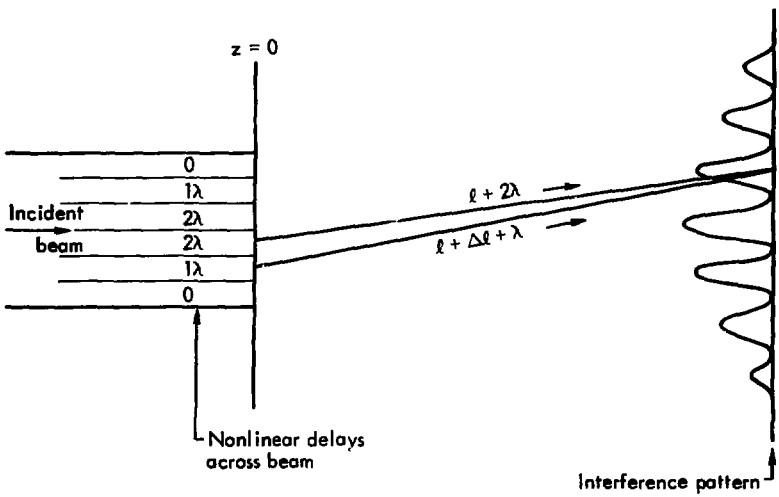

Figure 2.13(b) Interference of Nonlinear Delays

This figure schematically illustrates the interference of nonlinear delays in a manner which is suggestive of multiple-slit diffraction systems. Here, the differing nonlinear delays across the beam result in constructive and destructive interference as the beam propagates.

$$\Delta\theta \approx \frac{\lambda}{\Delta r} \tag{2.40}$$

where Δr is a characteristic radial width of constant phase regions of the beam at $z = 0$. The number of fringes in the beam will be roughly twice the number of wavelengths of nonlinear path length change across the beam cross section. After the beam exits from the CS_2 cell, the fringes will first develop at a distance characterized by the length:

$$L = \frac{\Delta\theta}{\Delta r} = \frac{\lambda}{\Delta r^2} \tag{2.41}$$

The above description of these nonlinear propagation effects are necessarily qualitative because the precise behavior of the beam will depend on details of the beam intensity profile and the nonlinearities in the CS_2 cell. It should be emphasized that it is not only the wavefront distortions which determine the propagation behavior, but also the relative intensities associated with these distortions; because the intensities will determine the relative importance of the contribution of the distortions to the interference pattern. Thus, the above description of nonlinear propagation can only be used as a qualitative guide for describing effects which will be expected to occur in nonlinear propagation.

In the limit of small optical nonlinearities, the interference description gives the same results as the thin lens analysis. For Fig. 2.11 the thin lens analysis correctly predicts the narrowing of the beam radius at high pulse intensities. The peak nonlinear path length increase for the pulse in Fig. 2.11 is about one-half wavelength. The interference description of pulse propagation for a peak nonlinear path increase of one-half wavelength would predict about one fringe across the beam peak intensity. This is precisely the case in Fig. 2.11

where the "narrowed" portion of the beam can also be viewed as one fringe across the beam, with destructive interference being responsible for the apparently narrowed beam diameter. At higher intensities, this destructive interference "moves" toward the center of the beam. Fig. 2.12 is an example of the behavior in the high intensity regime of this process.

C. Anomalous Temporal Behavior

While using the experimental arrangement of Fig. 2.10 for the propagation studies described above, we sometimes observe a random structure in the time dependence of the pulse transmitted through the CS_2 cell. This effect has not been previously observed and is not understood. Figs. 2.11 and 2.12 both show traces of this effect, but Fig. 2.14 demonstrates it clearly. In Fig. 2.14a the input pulse shows the usual time dependent intensity profile, but the output pulse is characterized by considerable temporal structure. The spatial integrity and expected "lensing" of the beam show that self-focusing has not occurred in the CS_2 cell. In Fig. 2.14b the pulse energy is increased by an order of magnitude and the output pulse has self-focused. The occurrence of self-focusing is established by the observation of the expected accompanying Raman scattered light from CS_2. It is interesting that roughly the same intensity is transmitted in both cases, in spite of a pulse energy difference of a factor of ten.

A characteristic of this effect is that the spatial coherence of the laser pulse is retained while its temporal coherence is apparently destroyed. Fig. 2.15 shows a streak photograph with the transmitted pulse expanded across the entire camera slit. Although the pulse has

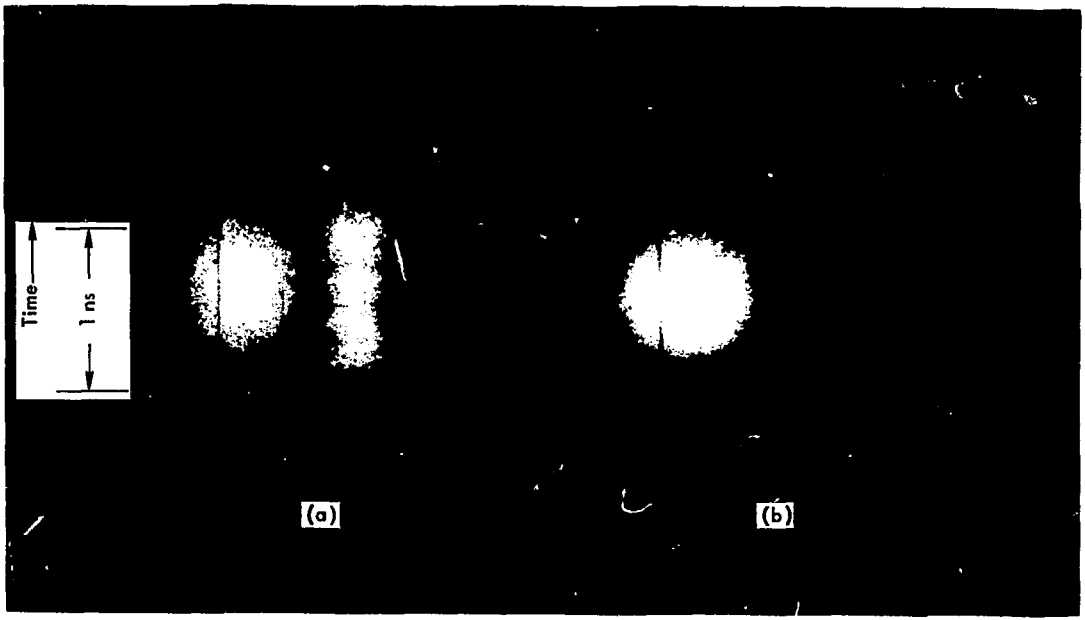

Figure 2.14 Anomalous Temporal Behavior in a CS_2 Cell

In part (a), the beam exiting from the CS_2 cell exhibits temporal structure which is not present on the input pulse. This occurs in the absence of catastrophic self-focussing. In part (b), higher laser intensity leads to catastrophic self-focussing and a drastically altered output pulse from the CS_2 cell.

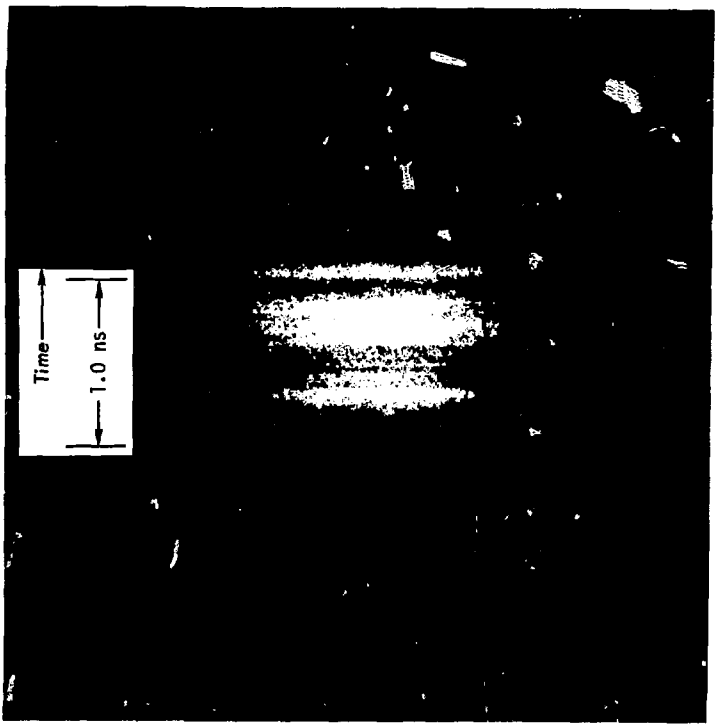

Figure 2.15 Anomalous Temporal Behavior

Here, an output pulse (from the CS_2 cell) which has acquired strong temporal fluctuations is expanded across the entire streak camera slit. This picture emphasizes the spatially coherent nature of the temporal structure.

time structure as fast as the resolution of the camera (~13 psec), the structure occurs simultaneously across the entire pulse cross section. In fact, the nonuniformity of the streak camera sweep rate across the slit can be observed with this picture. For an alternate view, Fig. 2.16 shows the Mach-Zehnder fringes associated with these pulses. Although the photograph is overexposed, it still demonstrates the spatial phase coherence of the pulse during its temporal break-up.

The exact conditions necessary for observation of this effect are not known. The random temporal structure seems to occur most frequently when the beam transmitted through the CS_2 cell is slightly diverging. A number of experiments have been performed in an attempt to isolate the interaction responsible for this effect; but no definite conclusions have been reached. By carefully monitoring in the forward and reverse directions the amplitude of Raman scattered light associated with self-focusing, we have established that the anomalous time behavior occurs at intensities as low as an order of magnitude below the self-focusing threshold. We have also observed this effect in a Schott SF-6 Faraday rotator glass rod, but the threshold energy for observing the effect was higher than in CS_2 by roughly the ratio of their nonlinear indexes.

When the anomalous behavior occurs, we have observed that significant amounts of light at essentially the laser frequency (up to ~15% of the pulse energy) are scattered in the reverse direction. Examinations of streak pictures of the forward and reverse scattered light from a pulse suggest that the reverse scattered light has temporal structure which is complementary to the structure of the forward transmitted pulse. Owyoung[17] has observed some behavior qualitatively similar to our observations and has attributed the effect to Brillouin

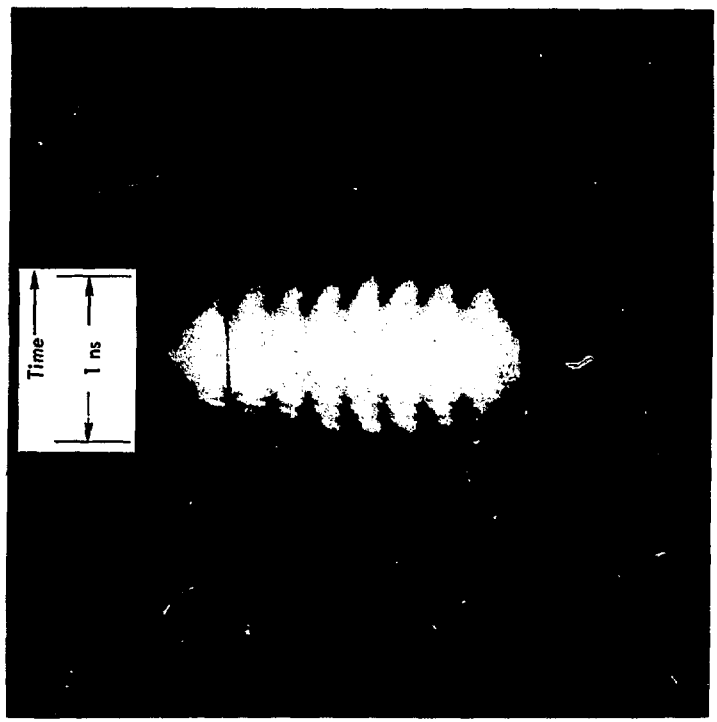

Figure 2.16 Mach-Zehnder Fringes of Anomalous Temporal Behavior

This picture, which was recorded under conditions very similar to those used for Fig. 2.15, further emphasizes the coherent nature of the temporal structure. Here, the input and output beams from the CS_2 cell are combined to give Mach-Zehnder fringes. Although the photograph is overexposed, the leading edge of the pulse clearly demonstrates the simultaneous onset of the temporal fluctuations across the beam cross section.

scattering. Unfortunately, our spectrometer resolution (~0.3 Å) is insufficient to resolve the expected Brillouin shift in CS_2 (~0.1 Å).[26]

In spite of the lack of understanding of this effect, we are always able to avoid it when performing nonlinear index ratio measurements. This is possible because the laser intensity is routinely reproducible to an accuracy of ±20%.

D. Nonlinear Index Coefficient-Measurements

The primary purpose for the present experiments is to determine the nonlinear index coefficient n_2 for optical materials related to high power laser systems. Our results represent the most general nonlinear index coefficient measurements reported to date. We perform measurements on both crystalline and amorphous materials and also on a collection of glasses with well specified differences in composition. In some cases, we are able to perform the measurements with both linearly and circularly polarized laser beams. The results of these measurements are important because they supply precisely the kind of information needed for current studies of the nonlinear optical characteristics of laser system related materials.

The experimental apparatus can be used for determining either absolute values of the nonlinear index coefficient n_2 or the ratio of n_2's for two different materials. All of our nonlinear index measurements are made relative to the n_2 of CS_2. The ratio method was chosen because it allows major experimental simplifications, such as obviation of absolute intensity measurements of the laser pulses used for the measurements. Some other advantages of ratio measurements have been mentioned previously. The nonlinear index coefficient ratios are determined from direct measurements (with the ultra-fast streak

camera and Mach-Zehnder interferometer) of nonlinear optical path length changes in the materials of interest. The measured path length changes are converted to nonlinear index coefficient ratios with the analysis described above.

These measurements are the first reported determinations of nonlinear index ratios. In order to compare our results with measurements by other workers, it is useful to be able to convert our relative measurements to absolute values for the nonlinear index coefficient n_2. The absolute value of the n_2 of CS_2 can be used to make this conversion; but, unfortunately, no definitive absolute measurement of the n_2 of CS_2 has been made with 1.06 μm light. While there have been several measurements of the n_2 of CS_2,[12,27] these measurements have been performed with light wavelengths different from 1.06 μm. Measurements[12] on CS_2 with 546 mm and 633 mm radiation have determined the n_2 to be $1.24 \cdot 10^{-11}$esu and $1.17 \cdot 10^{-11}$esu at the respective wavelengths. Thus, dispersion of the nonlinear index is sizeable and must be accounted for. In order to avoid unknown errors due to the dispersion of n_2, we use the data of Speck and Bliss[11] to estimate the n_2 of CS_2 at 1.06 μm to be approximately $1.1 \cdot 10^{-11}$esu. We then use this number with the measured nonlinear index ratio to estimate absolute values for the n_2 of materials we measure.

The results of our measurements are summarized in Table 2.1. The results presented in this table are not the raw data. Measured nonlinear path length changes for the various materials have been converted to nonlinear index ratios by using the appropriate forms of Eq. (2.33). In order to obtain estimated absolute n_2 values, the nonlinear index coefficient ratios are multiplied by $1.1 \cdot 10^{-11}$esu.

TABLE 2.1

Results of n_2 Measurements

Sample	Laser Polarization*	n_o	$\frac{n_2(\text{Sample})}{n_2(CS_2)}$	$n_2(\text{Sample}) \times 10^{13}$** (Estimated)
CS_2**		1.62	1.0	110. ± 33
ED-2†	V	1.55	.0139 ± .0017	1.53
C835††	V	1.50	.0166 ± .0017	1.83
C1020††	V	1.50	.0016 ± .0018	1.83
C2828††	V	1.53	.0184 ± .0018	2.08
YAG***	V	1.83	.0315 ± .003	3.47
YAG	C	1.83	.0253 ± .0035	2.78
SF_6†††	V	1.77	.032 ± .009	9.0
SF_6†††	C	1.77	.051 ± .005	5.6
RUBY	V	1.76	.0135 ± .0013	1.48
Lucite	V	1.49	.025 ± .0045	2.74

* V = Vertical, Linear; C = Circular

** n_2 of CS_2 determined by using independent measurement of n_2 of ED-2 glass by Speck and Bliss[11] with our ED-2 measurement, with a resulting uncertainty of ±30%.

† Manufactured by Owens Illinois

†† Manufactured by American Optical

*** Measurement performed with beam propagating along (111) axis with optical electric field vector 45° from (01-1) axis.

††† Manufactured by Schott Optical

As mentioned above, the value of $1.1 \cdot 10^{-11}$ esu for the n_2 of CS_2 was determined from the absolute n_2 measurements of Bliss.[11] Their measurements were time resolved interferometric n_2 determinations with a technique similar to our own. While Bliss did not measure the n_2 of CS_2, they did measure the n_2 of ED-4 laser glass with a 1.06 μm laser. ED-4 and ED-2 are identical glasses, except that ED-2 is doped with about three weight percent of Nd_2O_3; and both glasses should have identical n_2's at 1.06 μm. By using our measurement of $n_2(\text{ED-2})/n_2(CS_2)$ to be 0.0139 and Bliss's measurement of the n_2 of ED-4 to be $1.53 \cdot 10^{-13}$ esu, we estimate the n_2 of CS_2 to be $1.1 \cdot 10^{-11}$ esu at 1.06 μm. While this estimation has considerable uncertainty (~±30%), we feel that it is better than the unknown errors possible from estimating the n_2 of CS_2 at 1.06 μm with n_2 data from measurements at other wavelengths.

The typical error quoted for the nonlinear index ratios is about ±10%. The error is due mainly to normalization of the raw data to the same peak laser intensity and to the limited spatial resolution of the streak camera. With ≥5 lines per millimeter resolution, a 25 mm slit, and 6 fringes across the slit, we are limited to about 25 resolution points between fringes at a single point in time.

When the streak photographs of the Mach-Zehnder fringes are analyzed, a color contour neutral density representation of the fringes is used to measure the fringe curvature. By using microdensitometry with the color contour representation, we are able to detect a shift in fringe position as small as 1/30 of the fringe separation. This is accomplished by enhancing the signal to noise ratio through scanning several neighboring positions in the streak direction (equivalent to comparing fringe positions at neighboring positions in time) and taking advantage of the expected fringe symmetry.

For most of the measurements represented in Table 2.1, the overall nonlinear path lengths being compared amounted to about 1/3 wavelength, corresponding to a fringe shift of 1/3 fringe separation. This nonlinear phase delay together with our 1/30 of a fringe resolution capability are major contributions to the 10% quoted accuracy of the experiment. The accuracy is somewhat improved during analysis of the data by using a least squares fit to the data to determine the "null" intensity, as in Fig. 2.8.

There are several features in the experiment which could possibly contribute to the experimental error. These features include considerations such as the accuracy of our measurement of the interferometer mirror reflectivities (good to 1%) or the determination of the neutral density filter transmissivities (good to a few percent). Because of our excellent diagnostic facilities, we feel that these contributions to the experimental error are not significant.

Although it is also a small source of experimental error, practical limitations on laser beam alignment at the streak camera slit should also be mentioned. This error arises because when the beams are not exactly superimposed, the Mach-Zehnder fringes will be comparing phase delays from different portions of the intensity profile of the two interferometer beams. This situation would shift the fringe positions and could lead to erroneous results.

This last source of error is related to another subtle advantage of performing ratio measurements rather than absolute measurements of n_2. This advantage, which has to do with nonlinear propagation characteristics, is explained as follows. The most critical part of the ratio measurement

occurs when the interferometer arms' intensities are adjusted so that the nonlinear delays are nearly the same in both arms. Under these conditions, the laser beam experiences identical linear and nonlinear path lengths and the Mach-Zehnder fringe shifts are "nulled." If the optical nonlinearities lead to changes in the beam intensity profile at the streak camera slit (and they usually do), then both interferometer beams will exhibit identical changes at the slit and the Mach-Zehnder fringes will maintain their optimum contrast ratio.

However, for an absolute n_2 measurement with a nonlinear sample in only one interferometer arm, only one of the interferometer beams will experience nonlinear delays. This difference between the two beams can cause changes in the behavior of the Mach-Zehnder fringes. This is especially true if there is some slight asymmetry in the laser beam intensity profile. An asymmetric intensity profile could cause actual displacement of the interferometer alignment for the absolute n_2 measurement. This would not occur for a ratio measurement where both interferometer arms experience the same nonlinear optical perturbations.

Since the fringe shift resolution of the experiment is always the same, experimental accuracy increases directly as the amount of nonlinear delay which can be used in the experiment increases. Thus, it is desirable to operate the laser at the highest powers possible without damaging the experimental apparatus or generating undesirable nonlinear behavior in the experiment. We are able to avoid the undesirable nonlinear effects described above because the laser intensity is routinely reproducible with an accuracy of ±20%. Under these conditions, we find 1/3 of a wavelength of nonlinear path length increase to be a convenient operating point for the measurements.

Avoiding undesirable nonlinear behavior is simplified by examining the streak camera pictures to insure their absence. The presence of anomalous time behavior is easily observed on the streak pictures. Self-focusing can also be readily detected. When self-focusing occurs, the spatial phase coherence of the laser beam is destroyed. On the streak pictures, the loss of spatial coherence is identified by a drastic reduction or destruction of the Mach-Zehnder fringe contrast ratio. Fig. 2.17 shows the time resolved Mach-Zehnder fringes for a pulse which self-focuses at its peak intensity. The photograph clearly demonstrates the resultant loss of fringe contrast ratio at the pulse peak intensities.

E. Nonlinear Index Coefficients - Discussion

Detailed measurements of the nonlinear index of refraction coefficient n_2 are needed to specify characteristics of optical nonlinearities in optical materials. This information is needed both to provide design specifications for the materials and to supply data for verification of theoretical predictions of the behavior of optical nonlinearities.

The results of our nonlinear index coefficient measurements are summarized in Table 2.1. For convenience in the following discussion, these results will be discussed in terms of the estimated n_2 values,rather than the n_2 ratios. While the number of materials we measure is not exceedingly large, the variety of conditions and materials in our experiments can be used to illustrate several different aspects of optical nonlinearities. Four different silicate glass laser rods (see Table 2.2 for the glass compositions) are included in our samples and can be used to study the composition dependence of n_2. For two of our samples the optical nonlinearities could be measured with both

Figure 2.17 Mach-Zehnder Fringes With Self-Focussing

Here, Mach-Zehnder fringes are shown for a pulse transmitted through the CS_2 cell. The peak laser pulse intensity is at the self-focussing threshold, and at the peak intensity the pulse self-focusses and the contrast ratio of the Mach-Zehnder fringes is destroyed.

TABLE 2.2

Laser glass compositions

Glass	SiO_2*	NaO_2	K_2O	Al_2O_3	BaO	ZnO	CoO	Li_2O	Nd_2O_3	CeO_2	Sb_2O_3
ED-2	65.2			4.7			10.3	16.4	3.1	0.5	
ED-4	65.2			4.7			10.3	16.4		0.5	
L60	70.6	7.6	11.5	1.6	5	1.6		1		1	
C1020	68.5	7.4	11.1	1.5	4.9	1.5		1	3		1
C835	68.5	7.4	11.1	1.5	4.9	1.5		1	5		1
C2828	64.9	16		1		2	12		3	1.1	

*Numbers in table are approximate weight percent

linearly and circularly polarized light and the results can be compared with the predictions of Eq. (2.19). Several other aspects of optical nonlinearities relate to our data and are discussed below.

The ratio of n_2's measured with linearly and circularly polarized light is one of the easiest features of our data to discuss. Eq. (2.19) predicts that this ratio is 3/2 for materials where optical nonlinearities are due solely to electronic interactions. In materials with both electronic and nuclear interactions, the ratio can be used to estimate the relative size of contributions from these two types of interaction.

The n_2 measurement with circularly polarized light is more difficult to perform than the measurement with linearly polarized light because of optical perturbations in the laser beam caused by the quarter wave plates. Since the experiment is easier to execute with low laser power, we performed the measurement on two materials with relatively high optical nonlinearities: Schott SF-6 glass (a high index, lead-doped dense flint glass) and an Nd:YAG laser rod. For both of these materials the n_2 ratio for the two laser polarizations is within experimental error of the theoretically expected value of 1.5. The measured ratio for the Schott glass is almost exactly 1.5, while the value for Nd:YAG is barely within the limits of experimental error.

From these results, it is clear that significant improvements in experimental accuracy will be needed if the n_2 ratios are to be used for estimating the relative contributions to optical nonlinearities from nuclear and electronic processes. There is simply no way to determine whether the value for Nd:YAG is significant or whether it is just indicative of experimental inaccuracy. Unfortunately, there

is little present possibility of improvement on our measurements because of limitations associated with currently available high power pulsed laser system.

Theoretical calculations have also been used to predict additional aspects of the behavior of optical nonlinearities besides the ratio of n_2's for different light polarizations. These theoretical approaches usually relate the nonlinear index coefficient n_2 to the linear index of refraction and the dispersion of a material. The situation is very complicated, but n_2 is often found to depend on the fourth power of the linear index n_0 and to depend on the dispersion of the index in a complicated way. Calculation of specific n_2's can be difficult because the nonlinear dependences and the resulting values are often very sensitive to small changes in the data used for the calculation. For example, a small change in the wavelength range of data used to characterize the index of refraction dispersion for glasses can result in major changes in the final results of the calculations.

The five glasses included in our samples show intersting behavior with respect to the index of refraction. The results of these measurements are in reasonable agreement with the corresponding calculated predictions.[28] Our data shows that the nonlinear index coefficient of Schott SF-6 glass is about $9 \cdot 10^{-11}$ esu, which is much larger than the n_2's of the four laser glasses. This large difference in the n_2's is consistent with the differences in the corresponding indices of refraction: SF-6 has an n_0 of about 1.77, while the laser glasses have an n_0 of about 1.53.

The dispersion of an optical material has an equally important to the optical nonlinearity as the linear index of refraction. The effect of such contributions can be seen by examining the n_2's of the four

laser glasses. All of these glasses have nearly the same linear index ($n_0 \approx$ ..53), with ED-2 having the largest n_0. But there is considerable variation in the n_2 of these glasses, with ED-2 having the smallest n_2 of the group. Since the linear indexes are nearly identical, these glasses form a situation where the additional contributions to n_2 can be conveniently compared.

A more striking example of this complicated behavior can be seen by examining the measured n_2's of ruby and YAG. Ruby and YAG both have large indices of refraction (1.76 and 1.83, respectively) and are both crystalline laser materials. Our results show YAG to have a relatively large nonlinear index coefficient of about $3.5 \cdot 10^{-13}$ esu. This value is also in reasonable agreement with the theoretically expected values. However, the result for ruby shows an n_2 of about $1.5 \cdot 10^{-13}$. This is a very low value, considering the linear index of refraction and our result has not been reproduced by theoretical calculations. This particular case is illustrative of current problems associated with the understanding of optical nonlinearities. The disagreement could be due to hidden experimental errors, but we feel the problem is more likely to rest with methods used for theoretical calculations.

The data for the four laser glasses was intended to serve as an example of nonlinear index values as a function of glass composition. The composition of these and other relevant glasses is indicated in Table 2.2. The Americal Optical glasses (C1020, C835 and C2828) are basically sodium silicate glasses with minor variations in composition, and these glasses were designed to have a low n_2 value. These glasses have a similar composition to Americal Optical LSO laser glass, which

is often used in current neodymium laser systems. The Owens Illinois glass is another commonly used laser glass and has a basic alumio-silicate base glass composition.

One commonly expected characteristic of optical nonlinearities in neodymium laser glasses is that the n_2 value will be relatively independent of the neodymium doping level. This behavior is expected basically because the neodymium nuclei and electrons are present in low concentrations, and are expected to have negligible contributions to the nuclear and electronic interactions responsible for the nonlinearities. Comparison of samples C1020 and C835 (which differ only in the neodymium doping level) gives a strong verification of this expected behavior. The raw data for these two samples are nearly indistinguishable and the data analysis yields identical n_2 values for both glasses.

Comparison of the n_2 of the C1020 sample and the n_2 of the ED-2 sample has produced an unexpected question relative to the dispersive behavior of n_2. Our measurements show the n_2 of ED-2 to be lower than the n_2 of C1020 by about 20%. Owyoung[17] has used ellipse rotation measurements to estimate the n_2's of various materials. In particular, he estimates n_2 values for ED-4 and LSO glass samples. The composition of these glasses is shown in Table 2.2 and they are shown to be very similar to our own ED-2 and C1020 samples. ED-2 and ED-4 glasses differ only in the neodymium doping level and are expected to have identical n_2's. C1020 and LSO glasses have very similar, but not identical compositions, and may have identical optical nonlinearities. However, Owyoung's and Hellwarth's[16] measurements, which were performed with a 0.6943μm ruby laser, find that ED-4 has a roughly 20% higher n_2 than LSO glass. Comparison with our results for the corresponding glasses show that his measurements show an opposite result to our own.

There are two main possible reasons for this difference. Either the composition differences between LSO and C1020 result in major (~40%) differences in the n_2's or the difference is a striking example of dispersion of the nonlinear index. Owyoung's measurement was made with 0.6943 μ light, while ours was made with 1.06 μ. The different wavelengths used could be responsible for the different results of the measurements. If the difference is due to dispersion of n_2, it would be an interesting example of another case where theoretical calculations are inconsistent with the experimental results.

Although lucite is not currently actively used in high power laser systems, its n_2 measurement is interesting for several reasons. In spite of the extra experimental uncertainty, the final relatively low n_2 value of about $1.5 \cdot 10^{-13}$ esu suggests that there may be applications where low n_2 plastic would be desirable in high-peak intensity laser systems. Lucite is the only plastic material included in our samples and is also the only material which has a significant absorption cross section at 1.06 μ. Thus, the measurement indicates that n_2 measurements are feasible for materials which have nonzero absorption cross sections at the wavelength used for the measurement.

V. CONCLUSIONS

We have used time resolved interferometry and a 1 nanosecond pulsed laser system to investigate several aspects of optical nonlinearities. The apparatus has been used to perform detailed observations of important characteristics of laser beam propagation in nonlinear media in the absence of catastrophic nonlinear processes. We have also completed comparative measurements of optical nonlinearities in a variety of dielectrics. These experiments are useful diagnostic studies of nonlinear optical behavior and supply badly needed data for comparison with theoretical predictions of nonlinear beam propagation and magnitudes of optical nonlinearities.

The high quality laser beam together with the streak camera make possible the detailed observation of the time resolved behavior of laser beam propagation through nonlinear media. We have observed three distinct types of nonlinear behavior in the absence of catastrophic nonlinearities. First, we have verified previous experimental observations of "thin lens" nonlinear propagation. While this is a noncatastrophic effect and usually causes only a change in the laser beam diameter, it is an important effect because, at higher laser intensities, it leads to self-focusing and damage in laser systems.

Secondly, we have observed major perturbations in the laser beam spatial intensity profile due to the interference effects of optical nonlinearities. Previous investigations[2,20] have demonstrated that small scale intensity fluctuations of a laser beam can be amplified

by nonlinear processes; with the result that they destroy the desired spatial coherence of the beam. Our results show that there are other processes in which the spatial intensity profile of a beam can undergo drastic changes in the absence of initial small scale intensity fluctuations. This behavior appears to occur as a consequence of the interference of nonlinearly induced perturbations of the laser beam wavefronts. Although this is a noncatastrophic effect, it is important because the resulting intensity fluctuations can lead to self-focusing behavior.

The third distinct type of behavior is characterized by the nearly total destruction of the temporal smoothness and coherence of the laser pulse. A surprising aspect of this effect is that it occurs without causing major changes in the transverse spatial coherence of the beam. This behavior contrasts sharply with the previously nonlinear processes in which changes in the transverse spatial intensity profile occurred without noticeably affecting the temporal coherence of the pulse. Ours is the first observation of this unusual temporal behavior and this is probably due to the unique experimental capabilities.

The fundamental interactions responsible for the anomalous temporal behavior are not known, but self-focusing and Raman scattering have been eliminated as possible candidates. The effect is also characterized by the backward scattering of appreciable ($\sim$10%) amounts of the laser beam. Careful analysis of this back scattered light may reveal the fundamental

scattering mechanisms. It is important that this behavior be investigated and understood because it has immediate relevance to laser systems where temporal coherence of high intensity beams is desired.

Our nonlinear index coefficient measurements have demonstrated a versatile and useful experimental technique. The time resolved interferometric technique can be used for either absolute[11] or relative measurements of n_2. The method is applicable to a wide variety of materials and can be quickly modified to measure different characteristics of n_2, such as its laser polarization dependence. When used for ratio measurements, the technique is relatively quick and avoids the time consuming calibration necessary with most other measurement techniques.

With the variety of the types of materials we examined, the measured n_2 ratios can be used to illustrate the different kinds of information which can be obtained. The measurements on silicate laser glasses demonstrate a study of the dependence of n_2 on material composition. Comparison of the present data with the results of other experiments can be used to look for behavior such as the frequency dependence of n_2.

The data is especially useful for comparison with theoretical predictions of optical nonlinearities. For example, using a simple Stark-effect model including local field effects and only one judiciously chosen ultraviolet absorption (harmonic oscillator) frequency,[13] the magnitudes and ratios of n_2 for the solids in Table 2.1 can be fairly well predicted. A significant departure from this agreeable behavior is our result for the n_2 of ruby, where the measured n_2 is much smaller than is theoretically predicted.

Independent of the contribution to an understanding of the overall optical nonlinearity problem, the n_2 measurements are also useful for their direct technical applications. It is feasible that composition dependence studies of n_2 can be used to aid in the development of laser materials with smaller optical nonlinearities. The data are useful because they provide numbers needed as design criteria for the development of high power solid state lasers. The data are especially useful in this particular respect because the phase delays measured in our experiments are directly related to the onset of self-damage mechanisms in high power lasers.

The advantages of a ratio measurement of n_2's have already been mentioned. Our data can be used to illustrate one of these advantages by comparison with n_2 measurements by other workers.[7,11,16] Table 2.3 lists some of our results with the results of three independent measurements of the absolute value of n_2. For materials where n_2 can be compared, there is seen to be as much as 70% discrepancy in the results. This discrepancy is rather unsatisfactory in comparison to the 15-20% accuracy generally expected in these measurements. Much of the disagreement between results may be due to the difficulty of the calibration of absolute n_2 measurements.

If the n_2 ratios for appropriate materials are computed for the results in Table 2.3, the disagreement between different measurements is generally limited to about 25% and is much more consistent with the expected accuracies. A notable exception to this improvement is comparison of our measurement of the n_2 of C-1020 glass with Owyoung's measurement on LSO glass, but this anomaly has been discussed above. We feel that these results illustrate the usefulness of ratio measurements for comparison of the results of n_2 measurements by different experimenters.

TABLE 2.3

Comparison of measured n_2's

Materiol	Present work	Owyoung[16]	Levenson[7d]	Speck[11]
ED-4 ED-2	1.53*	1.73	2.6	1.52
LSO C-1020	1.83	1.44		
YAG	3.47	4.27	4.46	3.16
Ruby Sapphire	1.48		2.4	

*n_2 expressed in ubits of 10^{-13} esu

Our data illustrate only a few of the kinds of measurements which can be performed with the interferometric technique. The technique could be modified to determine possible resonant contributions to n_2 in optically pumped Nd lasing materials where the lasing transition itself can contribute to n_2. With some improvement in the laser properties, the technique could be used to probe the magnitude of higher order nonlinearities[30] such as the n_4E^4 term. If, for example, the n_4E^4 term were comparable to the minimum detectable fringe distortion in our experiments, the plot of fringe shift versus intensity in Fig. 2.8 would not be linear. The lack of any sizeable evidence for this behavior in our measurements establishes an upper limit for n_4 which in ED-2 glass is $6 \cdot 10^{-21}(esu^4)$.[30]

ACKNOWLEDGMENTS

In today's world of complicated technology, it would be rare for a person to be able to complete a piece of technical work without obtaining valuable assistance from a number of collaborators. This is especially true for this thesis, where many of the rewards have come from learning to cope with technical problems.

During the nonlinear index coefficient measurements I was given intense and energetic support by R. L. Carman. Discussions with W. H. Lowdermilk were also a source of encouragement and assistance. I wish to also acknowledge valuable technical assistance from Jim Kysilka, Oroville Dahlby, Bobbie Smith and Scott Hawley.

During the radiation damage experiments I received continuous and valuable support from my thesis advisor, Mike Schwab. Of particular value were conversations with Mike and with John Vitko. I would also like to acknowledge the intermittent, but extremely helpful, assistance of Aki Kuramoto, who helped to bail me out of a number of foundering situations. To these people, and the many others who helped me at various stages of completion of this work, I express my deepest appreciation.

Appendix 1. The Polarization Vector

The response of a material to an applied electric field $\vec{E}(t)$ can be described in terms of the electric polarization vector $\vec{P}(t)$. In the simplest case, these two vectors are linearly related through the electric susceptibility χ_0:

$$\vec{P}(t) = \chi_0 \vec{E}(t) \tag{A1.1}$$

When the applied electric fields contain a spectrum of different frequency components, the frequency dependence of χ_0 must be accounted for, and equation (A1.1) is redefined in the frequency domain:

$$\vec{P}(\omega) = \chi_0 (\omega)\vec{E}(\omega) \tag{A1.2}$$

In order to specify the time dependence of $\vec{P}$, it is now necessary to transform the components of Eq. (A1.2) into the time domain by use of the Fourier transform. For $\vec{P}(t)$ we obtain:

$$\vec{P}(t) = \frac{1}{\sqrt{2\pi}} \int_{-\infty}^{\infty} \vec{P}(\omega) e^{-i\omega t} d\omega \tag{A1.3}$$

Substituting the right-hand side of Eq. (A1.2) for $\vec{P}(\omega)$ in Eq. (A1.3) we find:

$$\vec{P}(t) = \frac{1}{\sqrt{2\pi}} \int_{-\infty}^{\infty} \chi_0(\omega)\vec{E}(\omega) e^{-i\omega t} d\omega \tag{A1.4}$$

But, since

$$\chi_0(\omega) = \frac{1}{\sqrt{2\pi}} \int_{-\infty}^{\infty} \chi_0(t') e^{i\omega t'} dt' \quad , \tag{A1.5}$$

Eq. (A1.4) becomes

$$\vec{P}(t) = \frac{1}{\sqrt{2\pi}} \int_{-\infty}^{\infty}\int_{-\infty}^{\infty} \chi_0(t')e^{-i\,\omega(t-t')}\vec{E}(\omega)d\omega dt' \qquad (A1.6)$$

$$= \frac{1}{\sqrt{2\pi}} \int_{-\infty}^{\infty} \chi_0(t')\vec{E}(t-t')dt' \quad , \qquad (A1.7)$$

where a Fourier transform has been used to obtain Eq. (A1.7) from Eq. (A1.6).

When expanded in a Taylor series, E(t-t') takes the form:

$$\vec{E}(t-t') = \vec{E}(t) - t'\left(\frac{\partial E(t)}{\partial t}\right) + \frac{t'^2}{2}\left(\frac{\partial^2 E(t)}{\partial t}\right) + \cdots \qquad (A1.8)$$

$$= \left[e^{-\left(t'\left(\frac{\partial}{\partial t}\right)\right)}\right]_{op} \vec{E}(t) \qquad (A1.9)$$

In Eq. (A1.9), the Taylor series expansion is represented in terms of a differential operator.

Now, substituting the result of Eq. (A1.9) into Eq. (A1.7) yields

$$\vec{P}(t) = \left[\frac{1}{\sqrt{2\pi}} \int_{-\infty}^{\infty} \chi_0(t')e^{-\left(t'\left(\frac{\partial}{\partial t}\right)\right)}\partial t'\right]\vec{E}(t) \qquad (A1.10)$$

And the Fourier transform of Eq. (A1.10) becomes:

$$\vec{P}(t) = \left[\chi_0\left(i\frac{\partial}{\partial t}\right)\right]_{op} \vec{E}(t) \quad , \qquad (A1.11)$$

where:

$$\left[\chi_o\left(i\frac{\partial}{\partial t}\right)\right]_{op} = \chi(\omega_o) + i\frac{\partial\chi_o(\omega)}{\partial\omega}\frac{\partial}{\partial t} - \frac{1}{2!}\frac{\partial^2\chi_o(\omega)}{\partial\omega^2}\frac{\partial^2}{\partial t^2} + \ldots \qquad \text{(A1.12)}$$

This result shows that a differential operator can be used to calculate the time dependent $\vec{P}(t)$ from $\vec{E}(t)$. The first term in the expansion (Eq. (A1.12)) of the operator gives the usual linear susceptibility $\chi_o(\omega_o)$. The second term describes the effects of linear chromatic dispersion; and when included in Maxwell's wave equation, gives the correct group velocity

$$v_g = \frac{d\omega}{dk} \qquad \text{(A1.13)}$$

for propagation of light in a dielectric material.

An alternate approach[31] to light propagation will yield the same results as ours, but uses an integral equation description of the system rather than a differential equation description. An advantage of the differential equation approach is that contributions associated with different orders of dispersion can be isolated and evaluated individually.

Appendix 2. Gaussian Propagation

There are many approaches to a description of fundamental aspects of light propagation and diffraction. One convenient problem relevant to laser beam propagation is to solve Maxwell's wave equations for a cylindrical beam with a Gaussian radial intensity profile with initially plane wavefronts.

The wave equation for light propagation in a dielectric medium with dialectric constant ε is:

$$\nabla^2 E(x,y,z,t) = \frac{\varepsilon}{c^2} \frac{\partial^2}{\partial t^2} E(x,y,z,t) \quad . \tag{A2.1}$$

Writing the electric field in terms of its envelope $\vec{E}(x,y,z)$,

$$\vec{E}(x,y,z,t) = \mathrm{Re}\vec{E}(x,y,z)e^{-i\omega t}e^{ikz} \quad , \tag{A2.2}$$

and using the slowly varying envelope approximation

$$\left| \frac{\partial^2 \vec{E}}{\partial z^2} \right| << \left| k \frac{\partial \vec{E}}{\partial z} \right| \quad , \tag{A2.3}$$

The wave equation becomes:

$$\frac{-\omega^2}{c^2}\varepsilon\vec{E} = \nabla_T^2\vec{E} + 2ik\frac{\partial \vec{E}}{\partial z} - k^2\vec{E} \quad , \tag{A2.4}$$

where

$$\nabla_T^2 = \frac{\partial^2}{\partial x^2} + \frac{\partial^2}{\partial y^2} \quad . \tag{A2.5}$$

But since

$$k^2 = \frac{\varepsilon\omega^2}{c^2} \quad , \tag{A2.6}$$

we obtain

$$\nabla_T^2\vec{E} + 2ik\frac{\partial \vec{E}}{\partial z} = 0 \quad . \tag{A2.7}$$

When Eq. (A2.7) is viewed as an operator equation, it has a simple solution which can be written[32]

$$\vec{E}(x,y,z) = e^{\frac{-z}{2ik}\nabla_T^2}\vec{E}(x,y,o) \tag{A2.8}$$

Now, for our Gaussian beam (as in Fig. 2.1),

$$\vec{E}(x,y,o) = A e^{\frac{-r^2}{2a^2}} \tag{A2.9}$$

The two dimensional Fourier transforms of this function gives (k_x,k_y,o):

$$\vec{E}(k_x,k_y,o) = \frac{1}{2\pi}\int_{-\infty}^{\infty}\int_{-\infty}^{\infty} dxdy\, e^{ik_x x} e^{ik_y y} e^{\frac{-z}{2ik}\nabla_T^2}\vec{E}(x,y,o) \tag{A2.10}$$

A similar Fourier transform of (k_x,k_y,o) will yield the final solution:

$$\vec{E}(x,y,z) = \left(\frac{A}{1+\frac{iz}{ka^2}}\right) e^{-\left(\frac{r^2}{2a^2}\right)\left(\frac{1}{1+\frac{iz}{ka^2}}\right)} \tag{A2.11}$$

$$= A(z) e^{-\left(\frac{r^2}{2a^2(z)}\right)} e^{-i\left(\frac{kr^2}{2R(z)}\right)}, \tag{A2.12}$$

where

$$R(z) = -\left(z + \frac{ka^2}{z}\right) \tag{A2.13}$$

is the z-dependent radius of curvature of the beam wavefronts, and

$$A(z) = a^2\left(1 + \frac{z^2}{k^2a^2}\right) \tag{A2.14}$$

is the z-dependent $\frac{1}{e}$ intensity radius of the beam. Fig. 2.1 illustrates the qualitative aspects of this solution.

Although precise description of beam propagation depends on details of the initial intensity distribution, the Gaussian case is a good approximation to the beam in our experiments which is initially the central lobe of an Airy pattern. In our experiments, the effect of nonlinear delays is to alter the shape of the wavefronts. Propagation of the perturbed wavefronts leads to the changes in the beam intensity profile which are observed with the streak camera. The Gaussian case is useful because it provides a simple format which can be used to help understand the different types of behavior we have observed.

Appendix 3. Qualitative Self-Focusing

Self-focusing of laser beams occurs as a result of wavefront distortions induced by nonlinear optical processes. Optical nonlinearities will distort wavefronts in response to the high electric field intensities associated with high power laser pulses. Characteristics of the self-focusing depend on the intensity profile, and spectral and temporal characteristics of the beam.

The laser beam in our experiments is a temporally and spectrally bandwidth limited pulse with a very smooth transverse intensity profile. While the accurate description of the onset of self-focusing is generally a difficult problem requiring sophisticated numerical techniques for its solution, the well defined laser beam considered here allows a simple analysis of the system to be used for understanding its qualitative behavior.

The nonlinear index coefficient n_2 induces optical path length increases which are proportional to the laser light intensity. Since the laser beam has the highest intensity on axis, the greatest nonlinear delays will occur on axis. And nonlinear delays in other portions of the beam will depend on the respective intensities.

Cylindrical beams with initially plane wavefronts will have roughly spherical converging perturbations imposed on the wavefronts. This added spherical character of the wavefronts will affect the beam intensity profile as it propagates and may eventually result in catastrophic self-focusing.

Fig. A3.1 illustrates a scenario useful for a simple description of self-focusing. An initially plane wave beam propagates a distance ℓ through a nonlinear medium. After propagating through the medium, the plane wavefronts have propagated through an on-axis extra path length $\Delta\ell$

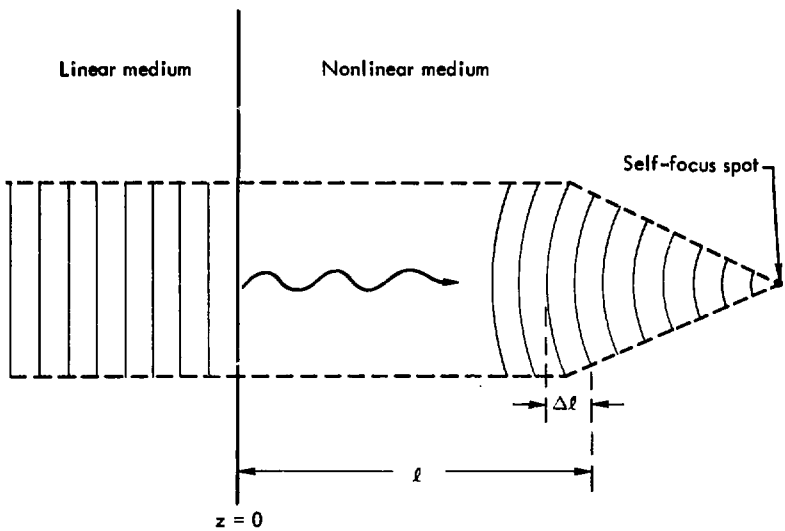

Figure A.3.1 Simplified Description of Self-Focussing

This figure represents a simplified description of self-focussing behavior. A plane wave incident on a nonlinear optical material is shown to experience catastrophic self-focussing as a result of the accumulation of nonlinear delays across the beam wavefronts.

due to the optical nonlinearities. The path length increase $\Delta\ell$ causes wavefront curvature which will lead to focusing of the beam. The focal distance, f, is estimated by using geometrical ray optics to propagate the perturbed wavefronts to their focal point (see Fig. A3.2):

$$\ell_2 n_o = f(n_o + \Delta n) \quad , \tag{A3.1}$$

where: ℓ_2 = distance along beam edge to focal point

n_o = linear refractive index

Δn = nonlinear change in n_o .

But the Pythagorean theorem shows that

$$\ell_2^2 = a^2 + f^2 \quad . \tag{A3.2}$$

Thus, substituting into Eq. (A3.1) we have

$$a^2 = f^2 \left[\left(1 + \frac{\Delta n}{n_o}\right)^2 - 1\right] \tag{A3.3}$$

or:

$$a^2 \approx f^2 \left(\frac{2\Delta n}{n_o}\right)$$

Thus, we finally obtain:

$$f = \frac{a}{\sqrt{2}} \sqrt{\frac{n_o}{\Delta n}} \equiv Z_{sf} \tag{A3.4}$$

This result is only approximate and the results will vary by a factor of 2 depending on the nature and the initial assumptions for the problem.

An alternate form of Eq. (A3.4) can be obtained by noting that

$$\Delta n \, \ell = \Delta\ell \tag{A3.5}$$

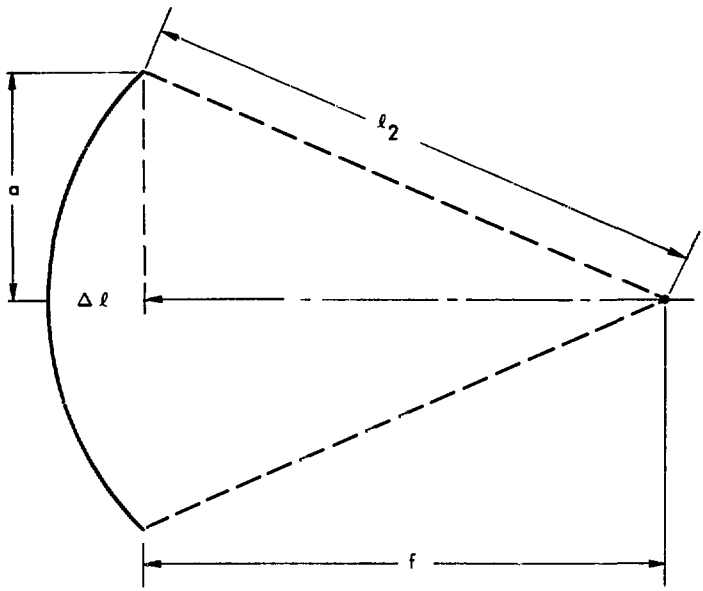

Figure A.3.2 Parameters Used to Estimate Self-Focussing Distances

This figure illustrates the basic geometrical relationships which are for estimations of self-focussing behavior.

But, since $\ell = f$ when the beam self-focuses, we have

$$f = \frac{a}{\sqrt{2}} \sqrt{\frac{n_o f}{\Delta \ell}} \quad , \tag{A3.6}$$

or:

$$f = \frac{a^2}{2} \frac{n_o}{\Delta \ell} = Z_{sf} \tag{A3.7}$$

This form is useful because it emphasizes that for a given magnitude of nonlinear path length increase $\Delta \ell$, the self-focusing distance is proportional to a^2.

If the length ℓ of nonlinear material is much less than the self-focusing distance Z_{sf}, a slight change in the analysis is necessary. When $\ell << Z_{sf}$, negligible changes in the beam intensity profile will occur in the nonlinear medium and the beam will focus at a point beyond the end of the nonlinear medium. For this case (see Fig. A3.2), we now have

$$\frac{\Delta \ell}{a} = \frac{a}{f} \tag{A3.8}$$

or:

$$f = \frac{a^2}{\Delta \ell} = \frac{2 Z_{sf}^2}{n_o \ell} \tag{A3.9}$$

This second case is the situation we work with during our measurements of n_2 ratios. The nonlinear focal lengths in these measurements are long enough so that the streak camera can observe wavefront and intensity profile perturbations in the intermediate field of the beam.

REFERENCES

1. a. For a Theoretical discussion, see, for example, the following P. L. Kelley, "Self-focusing of Optical Beams," *Phys. Rev. Lett.*, Vol. 15, pp. 1005-1008, Nov. 1965.

   b. V. N. Lugovoi and A. M. Prokhorov, "A possible explanation of the small-scale self-focusing filaments," *Pis'ma Zh. Eksp. Teor. Fiz.*, Vol. 7; pp. 153-155, Mar. 1968; also JETP, Lett., Vol. 7; pp. 117-119, Mar. 1968.

   c. For a discussion of an experimental verification, see, for example, the following: C. C. Wang and G. W. Racette, "Effect of linear absorption on self-focusing of laser beam in CS_2," *Appl. Phys. Lett.*, Vol. 8, pp. 256-257, May 1966.

   d. A. V. Butenin, V. V. Korobkin, A. A. Malyutin, and M. Ya. Shchelev, "Investigation of the kinetics of self-focusing in liquids," *Pis'ma Zh. Eksp. Teor. Fiz.*, Vol. 6, pp. 687-690, Sept. 1967; also JETP Lett., Vol. 6, pp. 173-176, Sept. 1967.

   e. M. M. T. Loy and Y. R. Shen, "Study of self-focusing and small-scale filaments of light in nonlinear media," *IEEE I. Quantum Electron.*, Vol. QE-9, pp. 409-422, Mar. 1973.

2. a. R. Y. Chiao, P. L. Kelley, and E. Garmire, "Stimulated four-photon interaction and its influence on stimulated Rayleight-Wing Scattering," *Phys. Rev. Lett.*, Vol. 17, pp. 1158-1161, Nov. 1966.

   b. R. L. Carman, R. Y. Chiao, and P. L. Kelley, "Observation of degenerate stimulated four-photon interaction and four-wave parametric amplification," *Phys. Rev. Lett.*, Vol. 17, pp. 1281-1283, Dec. 1966.

c. A. J. Campillo, S. L. Shapiro, and B. R. Sudyam, "Periodic breakup of optical beams due to self-focusing," *Appl. Phys. Lett.*, Vol. 23, pp. 628-630, Dec. 1973.

d. A. J. Campillo, S. L. Shapiro, and B. R. Sudyam, "Relationship of self-focusing to spatial instability modes," *Appl. Phys. Lett.*, pp. 178-180, Feb. 1974.

3. a. F. Shimizu, "Frequency broadening in liquids by a short light pulse," *Phys. Rev. Lett.*, Vol. 19, pp. 1097-1100, Nov. 1967.

b. R. R. Alfano and S. L. Shapiro, "Observation of self-phase modulation and small-scale filaments in crystals and glasses," *Phys. Rev. Lett.*, Vol. 24, pp. 592-594, Mar. 1970.

4. F. DeMartini, C. H. Townes, T. K. Gustafson, and P. L. Kelley, "Self-steepening of light pulses," *Phys. Rev.*, Vol. 164, pp. 312-323, Dec. 1976.

5. R. A. Fisher and W. K. Bischel, "Pulse compression for more efficient operation of solid state laser amplifier chains," *Appl. Phys. Lett.*, Vol. 24, pp. 468-470, May 1974.

6. J. A. Fleck, Jr., and R. L. Carman, "Laser pulse shaping due to self-phase modulation in amplifying media," *Appl. Phys. Lett.*, Vol. 22, pp. 546-548, May 1973.

7. a. P. D. Maker, R. W. Terhume, and C. M. Savage, "Intensity dependent changes in the refractive index in liquids," *Phys. Rev. Lett.*, Vol. 12, pp. 507-509, May 1964.

b. G. Mayer and F. Gires, "Action d'une onde lumineuse intense sur l'indes de refraction des liquides," *Compt. Rend.*, Vol. 258, pp. 2039-2042, Feb. 1964.

c. M. A. Duguay, J. W. Hansen, and S. L. Shapiro, "Nd:glass laser radiation," *IEEE J. Quantum Electron.*, Vol. QE-6, pp. 725-743, Nov. 1970.

d. M. D. Levenson, "Feasibility of measuring the nonlinear index of refraction by third order frequency mixing," *IEEE J. Quantum Electron.* (Part I of two parts), Vol. QE-10, pp. 110-115, Feb. 1974.

8. C. C. Wang, "Nonlinear susceptibility constants and self-focusing of optical beams in liquids," *Phys. Rev.*, Vol. 152, pp. 149-156, Dec. 1966.

9. A. P. Veduta and B. P. Kirsavov, "Variation of the refractive index of liquids and glasses in a high intensity field of a ruby laser," *Sov. Phys - JETP*, pp. 736-738, Nov. 1968.

10. E. A. McLean, L. Sica, and A. J. Glass, "Interferometric observation of absorption induced index change associated with thermal blooming," *Appl.Phys. Lett.*, Vol. 13, pp. 369-371, Dec. 1968.

11. E. S. Bliss, D. R. Speck, and W. W. Simmons, "Direct interferometric measurements of the nonlinear index coefficient n_2 in laser materials," *Appl. Phys. Lett.*, Vol. 25, pp. 728-730, Dec. 1974.

12. R. W. Hellwarth and N. George, "Nonlinear refractive indices of CS_2-CCl_4 mixtures," *Opto-Electron.*, Vol. 1, pp. 213-217, 1969.

13. N. L. Boling, A. J. Glass, and A. Owyoung, "An empirical relationship for predicting nonlinear refractive index changes in optical solids," unpublished.

14. J. T. Fournier, and E. Snitzer, "The nonlinear refractive index of glass," *IEEE I. Quantum Electron.*,Vol. QE-10, pp. 473-475, May 1974.

15. C. Y. She, M. J. Moran and R. L. Carman, "The degenerate cubic nonlinear susceptibility tensor in an isotropic medium and its determination," unpublished.

16. a. R. W. Hellwarth, A. Owyoung, and N. George, "Origin of the nonlinear refractive index in liquid CCl_4," *Phys. Rev. A*, Vol. 4, pp. 2342-2347, Dec. 1971.

b. A. Owyoung, R. W. Hellwarth, and N. George, "Intensity induced changes in optical polarizations in glasses," *Phys. Rev. B*, Vol. 5, pp. 628-633, Jan. 1972.

17. A. Owyoung, "Ellipse rotation studies in laser host materials," *IEEE J. Quantum Electron.*, Vol. QE-9, pp. 1064-1069, Nov. 1973.

18. W. G. Wagner, H. A. Haus, and J. H. Marburger, "Large scale self-trapping of optical beams in the paraxial ray approximation," *Phys. Rev.*, Vol. 175, pp. 256-266, Nov. 1968.

19. E. L. Dawes and J. H. Marburger, "Computer studies in self-focusing," *Phys. Rev.*, Vol. 179, pp. 862-868, March 1969.

20. E. S. Bliss, D. R. Speck, J. F. Holzrichter, J. H. Erkkila, and A. J. Glass, "Propagation of a high intensity laser pulse with small-scale intensity modulation," *Appl. Phys. Lett.*, Vol. 25, pp. 448-450, Oct. 1974.

21. B. C. Johnson, L. L. Steinmetz, R. L. Carman, and W. H. Lowdermilk, "A laser oscillator that directly produces bandwidth limited pulses in the 1-ns region and an amplifier chain that maintains the single pulse coherence," presented at the Conf. on Laser Engineering and Applications, Washington, D. C., 1973, paper 2.10.

22. L. W. Coleman and S. W. Thomas, "New 10-ps streak camera for laser pulse diagnostics," presented at the Conf. on Laser Engineering and Applications, Washington, D. C., 1973, paper 19.2.

23. E. S. Bliss, private conversation.

24. S. R. Gunn, "Volume absorbing calorimeters for high-power laser pulses," *Rev. Sci. Inst.*, Vol. 45, pp. 936-943, July 1974.

25. Reference to company or product name does not imply approval or recommendation of the product by the University of California or the U. S. Atomic Energy Commission to the exclusion of others that may be suitable.

26. T. A. Wiggins, R. V. Wick, N. D. Foltz, C. W. Cho, and D. M. Rank, "Optical mixing in stimulated Brillouin spectra," *J. Opt. Soc. Am.*, Vol. 57, pp.661-665, May 1967.

27. P. Thomas, A. Jares,and B. P. Stoicheff, "Nonlinear refractive index and "DC Kerr constant of liquid CS_2 at 10.6 μm," *IEEE J. Quantum Electron.*, Vol. QE-10, No. 5, pp. 493-494, May 1974.

28. A. J. Glass, private conversation.

29. R. W. Hellwarth, J. Cherlow, and T. T. Yang, "Origin and frequency dependence of nonlinear optical susceptibilities of glasses," *Phys. Rev. B*, Vol. 11, No. 2, pp. 964-967, Jan. 15, 1975.

30. T. K. Gustafson, P. L. Kelley, R. Y. Chiao and R. G. Brewer, "Self-trapping in media with saturation of the nonlinear index," *Appl. Phys. Lett.*, Vol. 12, pp. 165-168, March 1968.

31. J. D. Jackson, "Classical Electrodynamics," N. Y., Wiley, 1962.

32. J. H. Marburger, private conversation.